NORTHWESTERN UNIVERSITY

Synthesis, Shape, and Surfaces of Strontium and Barium Titanate Nanocrystals

A DISSERTATION

SUBMITTED TO THE GRADUATE SCHOOL
IN PARTIAL FULFILLMENT OF THE REQUIREMENTS

for the degree

DOCTOR OF PHILOSOPHY

Field of Materials Science and Engineering

By

Lawrence Crosby

EVANSTON, ILLINOIS

June 2018

ProQuest Number: 10821732

All rights reserved

INFORMATION TO ALL USERS
The quality of this reproduction is dependent upon the quality of the copy submitted.

In the unlikely event that the author did not send a complete manuscript
and there are missing pages, these will be noted. Also, if material had to be removed,
a note will indicate the deletion.

ProQuest 10821732

Published by ProQuest LLC (2018). Copyright of the Dissertation is held by the Author.

All rights reserved.
This work is protected against unauthorized copying under Title 17, United States Code
Microform Edition © ProQuest LLC.

ProQuest LLC.
789 East Eisenhower Parkway
P.O. Box 1346
Ann Arbor, MI 48106 – 1346

© Copyright by Lawrence Crosby 2018

All Rights Reserved

ABSTRACT

Synthesis, Shape, and Surfaces of Strontium and Barium Titanate Nanocrystals

Lawrence Crosby

The atomic surfaces structures of shape-controlled oxide supports prepared hydrothermally result in nanocrystals for use as model catalysts to bridge the “materials gap” from studies on single crystals. $SrTiO_3$ (001), (110), and $BaTiO_3$ (001) surfaces are investigated using several techniques, and synthetic approaches to obtain these materials are discussed in detail.

The Wulff shape of $SrTiO_3$ was determined to be an octadecahedron with six {100} facets and twelve {110} facets. TEM measurements of the faceting ratios $h_{110} : h_{100}$ were found to agree well with surface energy ratios $\gamma_{110} : \gamma_{100}$ derived from first-principles calculations.

Using aberration-corrected HREM, the surface structure of {110}-faceted $SrTiO_3$ nanoparticles synthesized solvothermally using glycerol as the surfactant yielded (n × 1) reconstructions with n=3 or 4. These structures are titania-rich and contain tetrahedrally coordinated TiO_4 units, similar to prior observations for $SrTiO_3$ (110) single crystal surfaces.

Aberration-corrected HREM investigation of $SrTiO_3$ nanocuboids made using caprylic acid, ethanol, and also $BaTiO_3$ nanocuboids revealed that the (001) surfaces for all these nanoparticles are terminated with a TiO_2 double layer. These results are similar to prior observations of TiO_2-rich surface reconstructions on $SrTiO_3$ nanocuboids made hydrothermally and single crystals prepared via wet chemical etching.

Pt and Pt deposited onto $SrTiO_3$ nanopolyhedra were investigated by HREM to determine the stable Winterbottom construction. The supported Pd particles were found to be predominantly multiply twinned particles while Pt particles were predominantly single crystals.

The effects of sub-nanometer atomic layer deposition of films of titania and alumina are compared for the acrolein hydrogenation selectivity of Pt catalysts supported on $SrTiO_3$. The titania-overcoated catalyst is similar to strong metal-support interaction catalysts formed by high temperature reduction, with a thin titania film on top of the supported Pt nanoparticles and an increase in allyl alcohol selectivity, neither of which are observed for the alumina-overcoated catalyst.

Pt-$SrTiO_3$ (110) catalyst samples prepared by ALD onto $SrTiO_3$ dodecahedra are compared with Pt-TiO_2 catalysts prepared by ALD onto commercially purchased anatase TiO_2. Catalytic testing of the CO oxidation reaction indicate that the turnover frequency for $SrTiO_3$ dodecahedra is significantly higher than anatase TiO_2.

Approved by

Professor Laurence D. Marks
Department of Materials Science and Engineering
Northwestern University, Evanston IL 60208, U.S.A

Acknowledgements

I first want to acknowledge my thesis advisor, Professor Laurie Marks, for putting up with my incessant questioning for the past five and half years. This has been a long journey of discovery, one that I hope to continue long after my days here at Northwestern are through. I have learned not only a good deal of materials science, but also how to go about learning something completely new and different. I look forward to the next challenge, and I feel well-prepared to tackle whatever it may be.

I want to thank Professor Ken Poeppelmeier for allowing me to use his laboratory space for all of the synthesis work in this thesis. The work would not have been possible without this critical component. Thank you to my committee members, Professors James Rondinelli and Michael Bedzyk for taking the time to peruse my dissertation and for providing feedback and support during my oral defense.

I have had much help along the way, and I hope that I can successfully name at least the majority of those who have contributed to me successfully reaching this milestone. Thank you to Dr. Robert Kennedy for the many hours given to bench work in the lab, for comments on paper manuscripts, and many useful discussions. Thank you to Dr. Bor-Rong Chen for many shared hours on synthesis, as well as discussions about papers, literature, and next moves.

Thank you to all of the facility managers who made it possible for me to acquire data, a critical component to make my work possible: Dr. Neil Schweitzer, Dr. Jinsong Wu, Dr. Alan Nichols, and Jerry Carsello. Thanks to Dr. J.G. Wen of Argonne National Lab for assistance with using the ACAT and obtaining quite a few beautiful TEM images. Thanks to collaborators who provided samples for me to test, and expertise in characterization techniques where I am a debutant: Dr. Xin Tang and Ryan Hackler. Thank you to group members who took the time to read through and give suggestions for paper manuscripts as well as the manuscript for this thesis: Christopher Mizzi, Alex Lin, Ryan Paull, Dr. Edmund Long, and Zachary Mansley in particular. Thanks to others who provided support by means of boosting morale and providing encouragement during difficult times: Dr. Pratik Koirala, Dr. Lingxuan Peng, Tiffany Ly, Dr. Stephanie Moffitt, Dr. Joshua Yeh, and others who I am surely forgetting. Finally, thank you to my friends and family who have provided emotional and spiritual support, particularly important to give the final push these last few years: Ginger and Andy, my sister, Ashley, Starlett, Amy and Jeff, Logan and Cristina, Hialy, Julie, Isabel, Liz, Mindy, Rebekah, Crystal, Si, Leah, Keith, Sara, Donna, and many others. Your encouragement, love, and support are greatly appreciated.

List of Abbreviations

ALD: atomic layer deposition.

BCO: $BaCO_3$.

BET: Brunauer–Emmett–Teller.

BTO: $BaTiO_3$.

BVS: bond valence sum.

DFT: density functional theory.

DRIFTS: diffuse reflectance infrared Fourier transform spectroscopy.

EDS: energy dispersive spectroscopy.

EELS: electron energy loss spectroscopy.

FCC: face centered cubic.

FWHM: full width at half maximum.

HAADF: high angle annular dark field.

HREM: high resolution electron microscopy.

ICP: inductively coupled plasma.

ICP-OES: inductively coupled plasma optical emission Spectroscopy.

MTP: multiply twinned particle.

RT13: $(\sqrt{13}\times\sqrt{13})\,R\,33.7^\circ$.

RT5: $(\sqrt{5}\times\sqrt{5})\,R\,26.6^\circ$.

SAXS: small angle X-ray scattering.

SMSI: strong metal support interaction.

$Sr(Ac)_2$: strontium acetate.

STEM: scanning transmission electron microscopy.

STO: $SrTiO_3$.

TED: transmission electron diffraction.

TEM: transmission electron microscopy.

$Ti(OBu)_4$: titanium tetrabutoxide.

$TiCl_4$: titanium tetrachloride.

TOF: turnover frequency.

TON: turnover number.

XPS: X-ray photoelectron spectroscopy.

XRD: X-ray diffraction.

Dedication

This is work is dedicated to my mother and my grandmother, both of whom have left this world all too soon. I hope that I have managed to make both of you proud. I will do my best to carry on your legacy.

Table of Contents

ABSTRACT 3

Acknowledgements 5

List of Abbreviations 7

Dedication 9

List of Tables 17

List of Figures 19

Chapter 1. Introduction 34

- 1.1 Motivation 34
  - 1.1.1 Why study surfaces? 34
  - 1.1.2 Why oxide nanomaterials 35
- 1.2 Organization 36

Chapter 2. Methods 37

- 2.1 Introduction 37
- 2.2 Experimental Techniques 37
  - 2.2.1 Characterization 37
    - 2.2.1.1. Transmission Electron Microscopy 37
  - 2.2.2 Scanning Electron Microscopy 39
  - 2.2.3 X-ray Diffraction 41
  - 2.2.4 X-ray Photoelectron Spectroscopy 42

2.2.5 Infrared Spectroscopy 42

2.2.6 Physisorption 43

2.3 Materials Synthesis 43

2.3.1 Solvothermal Synthesis of Oxide Nanomaterials 43

2.3.2 Sample Preparation 44

2.4 Modeling 45

2.4.1 Review of Basic Thermodynamic Functions and Materials Properties 45

2.4.2 Image Simulation 47

2.4.2.1. Quantitative comparison of image contrast 50

Chapter 3. Wulff Shape of Strontium Titanate 52

3.1 Introduction 52

3.2 Experimental Evidence of Wulff Shape 55

3.2.1 Experimental Methods 56

3.2.2 Image Analysis 57

3.2.3 *Ab-initio* Modeling 60

3.3 Experimental Results 61

3.4 Discussion 64

3.5 Conclusions 67

Chapter 4. Synthesis and Characterization of {110}-Faceted Strontium Titanate Dodecahedra 68

4.1 Introduction 68

4.2 Synthesis 68

4.3 Characterization 69

  4.3.1 X-ray Analysis 69

  4.3.2 XPS Analysis 72

  4.3.3 Electron Microscopy 72

  4.3.4 EDS Analysis 73

  4.3.5 HREM Quantitative Analysis 74

4.4 Results 78

  4.4.1 HREM Imaging and Simulations 79

4.5 Discussion 83

4.6 Conclusions 85

Chapter 5. Synthesis and Characterization of Strontium Titanate Nanocuboids 86

5.1 Introduction 86

  5.1.1 Motivation 86

  5.1.2 Background: Surfactants 86

  5.1.3 Carboxylates 89

5.2 Methods 91

  5.2.1 Goals and approach 91

  5.2.2 Experimental 92

    5.2.2.1. Varied Carboxylate Synthesis 92

    5.2.2.2. Targeted Caprylic Acid Synthesis 93

  5.2.3 Oleic Acid Synthesis 94

5.3 Results 95

  5.3.1 Varied Carboxylic Acids 95

5.3.2 Caprylic Acid Phase Diagram 97
5.3.3 Oleic acid synthesis 99
5.4 Discussion 100
5.5 Conclusion 103

Chapter 6. Synthesis and Characterization of Barium Titanate Nanocuboids 105
6.1 Introduction 105
6.2 Synthesis 106
6.3 Characterization 107
6.4 Results 107
6.4.1 X-ray Measurements 108
6.4.2 X-ray Photoelectron Spectroscopy 109
6.4.3 Electron Microscopy 116
6.5 Discussion 117
6.6 Conclusion 119

Chapter 7. All Roads Lead to TiO_2: {001} Surfaces of Barium Titanate and Strontium Titanate Nanocrystals 120
7.1 Introduction 120
7.2 Methods 121
7.2.1 Synthesis 121
7.2.2 Image Simulations 123
7.3 Results 124
7.3.1 Experimental Results 124

7.3.2 HREM Simulation Results 127

7.4 Discussion 131

7.4.1 Surface Structure 131

7.4.2 Role of Surfactants and Water 132

7.4.3 Comparison with first-principles predicted structures 134

7.4.4 Thermodynamic analysis 134

7.5 Conclusion 138

Chapter 8. Adhesion of Pt and Pd Nanoparticles on Oxide Supports 139

8.1 Introduction 139

8.1.1 Winterbottom Modeling 139

8.1.2 Multiply Twinned Particles and a modified Winterbottom construction 140

8.1.3 Relation to droplet wetting model 145

8.2 Experimental 146

8.2.1 Deposition of Pt and Pd on STO 146

8.2.2 HREM Imaging of Metal–Oxide interface 147

8.2.3 Measurement of contact angle 147

8.3 Results 149

8.3.1 Populations of single crystals and twinned particles for platinum and palladium 150

8.4 Discussion 155

8.4.1 Effect of atomic layer deposition (ALD) precursor 155

8.4.2 Support effect 156

8.5 Conclusions and Future Work 157

Chapter 9. Catalysis on oxide supports 158
  9.1 Introduction 158
    9.1.1 CO Oxidation 159
    9.1.2 Strong Metal Support Interaction via ALD 159
  9.2 Experimental Methods 160
    9.2.1 Preparation of catalyst samples 160
    9.2.2 Characterization 160
    9.2.3 Catalytic testing 161
      9.2.3.1. CO Oxidation 161
      9.2.3.2. Acrolein Hydrogenation 163
  9.3 Results 163
    9.3.1 Selectivity through ALD SMSI 164
    9.3.2 Comparison of STO dodecahedra to anatase titania supports 168
  9.4 Conclusions 169

Chapter 10. Ongoing Projects and Future Work 171
  10.1 Determination of support effect in twinning of Pt and Pd 171
  10.2 Characterization of Catalysis Samples 172
    10.2.1 Initial XPS Results 172
    10.2.2 DRIFT Results 176
  10.3 Proposed Future Work 177
  10.4 Conclusions 178

Appendix A. Appendix A 179

A.1 Thermochemical Data used for Dissolution Enthalpy Calculations in Chapter 7 179
A.2 Structure Files used for Simulations 179

Appendix. Bibliography 195

List of Tables

2.1 Computation speedup gained from the use of Fast Fourier Transform compared to Discrete Fourier Transform. Note that the speed scales logarithmically with size. 49

4.1 NCCF for experimental (left) and simulated (right) bulk motifs imaged along the [001] zone axis. The imaging parameters for simulated images for this zone were C_s=-0.005mm, C_5=0mm, α=0.5 mrad, and Δdf=30 Å. 74

4.2 NCCF for experimental (left) and simulated (right) bulk motifs imaged along the [110] zone axis. The imaging parameters for simulated images for this zone were C_s=-0.015mm, C_5=0mm, α=0.5 mrad, and Δdf=30 Å. 75

6.1 Estimated atomic percentages of key binding energies for $BaTiO_3$ (BTO) and BCO. The C 1s peak at 289 eV was fitted based upon reference values for carbonate phases (see p 41 reference [103] as well as reference [104]). Note that C contamination from the atmosphere and hydrocarbons is unavoidable and likely also present. 110

6.2 Comparison of experimental peak positions and kinematical positions for ring TED pattern of BCO nanowires, showing excellent agreement between the model and experiment. 118

7.1 Table for synthesis parameters for solvothermal synthesis of BTO and STO, as discussed in this chapter. Note that only one case (with oleic acid as the surfactant) results in A-site rich surface terminations. 122

7.2 Dissolution enthapies for TiO_2 and SrO dissolution reactions 7.1–7.6. 138

9.1 Calculated gravimetric TOF, in units of s^{-1} normalized by total platinum platinum mass for platinum deposited on STO dodecahedra and anatase titania supports. Note that the Pt-STO samples had between 10 to 85 times higher turnover rates than the Pt-TiO_2 samples. 169

A.1 Referenced standard enthalpies of formation for species involved in STO surface chemistry. Note that these values are used in thermodynamic analysis in Chapter 7 Section 7.4.4 (see Table 7.2 for calculated dissolution enthalpies). 179

List of Figures

2.1 Schematic (left) showing the electon gun, lenses, and specimen chamber in a modern TEM. Diagram (right) showing various electron-specimen interactions and signals that can be acquired in an electron microscope. TEM schematic adapted from JEOL USA.[29] 38

2.2 Illustration of scale of autoclave used to grow large single crystal of quartz, of several meters in length. Figure adapted from reference [35]. 44

2.3 Schematic illustrating the scattering process that is calculated in multislice simulations. Figure adapted from reference [42]. 48

2.4 Schematic illustrating phase shift due to use of plane waves instead of spherical waves. This also demonstrates that choosing a slice thickness significantly smaller than the lattice parameter has little gain in accuracy 50

3.1 Geometrical illustration of the Wulff construction (also known as a gamma plot) in two dimensions. Image credit reference [51]. 54

3.2 Illustration of the Wulff center measurement for the {100} and {110} facets. 55

3.3 Observed octadecahedral Wulff shape for STO nanoparticles. Projections of the STO Wulff shape along the [111] zone axis (left) and [001] zone axis (right). The shapes were calculated using the WulffMaker Mathematica code[52] with {100} facets shown in green and {110} facets depicted in blue for a h_{110}:h_{100} ratio of 1.14. 56

3.4 Sintering observed after annealing particles for 5 hours at 800°C under flowing O_2. 57

3.5 Example of typical, unannealed $SrTiO_3$ (STO) nanocuboid from hydrothermal synthesis using acetic acid. Note that there is predominantly {100} faceting with rounded corners. The radius of curvature was measured for several such particles: four corners were measured and the mean was calculated for each (see Figure 3.7 for plot summarizing these measurements). 58

3.6 Surface energy ratios for various annealing temperature and times of STO nanocuboids. 59

3.7 Measured radii of curvature for unnannealed STO nanocuboids. 62

3.8 Nanoparticles imaged near the [111] zone axis, with diffraction patten demonstrating that it is a single crystal. Note the hexagonal shape of the nanocuboids projected along this direction, evidence that little, if any, {111} facets are present in the particles. 62

3.9 Post-annealed STO nanocuboids imaged along [001] zone axis. Note the sharp faceting in a), while b) has some residual corner rounding. 63

3.10 Mean void size versus anneal condition. The void size remained constant, on average, in spite of annealing. 64

3.11 Surface energy ratios for various terminations of {100} and {110} facets of STO. 66

4.1 XRD $\theta - 2\theta$ scan for the dodecahedra indexed with cubic STO peak positions. 70

4.2 XRD rocking scan of a) (110) peak of STO dodecahedra and b) (111) peak of the 325 mesh Si powder. By applying the modified Scherrer equation (Equation 4.1), the mean crystallite size in the (hkl) can be determined from the broadening of the (hkl) diffraction peak. 71

4.3 a) XPS Survey Spectrum as well as b) Sr $3p_{1/2}$ and C 1s peaks c) Sr 3d and d) Ti 2p peak positions. 72

4.4 Plot of EDS linescan across nanoparticle with inset of a bright field image showing the location of linescan. 73

4.5 Geometry of (110) facet in plan view when viewed along a) [001] and b) [110] zone axes. The electron beam direction is parallel to the facet. Top-down projections of the rhombic dodecahedron along several low-index zone axes appear below. The [100] (c) and [110] (d) projections show different thickness gradients from the edge of the particle to the center. The top shows the [111] projection (e) with constant thickness at the edge of the polyhedron. 77

4.6 Low magnification SEM a) and HAADF b) images demonstrating dodecahedral shape of the nanoparticles. The three-dimensional character is evident in a), and shows in b) via the intensity changes. 78

4.7 High-resolution a) CTEM and b) HAADF images from two different nanoparticles showing atomically sharp faceting. 79

4.8 Defocus/Thickness map for sample viewed along the [001] zone axis , shown in a) and [110] zone axis, shown in b). Note that for a) there another particle directly behind the thin region which causes a rapid, stepwise increase in thickness. 80

4.9 Atomic model overlaid with simulation with optimal parameters (defocus-50 Å, thickness 58 Å) for a) (3 × 1) and b) (4 × 1) c) O and d) SrTiO along [001] zone axis 80

4.10 a) Experimental profile image down the [001] zone, with an image simulation (red box) for a (3 × 1) reconstruction inset. In b) image simulations for the (3 × 1) and c) (4 × 1) reconstructions are shown with the atomic structure superimposed. The (3 × 1) gave the best fit to experiment for this area, although in other regions it was the (4 × 1). 81

4.11 a) Experimental profile image down the [$1\bar{1}0$] zone, with an image simulation (red box) for a (4 × 1) reconstruction inset. In b) image simulations for the (3 × 1) and c) (4 × 1) reconstructions are shown with the atomic structure superimposed. The (3 × 1) gave the best fit to experiment for this area, although in other regions it was the (4 × 1). 81

4.12 Atomic model overlaid with simulation with optimal parameters (defocus-60 Å, thickness 6 Å) for a) (3 × 1) and b) (4 × 1) c) O and d) SrTiO along [$1\bar{1}0$] zone axis 82

5.1 Illustration of different physical configurations of microemulsion of a surfactant and water as function of concentration. Figure adapted from reference [74], pg 7. 87

5.2 Temperature stability phase diagram of $C_{12}E_6$ as function of surfactant concentration, adapted from reference [75]. S corresponds to an isotropic solution, 2L the co-existence of two isotropic liquids, M middle (hexagonal) phase, N neat (lamellar) phase, C crystalline hydrates, and I ice. 89

5.3 Illustration of the effect of hydrocarbon chain length upon packing distance for polar amphiphiles. Figure adapted from reference [76]. 91

5.4 Phase diagram of the sodium caprylate/butanol/water ternary system. Note that points 1–6 marked on the diagram correspond to synthesis conditions attempted for the purpose of this study. Figure adapted from reference [81]. 94

5.5 Bright-field TEM images of STO nanocuboids resulting from the use of butanoic and pentanoic acid in place of acetic acid. 95

5.6 Bright-field TEM images of STO nanocuboids resulting from the use of hexanoic and heptanoic acid in place of acetic acid. 96

5.7 Secondary electron image showing disparate particle morphology obtained using caprylic acid in place of acetic acid when following the method developed by Federico *et al.* from reference [80]. Note that there are particles with terraces as well as smooth surfaces. 97

5.8 Results of synthesis using caprylic acid, butanol, and water with molar fractions of 0.007, 0.435, and 0.558, respectively. These correspond to point 5 in Figure 5.4. 98

5.9 Results of synthesis using caprylic acid, butanol, and water with molar fractions of 0.07, 0.07, and 0.86, respectively. These correspond to point 2 in Figure 5.4. 98

5.10 Results of synthesis using caprylic acid, butanol, and water with molar fractions of 0.01, 0.13, and 0.86, respectively. These correspond to point 3 in Figure 5.4. 99

5.11 Results of synthesis using caprylic acid, butanol, and water with molar fractions of 0.21, 0.11, and 0.68, respectively. These correspond to point 1 in Figure 5.4. 99

5.12 TEM (left) and HREM (right) images of STO particles resulting from oleic acid synthesis. Note that particles are on average less than 20 nm in size and lack of regular faceting. These results are similar to those in Figure 5.9. Variation in contrast is because of unequal gain calibration for the four quadrants of the CCD detector. 100

5.13 Phase diagram for the oleic acid/butanol/sodium hydroxide system, as shown in Figure 5.15. Point 1 corresponds to the synthesis conditions reported in reference [79]. Point 2 corresponds to the synthesis conditions listed in section 5.3.3. Note that the targeted region is the lamellar liquid crystal, which is highlighted in blue. Also note that substituting ethanol for butanol will alter the phase diagram. 102

5.14 Stability equilibria for water/sodium caprylate/alcohol systems at 20 °C and atmospheric pressure. Note the reduction in area of the Region D, the lamellar phase, for ethanol compared with butanol. Figure adapted from reference [81]. 102

5.15 Stability equilibria for oleic acid/butanol/NaOH system at standard conditions. Note the shift of the stability region for the lamellar liquid crystal phase, labelled as liquid crystalline in the phase diagrams, upon changing the mineralizer from NaOH to $NaCO_3$. Figure adapted from reference [85]. 103

6.1 Powder XRD of products of BTO for run at 240 °C for 24 h. Note the presence of weak reflections resulting from the presence of a secondary phase identified as BCO. 109

6.2 XPS spectra of products of hydrothermal reaction at 240 °C for 24 h. 112

6.3 XPS spectra of products of hydrothermal reaction at 180 °C for 12 h. 113

6.4 XPS spectra of products of hydrothermal reaction at 180 °C for 24 h. 114

6.5 XPS spectra of products of hydrothermal reaction at 180 °C for 48 h. 115

6.6 Bright field TEM image showing polydispersity of BTO nanoparticles resulting from direct substitution of $Ba(OH)_2 \cdot 8\,H_2O$. The effect of lowering reaction temperature on the nanoparticle morphology can be see by comparing (a) to (b). 116

6.7 Size distribution of BTO nanoparticles produced using modified Federico synthesis. 117

6.8 (a) Bright field TEM image of nanorods found during sample imaging. (b) Selected-area TED from nanowires, indexed with peak positions of the witherite structure of BCO. 118

7.1 Polyhedral model of a 2 × 2 supercell of the RT13 reconstruction as reported in reference [60] viewed top-down and side-on. Note that the purple surface units correspond to TiO_5 truncated octahedra. 121

7.2 Low resolution TEM images of a) BTO b) STO-G and c) STO-CA 123

7.3 a) Experimental image of STO-G (001) surface imaged along the [100] zone axis, with simulated image insets of anatase titania [001] (Region 1) and the RT13 reconstruction (Region 2). b) Atomic structure of anatase TiO_2 unit cell along the [001] zone axis. c) Second experimental image of STO-G (001) surface along the [100] zone, with simulation of STO RT13 inset. d) Atomic structure of the STO RT13 reconstruction viewed along the [100] zone axis. e) Key for colors corresponding to O, Ti, Sr, and Ba used in atomic models. Note that the simulations correspond to a single bulk unit cell (orange box) along the projected direction. The conditions for all simulations were: thickness=39 Å, focus=40 Å, and crystal tilt=0. 125

7.4 a) Experimental image of BTO particle (001) surface imaged along the [100] zone axis and with simulated images of the BTO RT13 reconstruction inset. b) Atomic structure of BTO RT13 along the [100] zone axis. c) Experimental image of BTO particle (001) surface along the [110] zone axis, with simulated image contrast of the BTO RT13 reconstruction inset. d) Atomic structure of the BTO RT13 along the [110] zone axis. The simulations correspond to a single bulk unit cell (orange box) along the projected direction. The conditions for all simulation were: thickness=84 Å, focus=50 Å, and crystal tilt 7 mrad with an azimuthal angle of -45°. Note contrast matching a TiO_2 double layer at the surface terraces (the surface and subsurface layers are highlighted with dashed purple rectangles). 126

7.5 a) Experimental image of STO-CA particle (001) surface imaged along the [110] zone axis, with simulated image inset of the STO RT13 reconstruction. b) Atomic structure of the STO RT13. Note that the simulation corresponds to a single bulk unit cell (orange box) along the projected direction. The simulation conditions were: thickness=84 Å, focus=40 Å, and crystal tilt 7 mrad with an azimuthal angle of 45°. Note contrast matching a TiO_2 double layer at the surface (the surface and subsurface layers are highlighted with dashed purple rectangles). 127

7.6 Wide area HREM images of a) STO-CA viewed along the [110] zone axis and b) STO-G viewed along the [100] zone axis. 127

7.7 Montage of BTO and STO simulated motifs along the [100] and [110] zone axes. Thickness increases from left to right, and focus increases from top to bottom. 128

7.8 Comparison between experiment and simulations for the BTO RT13, TiO_2 1×1, and BaO 1×1 surface structures along the [110] zone axis. The conditions were: thickness of 84 Å, focus of 50 Å, crystal tilt 7 mrad with an azimuthal angle of -45°. From the surface and subsurface layers (purple box), the TiO_2 double layer structure best matched the experimental results. 129

7.9 Comparison between experiment and simulations for the BTO RT13, TiO_2 1 × 1, and BaO 1 × 1 surface structures along the [100] zone axis. The conditions were: thickness of 20 Å, focus of 90 Å, crystal tilt 0. Note that the contrast for both TiO_2 1 × 1 and BaO 1 × 1 appears the same along this zone axis. 129

7.10 Comparison between experiment and simulations for the STO RT13, TiO_2 1 × 1, SrO 1 × 1, and c(6 × 2) surface structures along the [110] zone axis. The conditions were: thickness of 84 Å, focus of 40 Å, crystal tilt 7 mrad with an azimuthal angle of 45°. From the surface and subsurface layers (purple box), the TiO_2 double layer best matched the experimental results. 130

7.11 Comparison between experiment and simulations for the STO RT13, TiO_2 1 × 1, SrO 1 × 1, and c(6 × 2) surface structures along the [100] zone axis. The conditions were: thickness of 39 Å, focus of 40 Å, crystal tilt 0. Note that the contrast for both TiO_2 1 × 1 and SrO 1 × 1 appears the same along this zone axis. 130

7.12 Simulated images for the RT5 and (3 × 3) surface structures along the [110] and [100] zone axes. The conditions were the same as the STO simulations in Figure 7.10 and Figure 7.11 along their respective directions. 131

7.13 Molecular structure of various surfactants used in hydrothermal synthesis of titanates. All except oleic acid are used in this study. 132

7.14 Surface enthalpies versus excess TiO_2 at the surface, calculated from DFT known reconstructions on strontium titanate {001} surfaces. The energies are referenced to bulk STO and rutile TiO_2. Reproduced with permission from reference [122]. 135

7.15 Effect of dissolution and hydrolysis of STO surface SrO and TiO_2 on the convex hull. The red points and shaded region correspond to the vacuum DFT surface enthalpies within DFT error of the convex hull, and blue points and shaded region correspond to the net surface enthalpies taking dissolution of SrO and/or TiO_2 into consideration. 137

8.1 Schematic showing three distinct cases of wetting of a crystalline material on a substrate. Left shows complete dewetting, where $\gamma_{\text{int}} - \gamma_{\text{sv}} = \gamma_{\text{pv}}$. The middle illustrates the case where $\gamma_{\text{int}} = 0$. Right shows near complete wetting, where γ_{int} is negative but greater than the absolutive value of the particle surface energy. Not shown is the case where where $\gamma_{\text{int}} \leq -\gamma_{\text{p}}$, which would be complete wetting. Graphic generated using the WulffMaker Winterbottom Mathematica code.[52] 140

8.2 Illustration of decahedral MTP composed of five tetrahedra wetting a substrate. Note that joining tetrahedra together in this manner will not fill space, leaving a gap. This gap is closed by straining the tetrahedra, introducing a defect known as a disclination. See reference [147] for more details. 141

8.3 Two-dimensional illustration of a decahedron wetting a substrate surface. The segments are labeled from 1 through 5 counterclockwise. On the left is a case with three segments in contact with the substrate, with lengths

l_1, l_2, and l_5. On the right is a case with four segments in contact with the substrate, with lengths l_2, l_3, l_4, and l_5. 142

8.4 Illustration of wetting of a droplet on a substrate according to the Young-Dupré model. Figure adapted from reference [144]. 145

8.5 Geometrical illustration of contact angle and particle wetting. The left case shows particle wetting, where $h_{\text{exp}} < r$. The right shows the dewetting case, where $h_{\text{exp}} \geq r$. 148

8.6 Population statistics for images of platinum and palladium nanoparticles observed by HREM. N is the total number of particles observed for each material. More that 100 particles were counted for each material, and 80% of the platinum particles were single crystals, while about the percentage were twinned particles for palladium. 150

8.7 Summary of types of palladium particles observed after deposition on both (001) and (110)-faceted STO nanoparticles. The labels Dh and Ih refer to decahedron and icosahedron, respectively. The scale bar of 1 nm applies to all images. 151

8.8 Histogram showing the distribution in contact angles measured for palladium nanoparticles after deposition on STO supports. Note that this includes both single crystals and twinned particles. 152

8.9 HREM image of palladium nanoparticles on STO (110) surface. Note several decahedra as well as other twinned particles observed. 152

8.10 HREM image of palladium nanoparticles on STO (001) surface. Note several decahedra as well as other twinned particles observed. 153

8.11 HREM image of platinum nanoparticles on STO (110) surface. Note that the majority of the particles are single crystals. 153

8.12 Histogram showing the distribution in contact angles measured for platinum nanoparticles after deposition on STO supports. Note that there is a support-dependence effect, splitting the dataset into two shows that the there is maximum around 75° for the (001) STO, and at 100° for (110) STO. 154

8.13 Histogram showing the distribution in contact angles measured for palladium nanoparticles separated by deposition technique. Note that while the number of counts for the wet impregnation (label WI), is low, 100% of the particles observed were either MTPs or lamellar twinned particles. 156

9.1 Secondary electron images and particle size distributions for (left) 1 platinum ALD and (right) 3 ALD cycles. 164

9.2 Plot of catalytic conversion versus time on stream showing increased selectivity towards allyl alcohol for titania overcoated Pt-STO samples, compared with the bare Pt-STO and alumina-Pt-STO samples. 165

9.3 high resolution electron microscopy (HREM) images of ALD overcoats of (a) alumina and (b) titania. The overcoats are visible as a disordered film at the perimeter of the platinum nanoparticle in (a) and also over the top of the platinum nanoparticle in (b). Note that the scale bar applies to both images. 166

9.4 Combined BF/HAADF/EDS of Al_2O_3/Pt/$SrTiO_3$ (a-c) and TiO_2/Pt/$SrTiO_3$ (d-f). The bright-field (a, d) and HAADF (b, e) images show platinum on the (001) of STO. An amorphous oxide film can be seen at the sides of the platinum nanoparticles in (a) and also on top in (d). The EDS line scan path is shown in purple. EDS of alumina overcoated sample (c) indicates that the alumina overcoat is concentrated at the platinum–STO interface (see also white trace in (b)). The titania overcoat (f) could not be distinguished by EDS from titania signal contributed by the support. 167

9.5 Conversion versus residence time for platinum deposited on titania and STO dodecahedra. The top row shows the samples with 1 Pt ALD cycle, while the bottom row shows 3 Pt ALD cycles deposited onto the supports as labeled. 168

10.1 HREM image of 3 wt% platinum deposited on anatase titania. Note the low contrast which is because of the very small platinum particle size. 172

10.2 XPS scans of the Pt 4d states for the 1 ALD cycle on both STO dodecahedra (left) and anatase titania (right). Note the increase in peak area at higher binding energies for the STO case. 173

10.3 XPS scans of the Pt 4f states for the 1 ALD cycle on both STO dodecahedra (left) and anatase titania (right). Note the peak splitting present in titania sample and absent in the STO sample. 174

10.4 XPS scans of the Pt 4d states for the 3 ALD cycle on both STO dodecahedra (left) and anatase titania (right). Note the increase in peak area at higher binding energies for the STO case. 174

10.5 XPS scans of the Pt 4f states for the 3 ALD cycle on both STO dodecahedra (left) and anatase titania (right). 175

10.6 DRIFTS data for Pt 3c on STO dodecahedra after exposure of sample to CO. The large change in intensity at 2091/cm occured after introducing oxygen into the chamber. Comparable results were obtained for the 1c sample. 176

10.7 DRIFTS data for Pt 3c on anatase titania. Note that the peaks identified at 2397/cm, 2174/cm, 2082/cm, and 2056/cm correspond to CO_2, gas phase CO and linear CO. The intensity for the peaks in this case becomes dominated by background signal after introduction of oxygen into the chamber. 177

CHAPTER 1

Introduction

1.1 Motivation

1.1.1 Why study surfaces?

Surfaces are a defining feature of physical systems. Surfaces are important because they are the epicenter of many phenomena that effect human life, from length scales ranging from the cosmological to the infinitesimal. It goes without saying that the surfaces (and interfaces) are where the action happens.

At the atomic scale, the structure of surfaces can vary significantly from the bulk crystal structure for many materials. Surfaces are distinct from the bulk because of the loss of coordination going from an "infinite" periodic structure to an abrupt termination of said periodicity.[1] For our purposes, we define bulk as the macroscopic crystal structure, meaning the crystal structure on the order of Avogadro's number of atoms in thermodynamic equilibrium.

Simply truncating a bulk crystal along a crystallographic plane will yield an unstable structure which seeks to minimize its energy by one of several structural changes. This includes surface relaxation, contraction, and ordered rearrangements of atoms—known as surface reconstructions. Some of the most famous cases of surface reconstructions are for the semiconductor silicon[2] as well as the metals silver and gold.[3,4] Classical bonding analyses such as the bond valence sum (BVS) approach (see[5] for a detailed discussion) work well to describe surface reconstructions in oxide materials.

In a world that is increasing moving towards miniaturization, surfaces and interfaces are becoming increasingly important to account for. The functionality of physical systems such as thin films and tribological coatings depends strongly upon the interactions between deposited materials and the substrate material. Work on surfaces of single crystals, a well-established field, can serve as a solid starting point from which to study nanocrystals with well-controlled faceting.

1.1.2 Why oxide nanomaterials

Further study and understanding of oxide nanomaterials will inform multiple applications including catalysis,[6–10] electronic devices,[11,12] and energy,[13–16] energy dielectrics,[17] ferroelectrics,[18] substrates for growth of thin films,[19–24] and transparent conductors.[25] At the nanoscale, materials properties can, and often do, deviate from those of their bulk counterparts. Given that chemical reactions occur most readily at discontinuities in materials—namely corners, edges, and surfaces—and that the surface-to-volume ratio increases as particle size decreases, surfaces and interfaces will continue to become more important as nanotechnology advances. Oxide supports are known to play a crucial role in catalytic systems through a variety of physical phenomena, among them, the strong metal support interaction (SMSI) effect.[26]

While quantum confinement effects are not as common in oxides as metals (plasmonic effects) and semiconductors (quantum dots), electronic properties can change drastically. One notable case is that of the $SrTiO_3/LaAlO_3$ interface[27] in which a highly conductive two-dimensional electron gas forms. It is possible that there are more of such unexpected effects that have not, to date, been discovered. As with all forms of basic science, advances in our understanding of the fundamentals will inform future applications, some of which have yet to be envisioned.

1.2 Organization

This dissertation will first describe the experimental and computation methods employed in the work described herein. The following chapters will describe the synthesis and characterization of STO and BTO nanocuboids, experimental evidence for the Wulff shape of STO, the synthesis of STO dodecahedra and resolution of the surface structure of the {110} facets therein, the universal observation of titania-rich surfaces of these materials made via hydrothermal synthesis, and finally catalytic application using the STO nanocuboids and dodecahedra. Ongoing work and future directions which build upon this work will be proposed in the final chapter.

CHAPTER 2

Methods

2.1 Introduction

This chapter describes the experimental methods used throughout the work described in this thesis. A variety of characterization techniques have been employed to determine the chemistry and structure of several different materials. Additionally, the experimental work was supported by computational techniques to corroborate the findings with theoretical predictions. A description of each and the strengths and limitations follows.

2.2 Experimental Techniques

2.2.1 Characterization

2.2.1.1 Transmission Electron Microscopy

The primary analytical tool used in this work is the electron microscope. The first electron microscope was invented by Ruska in 1931.[28] When operated in transmission mode, electron microscopes are capable of resolving atomic positions in a specimen. A schematic of a typical modern transmission electron microscopy (TEM) appears in Figure 2.1. The basic elements are the electron gun, the electron optics system, the sample holder, and the detection system. In a conventional TEM the sample is illuminated with a nearly parallel electron beam that is accelerated to high voltage. The wavelength of the electrons which reach the sample will be given by the de Broglie relation $p = \hbar\lambda$, and with a relativistic correction applied will be on the order of 2.51×10^{-12} m. The resolution limit, as defined by the Rayleigh criterion of $1.22\lambda/\beta$, will be on the order of one-half the wavelength of the illumination source, or in our case 1.2×10^{-12} m. This is several times smaller than the radius of an atomic in its ground state!

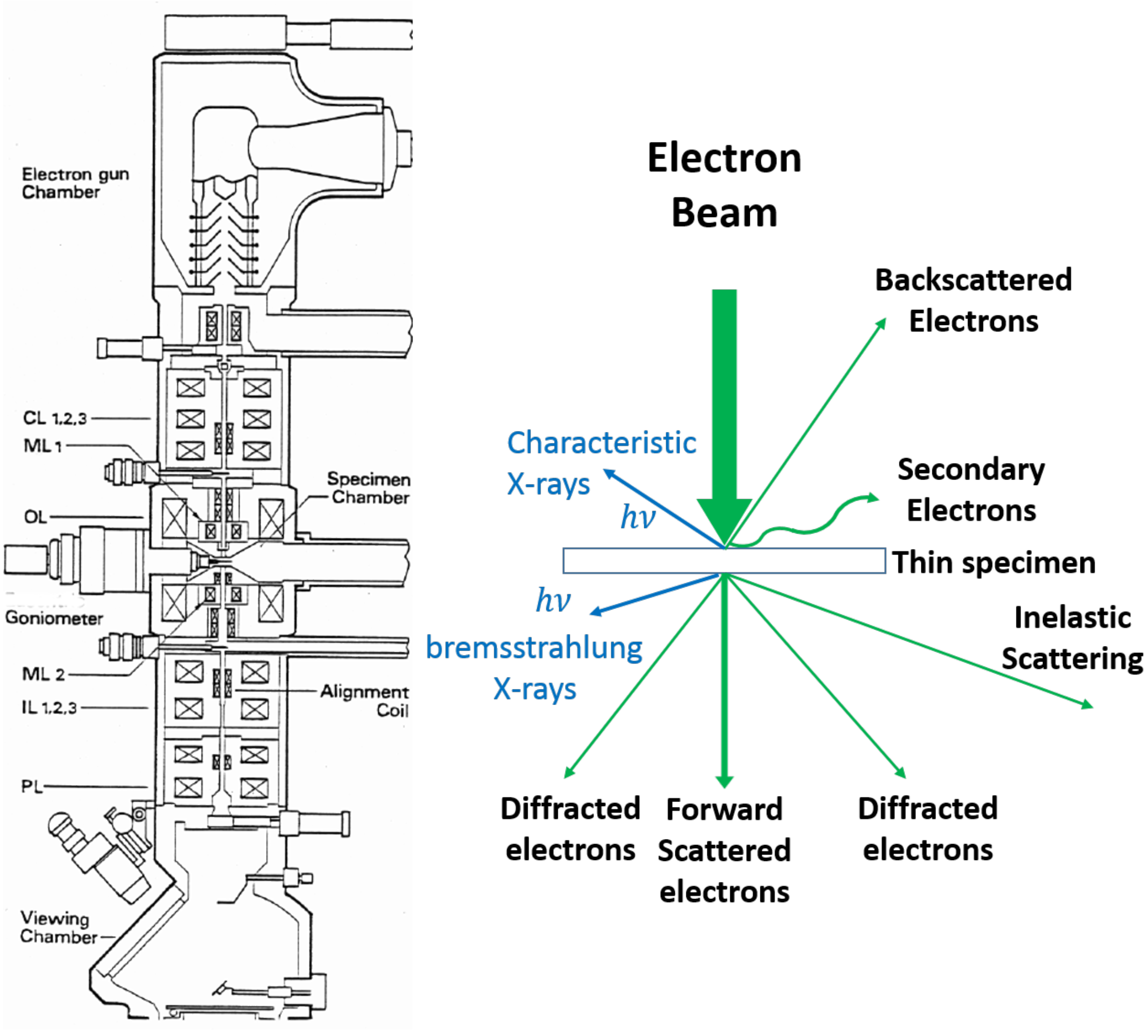
Electron gun Chamber
CL 1,2,3
ML 1
OL
Goniometer
ML 2
IL 1,2,3
PL
Viewing Chamber
Specimen Chamber
Alignment Coil
Electron Beam
Backscattered Electrons
Characteristic X-rays
hν
Secondary Electrons
Thin specimen
hν
bremsstrahlung X-rays
Inelastic Scattering
Diffracted electrons
Forward Scattered electrons
Diffracted electrons

Figure 2.1. Schematic (left) showing the electon gun, lenses, and specimen chamber in a modern TEM. Diagram (right) showing various electron-specimen interactions and signals that can be acquired in an electron microscope. TEM schematic adapted from JEOL USA.[29]

In reality, resolution will be limited by the electron optics rather than the wavelength.[30] Since electron microscopes use electromagnetic lenses, there are aberrations in the lenses that cannot be eliminated in the same way that optical lenses can by refinement of the manufacturing process. The alignment of the lenses, vibrations, and electromagnetic interference will all be additional limiting factors upon image resolution. Additionally, due to enhanced scattering and interactions with the sample compared with photons, transmission electron microscopes only work for thin samples. The advent of aberration correctors has helped to offset this to some degree, at the expense of adding significant cost and complexity to the microscopes.

For low-resolution imaging, the contrast is usually not terribly difficult to interpret. This is not the case for HREM. Interpreting these requires care, because the interaction of electrons with the specimen must be treated quantum mechanically. The image formation process consists of the incoming wave being scattered by the atoms in the sample, exiting as a wave with a phase shift related to the structure of the material, being modulated by the objective lens, and finally projected onto a detector and recorded as an image.[31]

The contrast results from the phase difference imposed due to both the sample and aberrations in the objective lens. Unless the sample is extremely thin and is imaged near the optimum imaging conditions with good microscope alignment, the astigmatism properly corrected, and the focus set to that of maximum contrast transfer, it is necessary to use image simulation to determine atomic positions from a HREM image.

2.2.2 Scanning Electron Microscopy

Scanning electron techniques use an electron beam which is a focused probe rather than a parallel beam. This probe is rastered back and forth across the sample to create an image. Several signals, including secondary electrons, backscattered electrons, and characteristic X-rays, can be collected in this operating mode. These each have varying levels of surface sensitivity, with secondary and backscattered electrons coming from the top 0.4-5 nm, and X-rays from several microns.

Scanning transmission electron microscopy (STEM) can be considered as a subset of TEM imaging. In this sense, the TEM convergence angle α is equivalent to the STEM collection angle β through time reversal symmetry. The primary advantage of STEM over TEM is that multiple signals can be recorded simultaneously, but at the expense of sequential, rather than parallel, spatially resolved image acquisition.

In the case of high angle annular dark field (HAADF), the image interpretation is easier. For high scattering angles, the technique will be sensitive to the thickness of the atomic column at the position of the beam. Additionally, the signal collected will be proportional to Z^n where $n = 1.5$–2. This is often called Z contrast in common parlance, but it is important to verify that the angular range is indeed large enough ensure that this is true. If the collection angle is at an intermediate range, diffracted electron beams from the sample can enter the detector. At this condition, contrast from different regions of a similarly stoichiometric material can appear brighter, which can mislead one to interpret the image as related to atomic number contrast. What is an appropriate collection angle is generally materials dependent.

Additionally, the use of a STEM allows for spatially resolved correlated imaging and spectroscopy in the form of energy dispersive spectroscopy (EDS) and electron energy loss spectroscopy (EELS). EDS (also known as EDX) arises from inelastic scattering events in which electrons in the material are promoted from core state (usually the K, L, or M shells) to vacuum. Another electron in an outer-shell state will decay into the hole and emit an X-ray with an energy characteristic of the energy difference between those two states. These X-rays can be collected be a detector and counted to obtain both qualitative and quantitative information about the elements present in a specimen. Quantitative analysis requires careful attention to X-ray absorbance and fluorescence effects, as well as elemental response factors.

EELS operates by measuring the energy change of the electrons which pass through a sample. The electrons which leave the bottom surface of the sample are collected and directed through a magnetic-prism spectrometer, where the energies are separated and projected onto a detector. Similar to EDS, the energy loss will be related to the elements present in the material.

2.2.3 X-ray Diffraction

X-ray diffraction (XRD) is a useful characterization technique to obtain structural information for a larger volume of material than possible with TEM. The interpretation of powder XRD spectra is simpler than electron diffraction because the kinematical scattering approximation can be used effectively in structure determination. XRD for large grains is governed by the Bragg law:

$$n\lambda = 2d\sin\theta, \tag{2.1}$$

where n is an integral multiple of the wavelength λ of the incoming X-ray, d is the interplanar spacing of the diffraction condition and θ is the scattering angle. XRD is particularly useful for determining material crystal structures. Typically a Bragg-Bretano geometry is used in which a diffractometer measured 2 times the scattering angle, in what is known as a $\theta - 2\theta$ scan. In the context of this dissertation, XRD is employed primarily for structure determination to confirm crystalline products of solvothermal synthesis.

2.2.4 X-ray Photoelectron Spectroscopy

X-ray photoelectron spectroscopy (XPS) is a characterization technique uses the photoelectric effect to eject electrons from the sample using an X-ray probe. The binding energy of the electrons is related to the kinetic energy (i.e. voltage) and the photon energy by the relation:

$$E_{bind} = E_{ph} - (E_{kin} + \phi), \tag{2.2}$$

where E_{bind} is the binding energy, E_{ph} is the energy of the incoming x-ray photon, E_{kin} is the kinetic energy of the ejected photoelectron and ϕ is the work function of the material. The energy of the X-ray probe is swept and the number of electrons ejected at some energy counted to determine the relative ratios of different elements and binding states present. This is a surface-sensitive technique, as only electrons from the first few tens of nanometers of material can escape from the surface to then reach the detector. Thus, it is useful to check the chemical composition and chemical state of constituents present near the surface of a sample.

2.2.5 Infrared Spectroscopy

Infrared spectroscopy is a technique that measures the vibrational response (photons) of a material using photons. The incoming photon wavelength ranges between 700 nm and 25 μm. This technique is particularly useful for probing bonding configurations of carbonaceous materials, which vibrate with characteristic wavelengths related to the bonding distance and symmetry. Additionally, spectra can be simulated from first-principles for known compounds. More details about the technique can be found in reference [32].

2.2.6 Physisorption

Gas phase physisorption measurements are a useful way to probe the surface morphology for powder samples. Typically adsorption isotherms are acquired by dosing known amounts of a carrier gas for a fixed volume and known amount of material. The temperature is held constant near the condensation point of the gas, and the pressure change is measured. The Brunauer–Emmett–Teller (BET) method[33] is commonly used to calculate the total surface area based upon the amount of gas adsorbed. Catalysis work described in Chapter 9 makes use of this technique.

2.3 Materials Synthesis

2.3.1 Solvothermal Synthesis of Oxide Nanomaterials

Solvothermal synthesis is a mature technique[34] for making a variety of oxide materials[16] spanning several length-scales. The method involves using aqueous solutions at high temperature and pressures that favor hydrolytic reactions. It is a technique inspired by nature, as many minerals are formed under these pressures in geological processes. What makes this technique interesting is the wide range of length scales of crystals produced, ranging from several meters in length[35] (see Figure 2.2) to a few tens of nanometers.[36,37] This flexibility is enabled by the use of different solvents and surfactants to allow control over both the morphology and the size of crystals. A recent review of using this technique to synthesize small particles of pyrochlore and perovskite materials appears in reference [38].

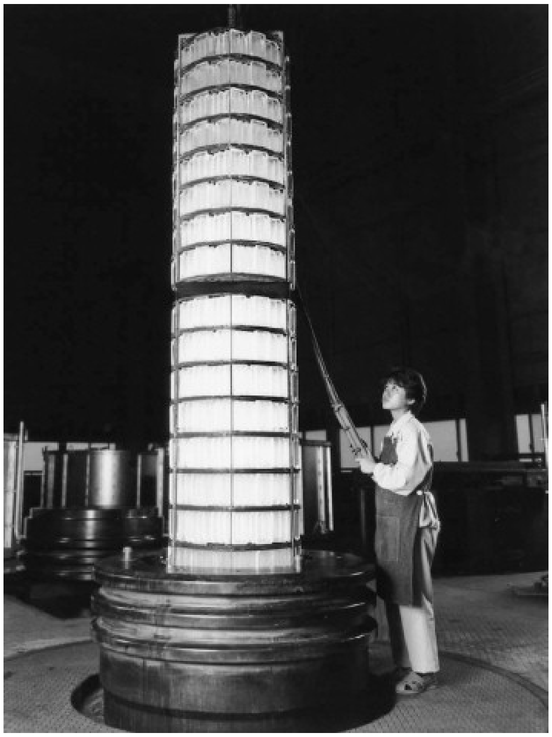

Figure 2.2. Illustration of scale of autoclave used to grow large single crystal of quartz, of several meters in length. Figure adapted from reference [35].

2.3.2 Sample Preparation

Nanoparticle TEM samples are generally prepared by dispersing a small amount of powder sample (on the order of a few mg) into solvent in a scintillation vial. It is important to ensure that the glassware used to disperse the nanoparticles is clean and free of hydrocarbons to prevent sample contamination. The choice of solvent (such as methanol, isopropanol, and hexane) depends upon the polarity of the material and the presence of adsorbed organic ligands. The choice of TEM grid is also important for imaging studies. Those with a thicker support, typically a carbon/polymer combination, reduce resolution by increasing the scattering of electrons after exiting the sample. However, depending upon the experiment, this may be an acceptable tradeoff for increased temperature stability for in-situ heating, as an example. Additionally, sample charging during imaging can be a frustrating occurence that degrades image quality, and can also be influenced by the choice of TEM grid (e.g SiN grids). In some cases, it is impossible to avoid, and can be managed by lowering the electron beam flux, and moving to different areas of the sample.

2.4 Modeling

2.4.1 Review of Basic Thermodynamic Functions and Materials Properties

The discussion in this section is based primarily upon the thermodynamics text written by Callen (see reference [39], primarily Chapter 2). Starting with the First Law of thermodynamics:

$$dU = \text{đ}Q + dW, \tag{2.3}$$

where U is the internal energy of the system, Q is the heat of the system, and W is reversible work. The total energy of an isolated system will be composed of the quasi-static heat added to the system and any work done on the system. Expanding work in terms of mechanical work and “chemical” work, we can rewrite this as follows:

$$dU = \text{đ}Q + dW_M + dW_C, \tag{2.4}$$

where W_M is the mechanical work and W_C is the chemical work. Finally, we can substitute for each of these quantities ($\text{đ}Q = TdS$, $dW_M = -PdV$, and $dW_C = \mu dN$) to obtain the more familiar form:

$$dU = TdS - PdV + \mu dN, \tag{2.5}$$

where μ is the chemical potential, N is the number of particles in the system, P is pressure, V is volume, and S is entropy. From this, we can assign definitions of temperature, pressure, and the chemical potential:

$$T \equiv \left(\frac{\partial U}{\partial S}\right)_{V,N} \qquad P \equiv \left(\frac{\partial U}{\partial V}\right)_{S,N} \qquad \mu \equiv \left(\frac{\partial U}{\partial N}\right)_{V,S}, \tag{2.6}$$

All of these are intensive quantities, meaning that they do not depend on the number of particles in the system. Using Legendre Transforms, we can define additional free energy functions. The Gibbs free energy is defined as:

$$G \equiv U + PV - TS, \tag{2.7}$$

with enthalpy defined as $H \equiv U + PV$ this becomes

$$G = H - TS, \tag{2.8}$$

In general, a chemical reaction will proceed if the Gibbs free energy of the products is below that of the reactants. For a system in diffusive equilibrium, the thermodynamic variable of interest is the chemical potential:

$$\mu \equiv -T\left(\frac{\partial S}{\partial n}\right)_{S,V} = \left(\frac{\partial G}{\partial n}\right)_{T,P} \tag{2.9}$$

where μ is the chemical potential, G is the Gibbs free energy, and n is the number of particles added to the system. Combining this with Equation 2.8 and differentiating we obtain:

$$dG = PdV + \mu dN - SdT, \tag{2.10}$$

which is the Gibbs-Duhem relation. In practice, when doing experiments, it is much easier to fix temperature, pressure, and volume as experimental parameters compared to entropy. Thus, in the literature, one almost always encounters free energy rather than the full internal energy of the system in question (and here, of course, we are ignoring rest mass and internal energy due to interatomic forces).

For considering surfaces and interfaces, we can modify the free energy by considering the energy cost to create a two-dimensional surface through the cleavage of bonds:

$$dG = P\,dV + \mu\,dN - S\,dT + \gamma\,dA, \tag{2.11}$$

where γ is a surface free energy term equal to $\partial G/\partial A$ and dA is the differential in area. These definitions will underly the work described in future chapters, both in terms of materials synthesis and observation of thermodynamic shapes.

2.4.2 Image Simulation

The mapping from a crystal structure to its image or diffraction pattern has been relatively well understood and documented. However, the reverse mapping from electron micrograph images to the crystal structure is generally more complicated. The fact that the images are two dimensional projections of three dimensional crystal structures, and that the contrast arises from nonlinear multiple scattering events makes it difficult to compare these projections to all plausible crystal structures. Hence, the use of numerical techniques to simulate results for different crystal structure is integral to the field of electron microscopy and crystallography. There are two common approaches to this problem: the multislice algorithm and the Bloch wave method. Here, we will focus on the multislice method, which is employed in later chapters for image simulation.

In 1957, Cowley and Moodie[40] showed that the Schrödinger equation can be solved numerically to evaluate the amplitudes of diffracted beam. By subdividing the material into slices, one can calculate the convolution of the electron wave from the electron source with the crystal potential and through the use of a propagator function, the amplitude and phase of the outgoing wave. (See reference [41] for a rigorous mathematical background.)

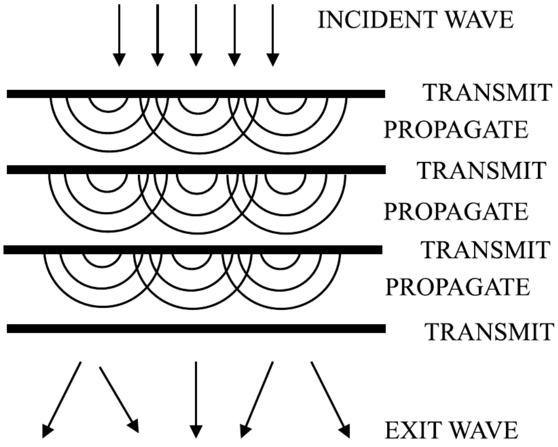

Figure 2.3. Schematic illustrating the scattering process that is calculated in multislice simulations. Figure adapted from reference [42].

The basic operating principle is to calculate diffraction from each layer of atoms using Fast Fourier Transforms (FFT) and multiplying by a phase grating term. The wave is then multiplied by a propagator, inverse Fourier tranformed, multiplied by a phase grating term yet again, and the process is repeated. The use of the FFT algorithm enables a significant computational advantage over the Bloch wave method in particular, since the

FFT algorithm involves $N \log N$ steps compared to the diagonalization problem of the Bloch wave solution which scales as N^2 where N is the number of atoms in the system.[42]

The most important step in performing a multislice calculation is setting up the unit cell and determining an appropriate slice thickness. In general, the unit cell used for simulating images will be different from the unit cell that defines the crystal structure of a particular material. The primary reason for this is due to aliasing effects which occur due wraparound errors in FFT calculations. The requirement to add additional "padding" to the unit cell has earned the nomenclature "super cell" and the requirement to add these additional pixels to the basic unit cell comes at a computational price.

Figure 2.4 shows a vector diagram of the wave-fronts being diffracted by the atomic planes in the sample. In the case of the small-angle approximation ($\theta \sim 100$ mRad) we can approximate the phase shift as $d - S \approx \frac{\Delta z}{\cos\theta} - \Delta z\theta$. For 100 mRad the difference is fleeting as $\cos(0.01) = 0.99995$ so $\frac{\Delta z}{\cos\theta} \approx \Delta z\theta$. For small angles this approximation holds regardless of how many slices there are, although choosing a Δz greater than the lattice parameter (or half the lattice parameter in the case of perovskites) for a multislice simulation is problematic.

Data Points	**$\log_2 N$**	**Discrete FT**	**Fast FT**	**Ratio**
64	6	4,096	384	10.7
128	7	16,384	896	18.3
256	8	65,536	2,048	32
512	9	262,144	4,608	56.9
1,024	10	1,048,576	10,240	102.4
2,048	11	4,194,304	22,528	186.2

Table 2.1. Computation speedup gained from the use of Fast Fourier Transform compared to Discrete Fourier Transform. Note that the speed scales logarithmically with size.

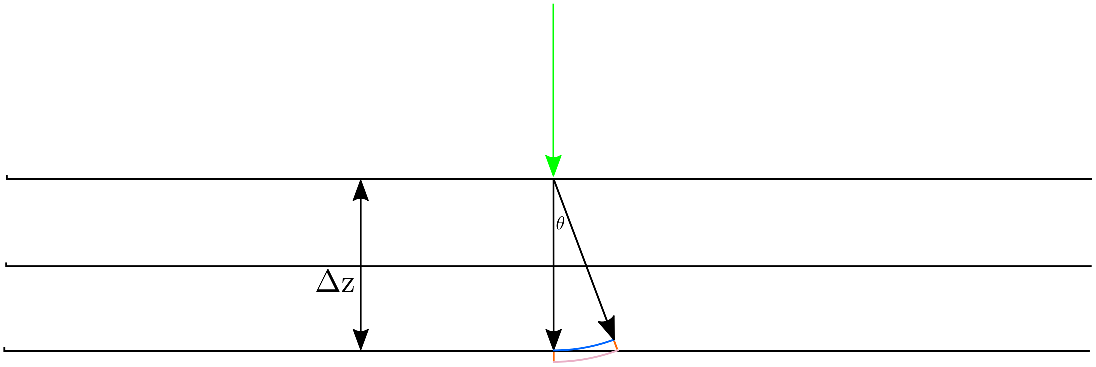

Figure 2.4. Schematic illustrating phase shift due to use of plane waves instead of spherical waves. This also demonstrates that choosing a slice thickness significantly smaller than the lattice parameter has little gain in accuracy

2.4.2.1 Quantitative comparison of image contrast

An experimental image can be quantitatively compared with a simulated image through the use of template matching. A robust method for doing so is through the normalized cross correlation coeffiecient (NCCC):

$$NCCC = \frac{\sum_x \sum_y \left(f(x,y) - \bar{f}_{u,v}\right)\left(t(x-u,y-v) - \bar{t}\right)}{\sqrt{\sum_x \sum_y \left(f(x,y) - \bar{f}_{u,v}\right)^2 \left(t(x-u,y-v) - \bar{t}\right)^2}} \tag{2.12}$$

where

$$\bar{f}_{u,v} \equiv \frac{1}{N_x N_y} \sum_{x=u}^{u+N_x+1} \sum_{y=v}^{v+N_y+1} f(x,y), \tag{2.13}$$

Here $f(x,y)$ represents the experimental image, t is the template or simulated image that is being compared directly with the experimental image, and (x, y, u, v) are the position and shifts in position of the template found relative to the experimental image. (See references [43, 44] for more details.) The result of the comparsion will yield a number between -1 and 1: -1 for perfectly inverted contrast, 1 for perfectly matching contrast, and 0 for no correlation between the images. This statistic maps the variation in contrast for an image to a single number for finding an “image inside an image.” One limitation is that it will normalize the contrast of both images prior to the comparison, so a large difference in dynamic range between the two images being compared will be lost. This method is useful for comparing simulated HREM images with experimental images, if the contrast and spatial dimensions are appropriately scaled.

CHAPTER 3

Wulff Shape of Strontium Titanate

3.1 Introduction

Crystal shapes are determined by a competition between thermodynamics and kinetics. In the thermodynamic limit—i.e. infinite equilibriation time with uninhibited growth of all possible crystallographic directions—the equilibrium, minimum energy shape is described by the thermodynamic Wulff construction.[45] Mathematically, the Wulff shape is defined as

$$S_W = \{\mathbf{x} \in \mathbb{R}^3 \mid \mathbf{x} \cdot \mathbf{n} \leq h(\mathbf{n}) \text{ for all normal vectors } \mathbf{n}\}, \tag{3.1}$$

where S_W is the set of all points $\mathbf{x}$ contained within a region bounded by at a distance $h(\mathbf{n})$ away from origin, for all directions that exist in the crystal as specified by the normal vectors $\mathbf{n}$.

Typically, the shape will be a convex polyhedron, with the same symmetry as the underlying crystal structure. In the early 20th century,[45] George Wulff postulated, without proof, that the equilibrium crystal shape which bears his name is uniquely determined by the surface energies of the various crystallographic planes. First we define the total surface free energy for the crystal:

$$G_{\text{surface}} = \int_{S_W} \gamma \, dA. \tag{3.2}$$

Ignoring effects from edges and corners—which is certainly valid in the large limit—the total surface free energy G_{surface} should be mimimized by holding the volume fixed and performing a variational minimization. By assigning surface energies γ_n to each family of crystal planes h_n, the optimal shape will be given by

$$\gamma_n = \frac{h_n}{\lambda} \tag{3.3}$$

where γ_n is the surface energy of a given facet, λ is a Lagrange multiplier, and h_n is the normal distance from the Wulff center to the plane. From this, it immediately follows that the ratios of the surface energies will be equivalent to the ratios of the facet normals, i.e.

$$\frac{h_n}{h_m} = \frac{\gamma_n}{\gamma_m}, \tag{3.4}$$

for arbitrary facets specified by n and m. This result is the basis of the work presented in this chapter.

Max von Laue[46] was the first to prove Wulff's theory mathematically. A more rigorous discussion can be found in work by Miracle-Sole[47] and Taylor.[48] Note that the Wulff construction is a model for pure crystalline materials, and does not take into account twinning, dislocations, or other defects. There are several extensions[49,50] to the Wulff construction that attempt to account for various parameters—such as twin boundaries, kinetics and compositional variation—and how they affect the shape of small crystals.

There should be one optimal geometric shape governed by the ratios of different surface energies for a particular material system or phase in thermodynamic equilibrium. (Both the crystal and its surroundings, be it vacuum, air, or a liquid must be taken into account.) A geometrical illustration of the minimization process, which is to take the inner envelope of tangents of the surface energy as a function of crystallographic orientation, appears in Figure 3.1.

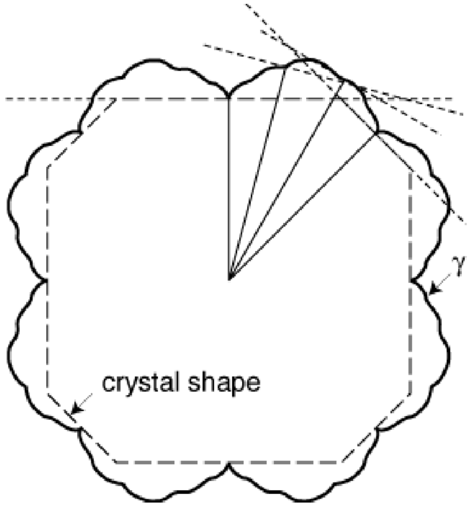

Figure 3.1. Geometrical illustration of the Wulff construction (also known as a gamma plot) in two dimensions. Image credit reference [51].

In practice, it is difficult to determine the surface energies of every family of crystallographic planes for crystalline materials to generate such plots. One can get estimates for them from *ab-initio* models, but these values are often only useful as a first approximation. The main limitations are the accuracy of functionals employed in density functional theory (DFT) calculations, the lack of entropic effects, and computational limits to calculate equilibrium with liquid and gas phases. Additionally, the surfaces of materials are often structurally different from simple bulk cleavage of the atomic planes, which will alter the surface energetics. Thus, it is rare to find accurate theoretical Wulff shapes for oxide materials, in particular, which can have significant variance in the surface free energies imposed by the surface chemistry and structure.

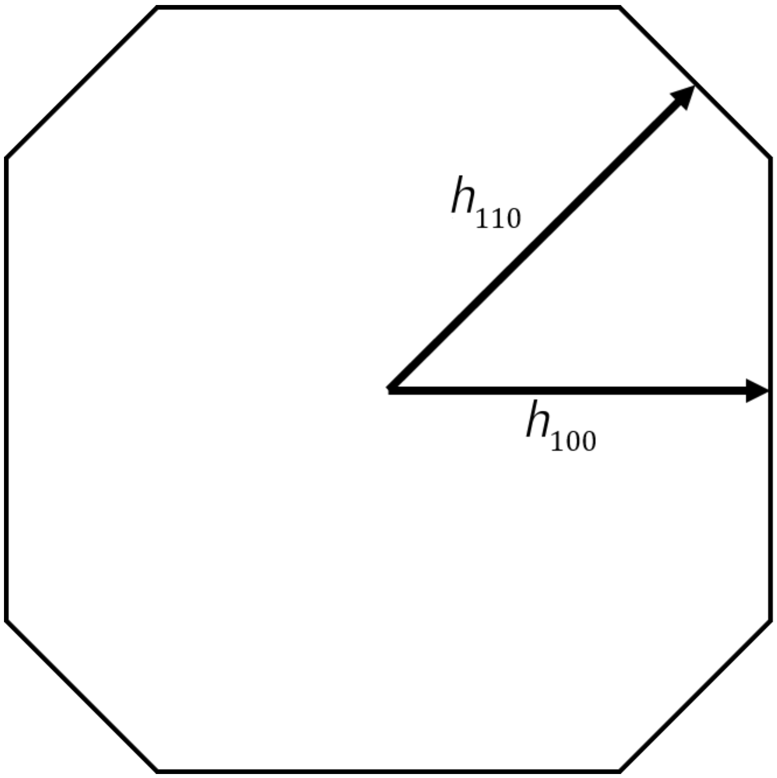

Figure 3.2. Illustration of the Wulff center measurement for the {100} and {110} facets.

3.2 Experimental Evidence of Wulff Shape

What follows is a description of experimentally observed shapes of STO nanocrystals which been grown and treated to transform to their equilibrium shape. The Wulff shape for this material was experimentally determined to be an octadecahedron, consisting of twelve {110} facets and six {100} facets as shown in Figure 3.3.

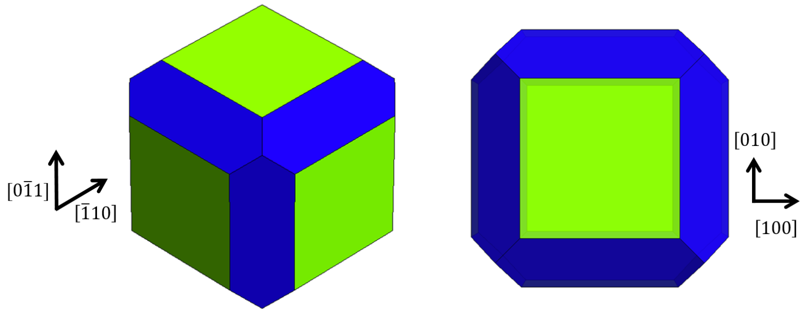

Figure 3.3. Observed octadecahedral Wulff shape for STO nanoparticles. Projections of the STO Wulff shape along the [111] zone axis (left) and [001] zone axis (right). The shapes were calculated using the WulffMaker Mathematica code[52] with {100} facets shown in green and {110} facets depicted in blue for a h_{110}:h_{100} ratio of 1.14.

3.2.1 Experimental Methods

STO nanocrystals were prepared by hydrothermal synthesis following the method developed by Rabuffetti *et al.*[53–55] Note that some samples were prepared by Dr. James Enterkin. Post-synthesis heat treatment of the nanocrystals enabled significant shape change through surface diffusion. By annealing for extended times, the shape should tend towards the minimum energy configuration.

TEM samples were prepared by sonicating a few milligrams of STO nanocrystals in a solution of high purity ethanol, then drop-casting them onto heat-resistant silicon nitride TEM grids. The TEM samples were subsequently loaded in an alumina crucible and annealed at different temperatures (700 °C to 950 °C in steps of 50 °C) for various times ranging from 5 to 20 hours in a fused silica tube within a tube furnace under flowing O_2 and in ambient conditions. It is important to note that many samples prepared in this manner exhibited significant sintering (see Figure 3.4); this could not be avoided except through control of the nanoparticle loading on the TEM grids.

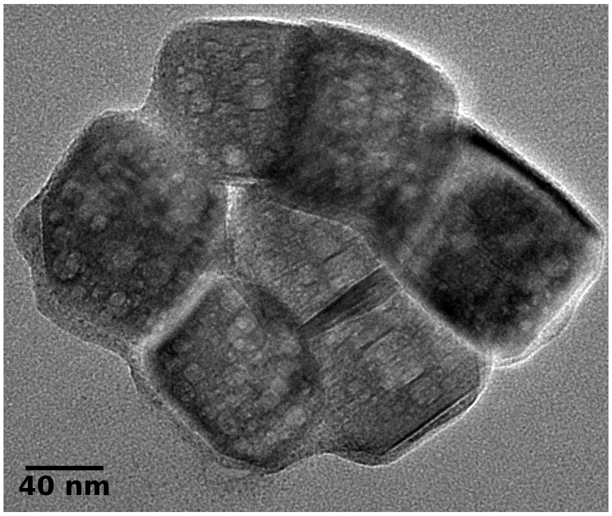

Figure 3.4. Sintering observed after annealing particles for 5 hours at 800°C under flowing O_2.

Imaging and transmission electron diffraction (TED) measurements for this study were carried out using a JEOL 2100F TEM. The TED measurements were used to determine the crystallographic orientation of several nanocrystals.

3.2.2 Image Analysis

Measurements of the nanoparticle faceting and corner rounding were carried out for several particles using bright-field TEM images. An example of a typical unnannealed nanocuboid with curvature of the nanoparticle corners appears in Figure 3.5.

To determine the Wulff shape, the following steps were carried out. First, the particles were tilted to the [100] zone axis. Next, the distance from the Wulff center of the respective face—either {100} or {110}—was measured for several nanoparticles. This

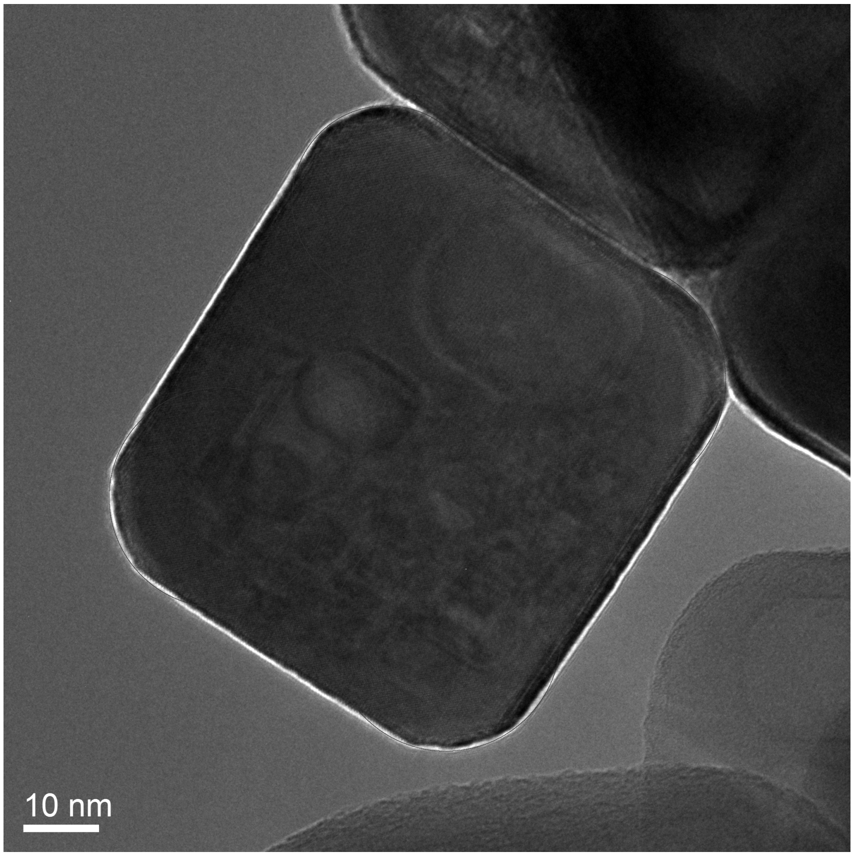

Figure 3.5. Example of typical, unannealed STO nanocuboid from hydrothermal synthesis using acetic acid. Note that there is predominantly {100} faceting with rounded corners. The radius of curvature was measured for several such particles: four corners were measured and the mean was calculated for each (see Figure 3.7 for plot summarizing these measurements).

yielded the h_{110}:h_{100} ratios, which are equal to the ratios of surface free energy per area via Equation 3.4.

The WulffMaker Mathematica code[52] was used to obtain graphical representations of the Wulff shape for different ratios of γ_{111}:γ_{110}:γ_{100}, with the values matching observed experimental images shown in Figure 3.3. Note that the appearance of {111} facets in the observed images depends upon the zone axis, because TEM collects two dimensional projections of three dimensional objects. Additional images were collected along the [111] zone axis to check for the presence of {111} facets. The observed hexagonal shape (see Figure 3.8) is evidence that little, if any, {111} facets are present in the particles measured. The ratios of h_{110}:h_{100} were measured for several images and the average (arithmetic mean) and standard error were calculated for each anneal condition using Equation 3.5. These statistics appear in Figure 3.6.

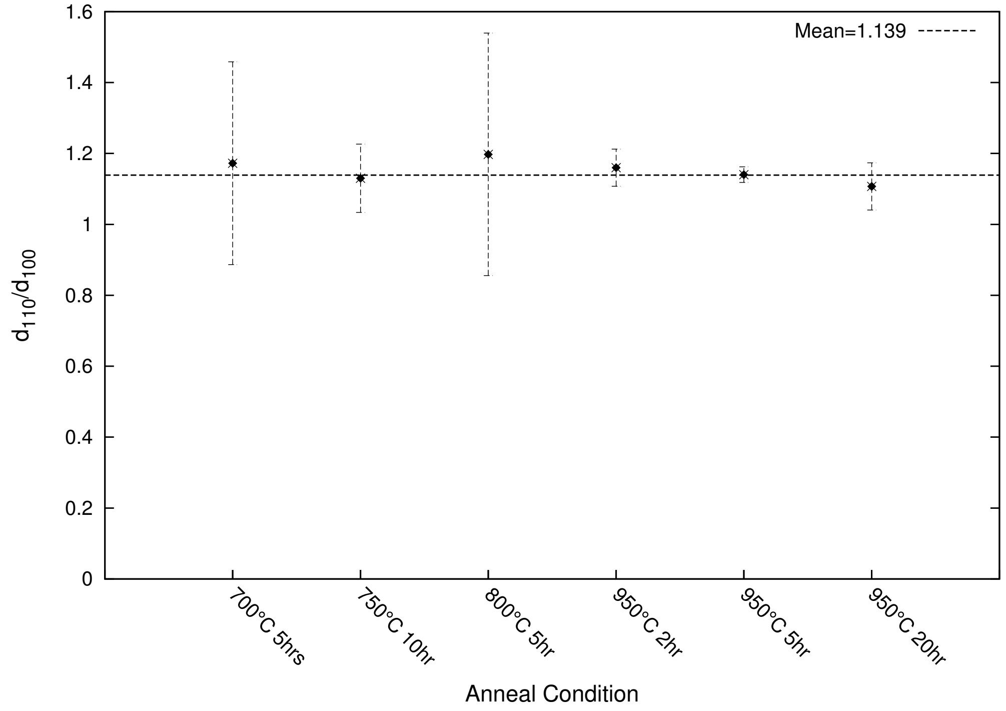

Figure 3.6. Surface energy ratios for various annealing temperature and times of STO nanocuboids.

The reported error was calculated using a two-tailed T-test, defined as:

$$T_{\alpha/2}\frac{s}{\sqrt{N}}. \tag{3.5}$$

The probability distribution function for the T distribution is defined as:

$$f(x) = \frac{\Gamma\left(\frac{\nu+1}{2}\right)}{\sqrt{\nu\pi}\,\Gamma\left(\frac{\nu}{2}\right)}\left(1+\frac{x^2}{\nu}\right)^{\frac{-\nu+1}{2}}, \tag{3.6}$$

where the gamma function $\Gamma(t)$ is defined as:

$$\Gamma(t) = \int_0^\infty x^{t-1}e^{-x}\,dx. \tag{3.7}$$

$T_{\alpha/2}$ is the critical T value (α=0.05 which is based on a 95% confidence interval), s is the sample standard deviation, and N is the sample size. All statistical analysis was performed using the t.test function of the stats software package written in the *R* programming language.

3.2.3 *Ab-initio* Modeling

DFT calculations of surface energies γ_{110} and γ_{100} were performed by Professor Marks using the WIEN2K code,[56] which uses all-electron augmented plane wave+local orbitals as the basis functions. The surface in-plane lattice parameters were set to those for the corresponding DFT optimized bulk cell, with ~1.6nm of vacuum to minimize artifacts from periodic boundary conditions. Muffin-tin radii were set to 1.55, 2.36 and 1.75 Bohrs for O, Sr and Ti respectively. The energy cutoff was set using min(RMT)*K_{max} (RK_{max}) of 8.0, with a 3×3×1 Brillouin-zone reciprocal space sampling of the primitive unit cell. The electron density and atomic positions were simultaneously converged using a quasi-Newton algorithm[57] to a numerical convergence of better than 0.01eV/1×1 surface cell. The PBEsol[58] generalized gradient approximation and the revTPSS method[59] were used, with 0.5 on-site exact-exchange—the optimized number for several test TiO_x units similar to earlier work by Kienzle *et al.*[60]

The surface enthalpy per (1×1) surface unit cell (H_{surf}) was calculated as:

$$H_{\mathrm{surf}} = \frac{(H_{\mathrm{slab}} - H_{\mathrm{STO}}N_{\mathrm{STO}} - H_{\mathrm{TO}}N_{\mathrm{TO}})}{(2N_{1\times 1})}, \tag{3.8}$$

where H_{slab} is the total enthalpy of the slab, H_{STO} for one bulk $SrTiO_3$ unit cell, N_{STO} the number of bulk $SrTiO_3$ unit cells, H_{TO} the enthalpy for bulk rutile TiO_2, N_{TO} the number of excess TiO_2 units and ($N_{1\times 1}$) the number of (1×1) cells. Consistency checks between the different functionals indicated an error in the energies of approximately 0.1eV/1×1 cell (~60 mJ/m^2, 8kJ/mole).

3.3 Experimental Results

The results of TEM imaging reveal a general cubic morphology with the {100} facets dominating, with rounded corners—thus dubbed “nanocuboids.” The corner rounding decreased after annealing for long time periods, after which significant coverage of {110} faces appears in the TEM images. The nanocuboids were single crystals as evidenced by the nanodiffraction measurements (see Figures 3.8 and 3.9).

HREM demonstrates that faces in the unannealed samples which appear curved at low magnifications are actually {100} and {110} step edges. There were also defects present within the nanocuboids with the same shape and faceting as the exterior surfaces. Thickness mapping measurements showed that these areas were thinner than the rest of the nanocuboids and thus they were identified as voids or cavities. Such voids have been observed in other work on hydrothermal synthesis.[61] It is likely that they result

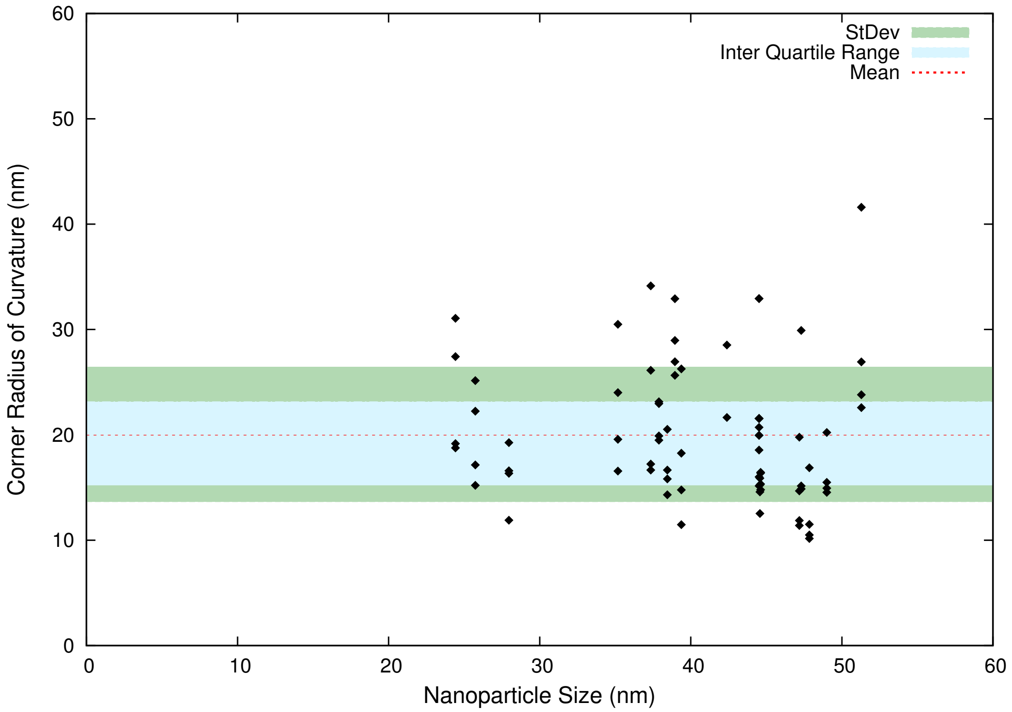

Figure 3.7. Measured radii of curvature for unnannealed STO nanocuboids.

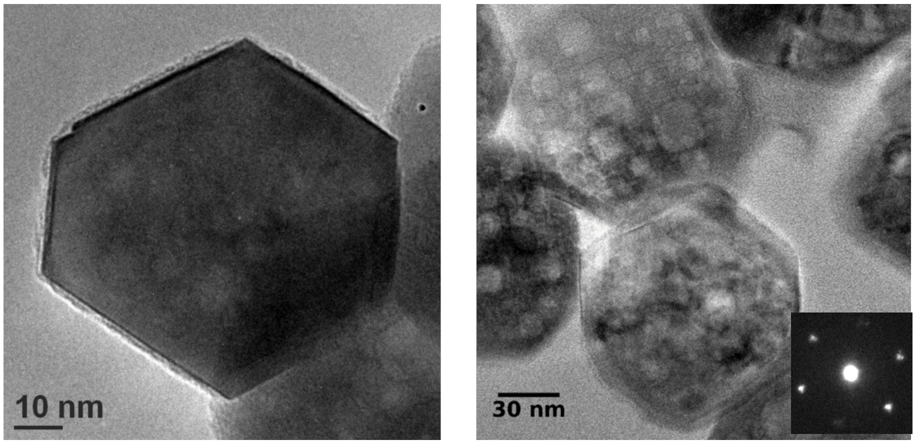

Figure 3.8. Nanoparticles imaged near the [111] zone axis, with diffraction patten demonstrating that it is a single crystal. Note the hexagonal shape of the nanocuboids projected along this direction, evidence that little, if any, {111} facets are present in the particles.

from inhomogeneous distribution of the strontium cations during the formation of an amorphous titanium-rich complex,[62] which then grow in size via the Kirkendall effect[63] upon crystallization during the hydrothermal treatment.

Measurements of h_{110}:h_{100} ratios for various annealing temperatures appears in Figure 3.6. The average h_{110}:h_{100} ratio calculated is 1.14 with a standard deviation of 0.055 with and a margin of error of 0.045. There is no evidence to suggest that increasing the annealing temperature had any effect on the changing the equilibrium surface faceting.

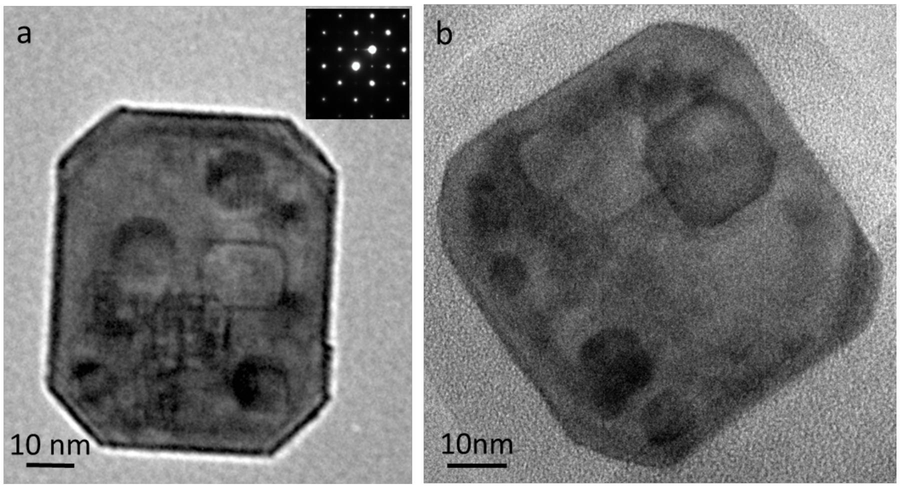

Figure 3.9. Post-annealed STO nanocuboids imaged along [001] zone axis. Note the sharp faceting in a), while b) has some residual corner rounding.

The voids observed in the unannealed samples remained after the annealing process. The voids measured were found to exhibit the same faceting as the external surfaces, as can be seen in Figure 3.9. The average size remained the same after annealing (see Figure 3.10).

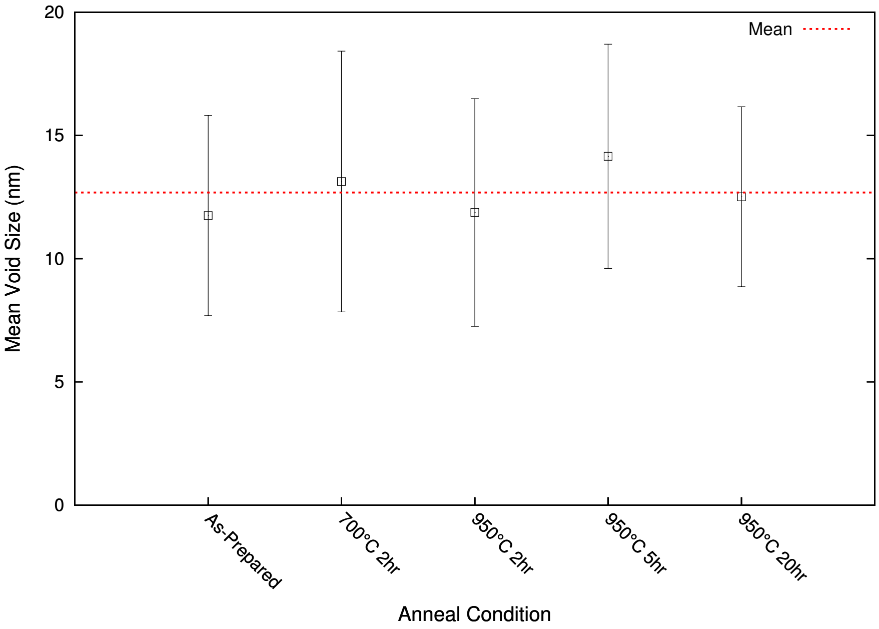

Figure 3.10. Mean void size versus anneal condition. The void size remained constant, on average, in spite of annealing.

3.4 Discussion

The minimum surface energy γ_{111} at which {111} facets begin to appear (noted geometrically by a shift from a hexagon to a dodecagon for the [111] projection) was found to be 1.3 times greater than the surface energy γ_{100}. Any surface energy larger than this would mean that {111} facets would not be a part of the geometrical solution for the thermodynamic shape. To preclude the possibility of higher order-facets being present, several images of nanocuboids along the [111] zone axis were recorded and revealed a general hexagonal shape. Note that unlike face centered cubic (FCC) materials, such as metals including Au, Ag, and Cu, STO is a simple cubic material with a five atom basis. If we consider the cations (Sr and Ti only), the structure is body-centered, with the {110} family as the close-packed planes. It is important to emphasize that this does not mean that such facets are not *stable*; rather, they are not optimal when taking the geometry of the crystal planes into consideration.

The fact that the nanocuboids largely maintained their shape before and after annealing, as evidenced by the h_{110}:h_{100} ratios remaining statistically unchanged, indicates that the shape we have observed is the thermodynamic limit and is representative of the Wulff construction.

Other shapes have been observed such as sharply faceted cubes in which the {100} surfaces dominate, and dodecahedra in which {110} dominate. In these cases, surfactants limit the rate of crystallization and growth on the respective facets, which is therefore a predominantly kinetic effect. Here, the high temperature processing after nanoparticle growth relies upon surface diffusion that will tend towards the thermodynamically favored shape after sufficient time has elapsed. The stabilization of the {110} facets occurs both on the surfaces of the nanocuboids and internally within the voids, further evidence of the thermodynamic stability of the {100} and {110} facets.

The comparison of the experimental results with DFT calculations is very informative, remembering that the latter are better at yielding relative energies than absolute values. A plot of calculated surface energy ratios for various surface structures on {100} and {110} surfaces based upon the DFT calculations is given in Figure 3.11.

The error bars correspond to the standard error of the measurements in question and the green overlay is the standard deviation of the experimentally measured value of $h_{110} : h_{100}$. A more complete comparison to experiment is to compare the ratio γ_{110}:γ_{100}, using an error of 0.13 for the DFT calculations based upon an uncertainty of 0.1 eV/1×1 unit cell.

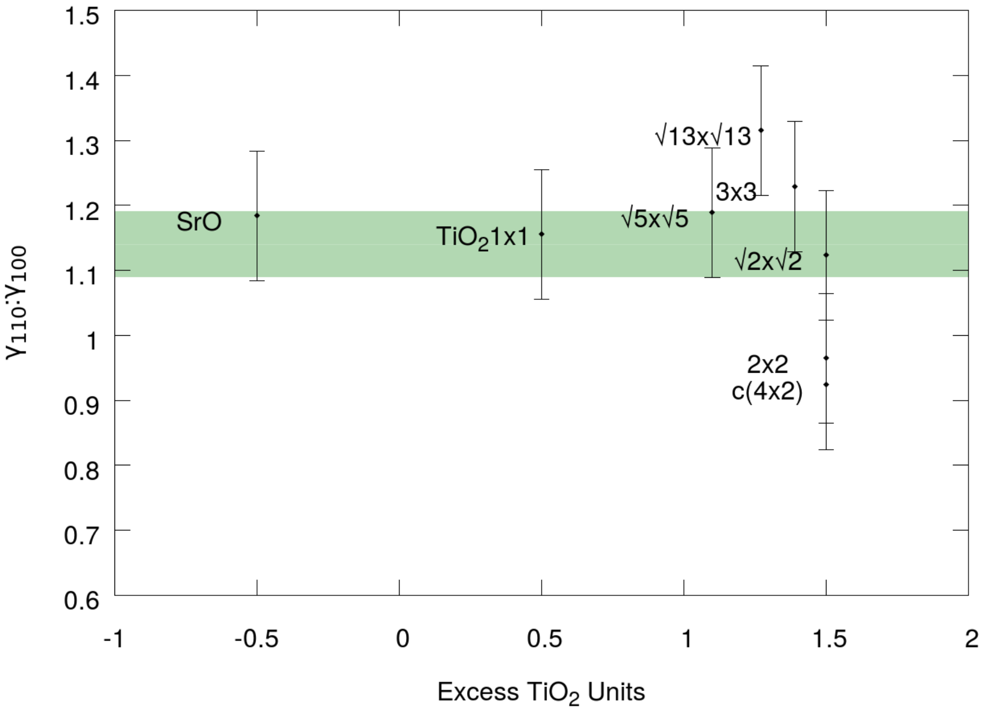

Figure 3.11. Surface energy ratios for various terminations of {100} and {110} facets of STO.

The DFT {110} surface energy was fixed as a linear combination of the 1×1 oxygen terminated surface and the (3×1) surface.[64] As we will see later, it would have perhaps been more appropriate to use a combination of the (3×1) and (4×1) as matches since these are the lowest energy structures from DFT calculations.

Given this, the agreement is between the predicted ratios $\gamma_{110} : \gamma_{100}$ and the experimentally measured ratios $h_{110} : h_{100}$ is reasonable. From the plot shown, there are several possible surface terminations that have the same ratio $h_{110} : h_{100}$ within both experimental and DFT error.

Based upon observations of unannealed nanocuboids by Dr. Yuyuan Lin[65] and work discussed in later chapters (see Chapter 7) the samples should be near the composition of the $(\sqrt{13}\times\sqrt{13})\,R$ 33.7° (RT13) reconstruction for the {100} facets,[60] perhaps in combination with the $(n \times 1)$ reconstructions (n=3, 4) for the {110} facets.[64] This combination of surface structures follows the convex hull for the two respective families of crystallographic planes, and should yield the lowest total surface free energy.

3.5 Conclusions

In this chapter, we discussed the methodology and measurement of the Wulff shape of STO. The equilibrium shape (with atmosphere) is a octadecahedron with $\gamma_{110} : \gamma_{100}$ ratio of 1.14. The reduction in curvature of the corners coupled with the similar shapes of the internal voids serve as additional evidence that the shape observed is the thermodynamic minimum.

CHAPTER 4

Synthesis and Characterization of {110}-Faceted Strontium Titanate Dodecahedra

4.1 Introduction

This chapter describes the synthesis of and characterization of {110}-faceted STO nanocrystals. By leveraging the powerful tool of profile view HREM imaging, we find through simulated image contrast that the surfaces match TiO_2-rich surface reconstructions. The structures which best match the experimental results were the $(n \times 1)$ reconstructions ($n = 3, 4$) previously observed on single crystals and solved by Dr. James Enterkin.[64,66] The observation of these complex surface structures illustrates why we cannot assume that nanoparticle surfaces terminations are simple 1×1 truncations of the bulk crystal structure.

4.2 Synthesis

STO rhombic dodecahedra were synthesized following a modified version of the method published by Dong *et al.*[67] The primary modifications are the use of titanium tetrabutoxide ($Ti(OBu)_4$) instead of titanium tetrachloride ($TiCl_4$) as titanium precursor, the use of strontium acetate ($Sr(Ac)_2$) instead of $SrCl_2$, and the use of sodium hydroxide (NaOH) instead of lithium hydroxide (LiOH). Additionally, the solution was not chilled in an ice bath. With these changes, the details of the synthesis are as follows:

Solution A was prepared by dissolving 9.1 mmol $Sr(Ac)_2$ into 40 mL of 1 M acetic acid while stirring. Solution B was prepared by adding 9.1 mmol $Ti(OBu)_4$ into 31.5 g of glycerol while stirring for at least 5 minutes. Solution A was then added into solution B while stirring for at least 2 minutes. Then 10 mL of 10 M NaOH was added dropwise while stirring. The resulting mixture (translucent yellow-white) was placed into a Teflon-lined autoclave for 36-48 hours of solvothermal treatment at a temperature of 240 °C, with ramping rate of 1 °C/min for the heating.

The resulting white powder was washed by suspension in water followed by centrifuging, which was repeated until the pH was neutral (7) as measured by pH strips. The powder was then dried in an oven at 80 °C overnight. TEM samples were prepared by suspending a few milligrams of powder in approximately 10 mL of ethanol and sonicating for 15 minutes. The dispersed nanoparticles were then drop-cast with a pipet onto lacey carbon TEM grids.

4.3 Characterization

The samples were characterized with several techniques, including XRD, TEM, and XPS. Further details can be found in the following sections.

4.3.1 X-ray Analysis

Powder XRD measurements to confirm the sample crystallinity were carried out by Dr. Bor-Rong Chen. The samples were prepared by compacting several grams of the powder sample into a pellet on a low-background glass slide. In order to identify the phase purity of the synthesized sample, the survey scattering profile was completed with an Ultima X-ray diffractometer (Rigaku), with a Cu Kα source operating at 40 kV and 20 mA. For measurements to determine the crystallite size, a Ge (111) monochromator attached to an ATXG X-ray diffractometer (Rigaku) was employed in order to minimize the instrument peak width. The XRD spectra were fingerprinted using the MDI JADE X-ray crystallographic database.

Figure 4.1 shows a $\theta - 2\theta$ XRD scan from 20° to 80° in which the Bragg peaks are indexed. From the XRD profile, all the major diffraction positions and the relative intensities of the peaks are consistent with cubic STO with a lattice constant of 3.903 Å. The most common impurties, namely $SrCO_3$ and oxy-hydroxides, were below the detection limit of the instrument.

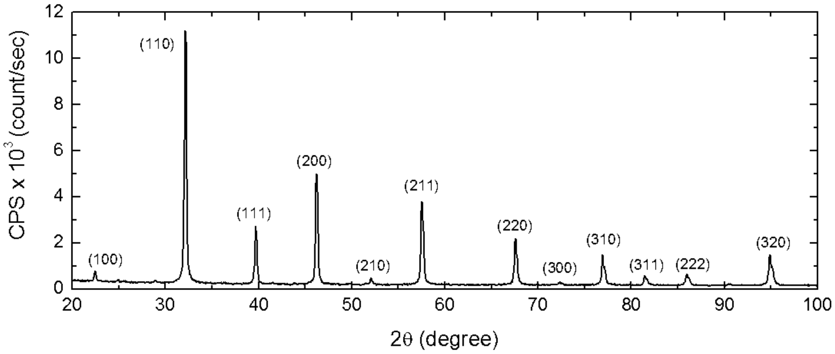

Figure 4.1. XRD $\theta - 2\theta$ scan for the dodecahedra indexed with cubic STO peak positions.

We can employ the Scherrer equation (Equation 4.1) to analyze the crystalline domain size of the nanoparticles:

$$L_{\text{hkl}} = \frac{K\lambda}{\beta \cos\theta}, \tag{4.1}$$

where L is the crystalline size in the [hkl] direction, K is the Scherrer shape factor, (usually a constant of 0.9), λ is the incident X-ray wavelength (1.542 Å for Cu Kα source), θ is the angular peak position, and β is the integral breadth. Figure 4.2a shows the (110) diffraction peak of the nanododecahedra, which was used for the fitting. The peak shape was fitted using a Lorentzian function given by

$$f(x) = A\frac{w/2}{(x - x_0)^2 + (w/2)^2} + Bx + y_0, \tag{4.2}$$

where A is the scaling factor, B and y_0 are fitting constants for the linear background, and the w and x_0 terms give the peak full width at half maximum (FWHM) and the position, respectively.

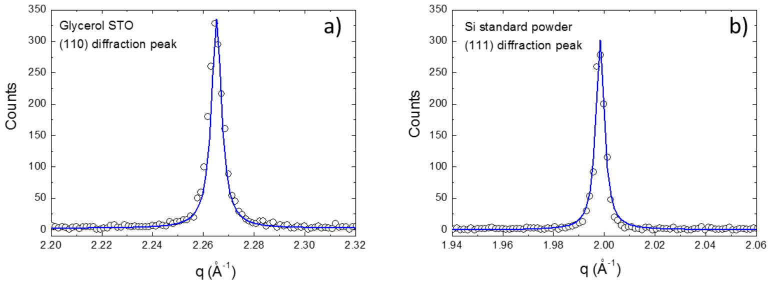

Figure 4.2. XRD rocking scan of a) (110) peak of STO dodecahedra and b) (111) peak of the 325 mesh Si powder. By applying the modified Scherrer equation (Equation 4.1), the mean crystallite size in the (hkl) can be determined from the broadening of the (hkl) diffraction peak.

The integral breadth (β) for Lorentzian peak shape is related with the FWHM via:

$$\beta = \left(\frac{\pi}{2}\right) \text{FWHM}, \tag{4.3}$$

The additional peak broadening by the instrument contribution was also taken into consideration in determining the peak broadening contributed by the crystallite size. 325 mesh single crystal Si powder was used as a standard to determine the instrumental peak width. The Si powder has a large crystallite size (44 μm), which minimized the peak broadening from size effects (Figure 4.2b). For Lorentzian peaks, the peak width due to the size of crystalline domains is obtained by subtracting the instrumental width from the measured peak width. This analysis led to an average crystalline domain size of 180 nm, which is consistent with that observed by TEM.

4.3.2 XPS Analysis

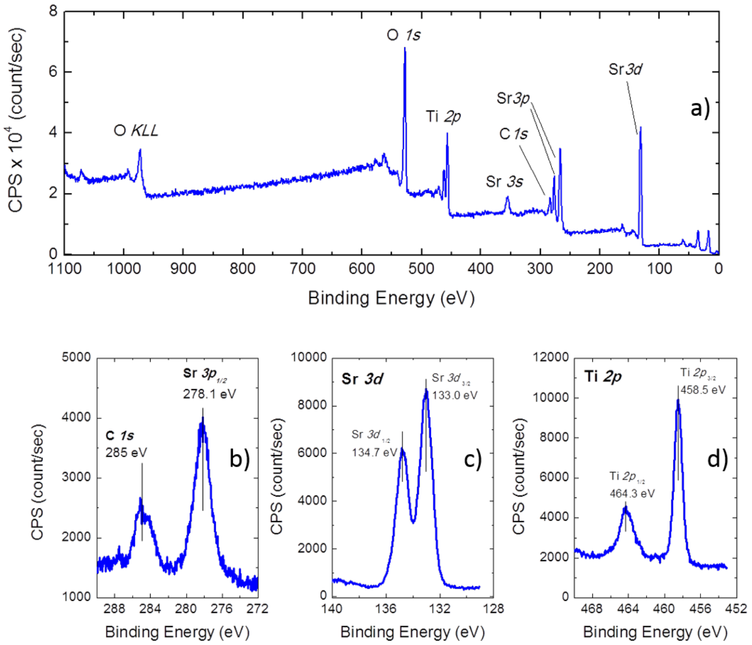

Figure 4.3. a) XPS Survey Spectrum as well as b) Sr $3p_{1/2}$ and C 1s peaks c) Sr 3d and d) Ti 2p peak positions.

XPS survey spectra were acquired using a Thermo Scientific ESCALAB 250Xi using a monochromatic Al Kα (1486.74 eV) X-ray source. The carbon 1s peak was calibrated to 285 eV. The peak positions of the core-level peaks of Sr, Ti and O elements (see Figure 4.3) are consistent with reference spectra for crystalline $SrTiO_3$.[68] There was no evidence of significant contamination or strongly adsorbed hydrocarbons.

4.3.3 Electron Microscopy

Electron microscopy was carried out using several microscopes, including a Hitachi HD2300 equipped with a secondary electron detector, a probe-corrected JEOL ARM

200CF at the University of Illinois at Chicago, and the Argonne chromatic aberration-corrected TEM (ACAT, a FEI Titan 80-300 ST with a C_s/C_c image corrector) at Argonne National Laboratory.

4.3.4 EDS Analysis

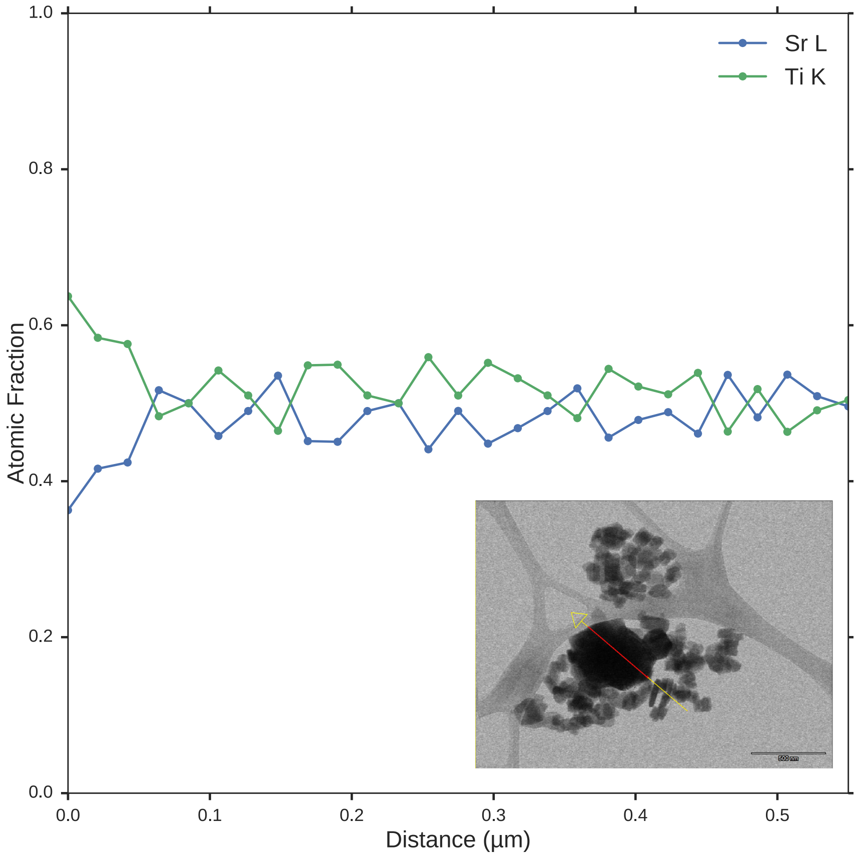

Figure 4.4. Plot of EDS linescan across nanoparticle with inset of a bright field image showing the location of linescan.

EDS using a Thermo Scientific dual-detector Si(Li) EDS system on the Hitachi HD2300 provided compositional information to complement the XPS for compositional analysis. The EDS linescan, processed with the Cliff-Lorimer method, (see Figure 4.4) show that the Sr:Ti ratio is approximately 1:1 across the particle, within the statistical error of the measurement.

4.3.5 HREM Quantitative Analysis

The MacTempasX software package, which implements non-linear imaging theory using the multislice method,[40] was employed to simulate the HREM images for quantitative analysis. The simulated imaging parameters were optimized to find the closest match to the real microscope conditions. This tuning was done using bulk motifs within the experimental dataset. The procedure for doing so was to first obtain reasonable estimates for the microscope parameters such as accelerating voltage, spherical aberration, focal spread, and beam tilt. To do so, a map consisting of a montage of simulated motifs was constructed using the crystal structure of the known material and the aforementioned parameters for a range of thicknesses and defoci, then used to qualitatively match the experimental results for the bulk unit cells. Next, the crystal tilt was varied in steps of 2 mrad and 5 degrees azimuthal rotation. Comparing several maps, the best qualitative results were chosen for further refinement using the normalized cross correlation coefficient (NCCC) statistic (see Equation 2.12 in Chapter 2). The imaging parameters were fitted as described in Chapter 2, with the quantitative comparison using the NCCC appearing in Tables 4.1,and 4.2.

Table 4.1. NCCF for experimental (left) and simulated (right) bulk motifs imaged along the [001] zone axis. The imaging parameters for simulated images for this zone were C_s=-0.005mm, C_5=0mm, α=0.5 mrad, and Δdf=30 Å.

Motif	Thickness (Å)	Defocus (Å)	NCCC
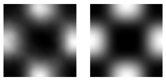	82	90	0.984
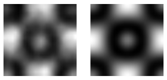	50	70	0.930
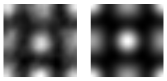	26	70	0.923

After maximizing the NCCC for the bulk simulated motifs, these results were then used to simulate several test surface structures without changing any of the optimized conditions.

Table 4.2. NCCF for experimental (left) and simulated (right) bulk motifs imaged along the [110] zone axis. The imaging parameters for simulated images for this zone were C_s=-0.015mm, C_5=0mm, α=0.5 mrad, and Δdf=30 Å.

Motif	Thickness (Å)	Defocus (Å)	NCCC
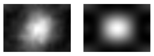	105	60	0.924
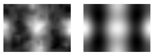	11	90	0.896
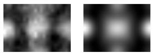	66	70	0.885

For particles imaged along the [001] zone axis, the thickness (see Figure 4.5a) follows the relationship $t = \frac{2\sqrt{3}}{3}x + t_0$ where x is the position relative to the edge and t_0 is the initial thickness. The corresponding form is $t = 2\sqrt{3}x + t_0$ for the [110] zone (see Figure 4.5b).

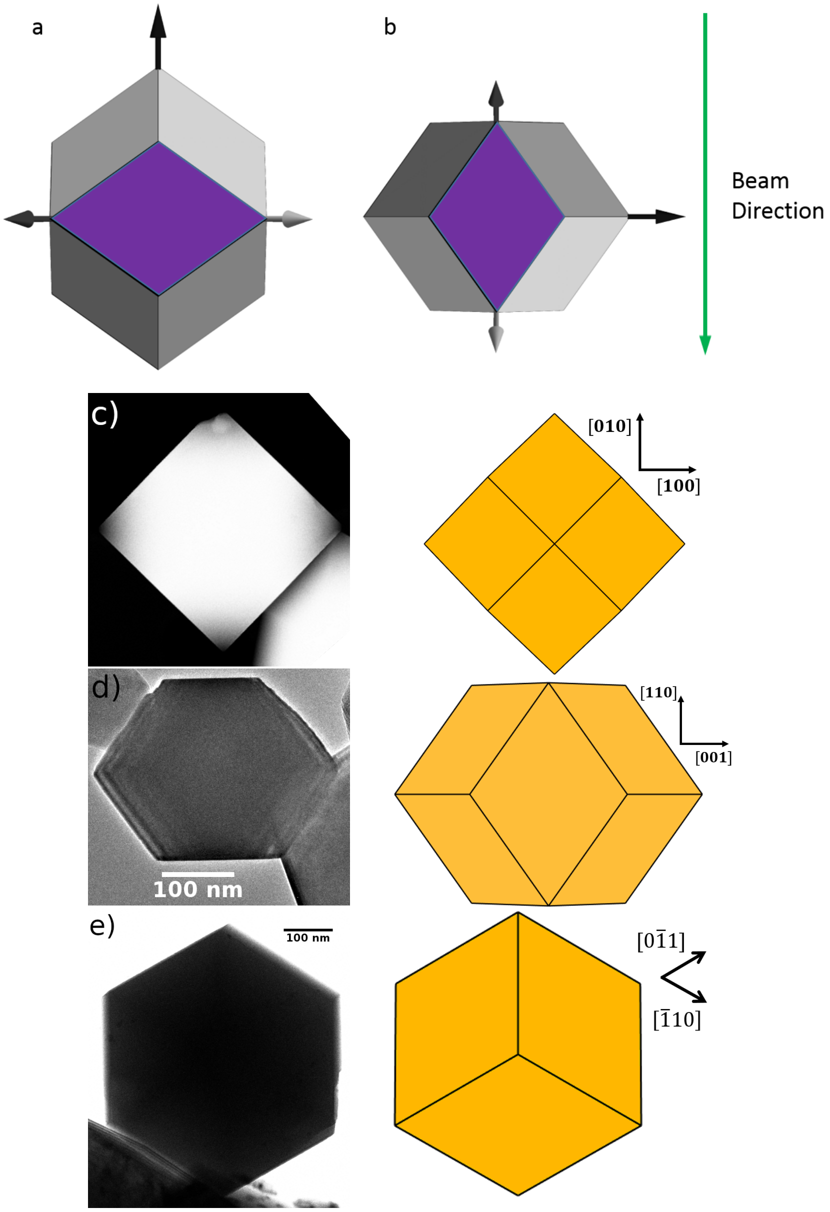
a
b
Beam Direction
c)
[010]
[100]
d)
100 nm
[110]
[001]
e)
100 nm
[0$\bar{1}$1]
[$\bar{1}$10]

Figure 4.5. Geometry of (110) facet in plan view when viewed along a) [001] and b) [110] zone axes. The electron beam direction is parallel to the facet. Top-down projections of the rhombic dodecahedron along several low-index zone axes appear below. The [100] (c) and [110] (d) projections show different thickness gradients from the edge of the particle to the center. The top shows the [111] projection (e) with constant thickness at the edge of the polyhedron.

4.4 Results

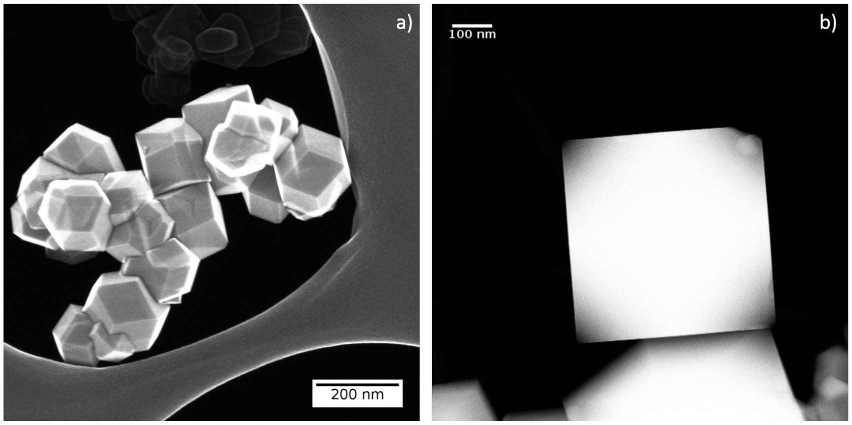

Figure 4.6. Low magnification SEM a) and HAADF b) images demonstrating dodecahedral shape of the nanoparticles. The three-dimensional character is evident in a), and shows in b) via the intensity changes.

The general morphology of the resulting nanoparticles was dodecahedral with predominantly {110} faceting as shown in a secondary electron microscopy (SEM) image in Figure 4.6a. There was additional minor faceting present, as {001} is visible at high magnification (Figure 4.7). The particles were phase pure as verified by XRD (Figure 4.1) with an average domain size of 180 nm, with minimal surface contamination evident in the XPS results (Figure 4.3) and no evidence for any variations in composition based upon the EDS results (Figure 4.4). While there were particles that exhibited sintering, the majority of the particles imaged exhibited sharp faceting with little, if any, corner rounding. Additionally, there was no evidence of dislocations, twins, or other defects in the TEM data. When imaged along the [001] direction with high angle annular dark-field (HAADF), the reduced contrast of the dodecahedra is consistent with thin areas at the corners as shown in Figure 4.6b. This is visible in Figure 4.7 which shows that the corners are atomically flat at the edges for two different nanoparticles.

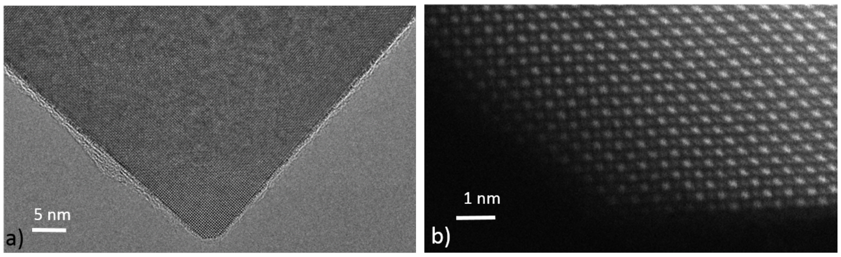

Figure 4.7. High-resolution a) CTEM and b) HAADF images from two different nanoparticles showing atomically sharp faceting.

4.4.1 HREM Imaging and Simulations

Utilizing the tool of profile-view imaging[4] we observed the surface structure of the nanoparticles along two zone axes. By comparing the observed experimental contrast with simulated images for both SrTiO and O terminated surface (the two possible nominal (1 × 1) bulk truncations) it is clear that neither is a plausible structural match (see Figures 4.9 and 4.12). The (3 × 1) and (4 × 1) reconstructions, whose structure is reported previously[64] were used as the basis for additional simulations.

The defocus/thickness maps compared with wide area HREM experimental images for both the [001] and [110] zone axes (see Figure 4.8) show good qualitative agreement.

When viewed along the [001] direction (see Figure 4.10) there is an additional corrugation of the {110} surface along the $[1\bar{1}0]$ direction. As shown in the inset, this can be explained by either of the (3 × 1) or (4 × 1) reconstructions.

Comparing the contrast between the simple (1 × 1) truncations, one can see subtle differences. For instance, there is an additional small bright spot below the surface arrowed in Figure 4.10 which is not present with a simple bulk termination. With respect to quantitative agreement, the cross-correlation values were 0.79 for the (3 × 1) and 0.77 for the (4 × 1) along the [001] zone.

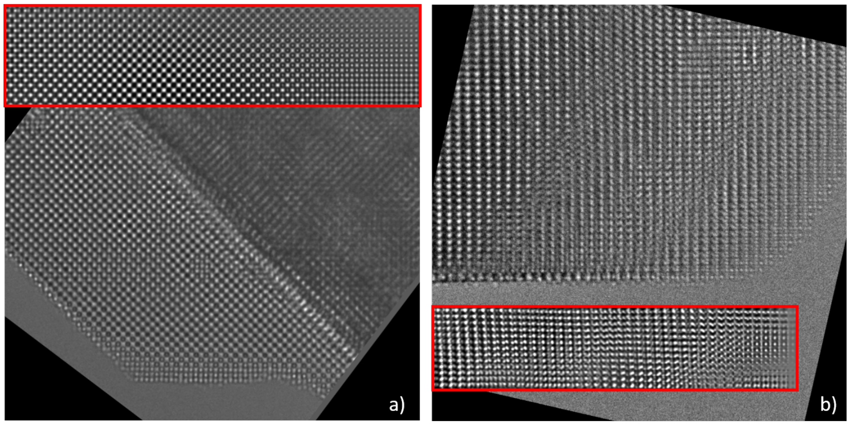

Figure 4.8. Defocus/Thickness map for sample viewed along the [001] zone axis , shown in a) and [110] zone axis, shown in b). Note that for a) there another particle directly behind the thin region which causes a rapid, stepwise increase in thickness.

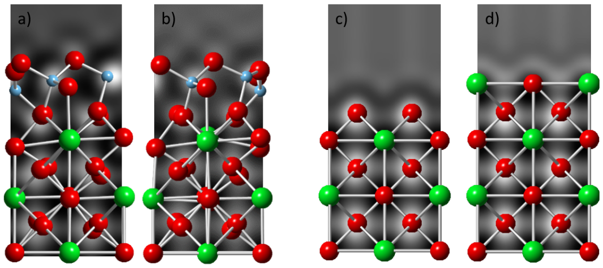

Figure 4.9. Atomic model overlaid with simulation with optimal parameters (defocus-50 Å, thickness 58 Å) for a) (3 × 1) and b) (4 × 1) c) O and d) SrTiO along [001] zone axis

As a secondary check results for the [110] zone axis are shown in Figure 4.11 which confirm the interpretation that the surface is likely a mixture of several (n × 1) reconstructions with (3 × 1) and (4 × 1) yielding the best match. The best cross-correlation values for the (3 × 1) and (4 × 1) were 0.69 and 0.65 respectively.

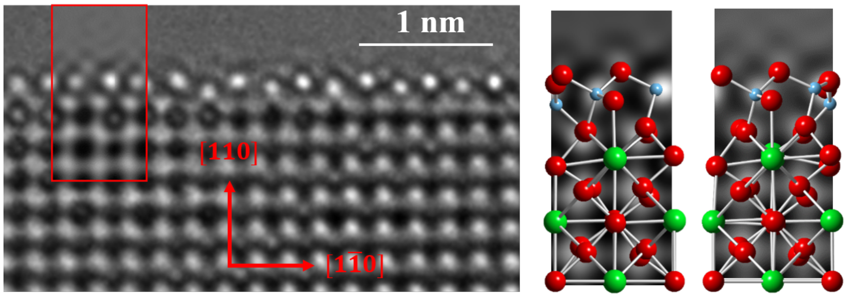

(3 × 1) **(4 × 1)**

Figure 4.10. a) Experimental profile image down the [001] zone, with an image simulation (red box) for a (3 × 1) reconstruction inset. In b) image simulations for the (3 × 1) and c) (4 × 1) reconstructions are shown with the atomic structure superimposed. The (3 × 1) gave the best fit to experiment for this area, although in other regions it was the (4 × 1).

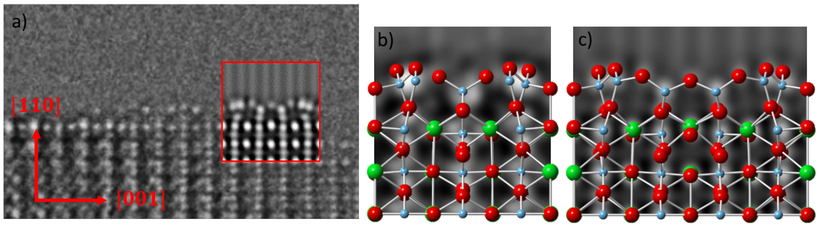

Figure 4.11. a) Experimental profile image down the $[1\bar{1}0]$ zone, with an image simulation (red box) for a (4 × 1) reconstruction inset. In b) image simulations for the (3 × 1) and c) (4 × 1) reconstructions are shown with the atomic structure superimposed. The (3 × 1) gave the best fit to experiment for this area, although in other regions it was the (4 × 1).

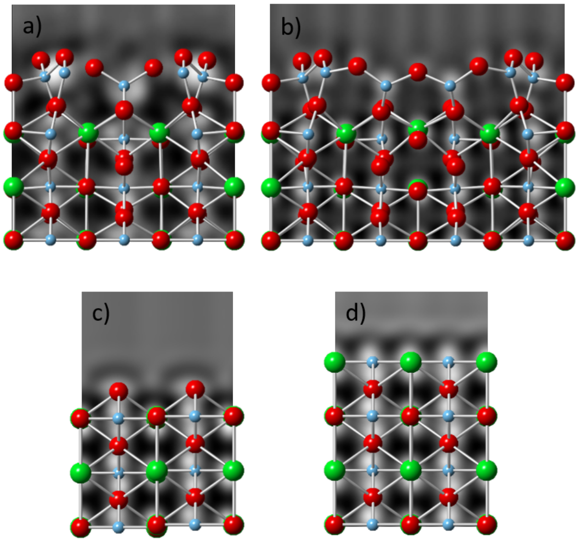

Figure 4.12. Atomic model overlaid with simulation with optimal parameters (defocus-60 Å, thickness 6 Å) for a) (3 × 1) and b) (4 × 1) c) O and d) SrTiO along [1$\bar{1}$0] zone axis

4.5 Discussion

The shape of a nanoparticle is controlled by a combination of factors involving both the nucleation of new steps as well as the relative energies and chemisorption characteristics of different surfaces. During solvothermal synthesis there is exchange between the surface of the oxide nanoparticles and the surrounding solute. At lower $\mathrm{pK_a}$ the {001} facets are growing fast, so vanish from the kinetic-growth shape; at higher $\mathrm{pK_a}$ the situation reverses and the {110} facets are growing out of existence. We note that the results of Dong et al.[67] indicate sharp corners and edges at high $\mathrm{pK_a}$, indicators of kinetic control with a relatively large chemical potential difference between the solid and surrounding fluid. The corners and edges of the nanoparticles were sharp, which indicates that the chemical potential difference between the solid and the surrounding environment was relatively large[69] and that the overall growth was via a kinetic-Wulff construction route (see reference [70] and references therein). We did not observe significant crystal defects for samples which contained quite large particles, which indicates conventional nucleation and growth. Other similar syntheses have been demonstrated to have growth affected by confinement of liquid crystal microemulsion[71] as well as shrinking and Ostwald ripening.[72] An overview of some of these terms as well as additional literature can be found in a review by Marks & Peng (reference [70]).

It is known that the synthesis conditions can stabilize different crystallographic facets, and even different chemical environments for a given facet.[65] The structure of a surface, on both bulk crystals and nanocrystals, is determined by thermodynamics, kinetics, or a combination of the two. In this synthesis, glycerol served as either a co-solvent, surfactant, or both. Both solvents and surfactants can alter the kinetics of growth and the thermodynamics of which surface is lowest in energy. Since {110} facets are small for the Wulff shape in oxygen, as shown in Chapter 3, glycerol has clearly had a significant effect to preferentially stabilize {110} facets.

Dong *et al.*[67] experimentally establish a correlation between the faceting and the pK_a and concentration of the polyol added to the system: more {110} at lower pK_a i.e. more acidic surfactants/solvents. To understand this, they performed DFT calculations to calculate the adsorption energies of water, methanol, and ethylene glycol on a simplified model of the surface. From the observed contrast in Figure 4.12, the bulk truncations clearly do not match the simulated contrast at the microscope conditions obtained from bulk tuning. Moreover, accurately modeling adsorption of organic ligands to a crystalline material is decidely nontrivial.

The results presented here indicate that the true surface is more complex, and matches well with titanium-rich structures of the $(n \times 1)$ reconstructions. In our case the reconstructions on the {110} surfaces are stabilized during the nanoparticle growth phase, and remain stable in air as the samples are stored at ambient conditions. The $(n \times 1)$ reconstructions, previously obtained on bulk (110) single crystal surfaces using buffered etching followed by high-temperature annealing,[64] both lie along the convex hull for known (110) surface reconstructions. The (4×1) has a surface TiO_2 excess of about 1.5 per 1×1 surface unit cell, while the (3×1) has an excess of 1.67. These structures, previously observed on annealed bulk single crystal samples of (110) STO, were solved via direct methods analysis[73] of transmission electron diffraction data combined with refinement using density functional theory.

4.6 Conclusions

In summary, the {110}-faceted STO nanoparticles have surfaces which matche well with the (3×1) and (4×1) surface reconstructions. This is noteworthy because of the different methods by which these surfaces were obtained: the bulk samples by mechanical polishing, ion beam thinning, buffered etching, and subsequent annealing at high temperatures; the results herein by wet chemical synthesis via solvothermal preparation of nanoparticles at comparatively moderate temperatures and highly alkaline conditions. While different methods will yield different kinetic routes to surface structures, the thermodynamics will always be important. Furthermore, this serves as a reminder that the atomic structure of nanoparticles needs to be considered as a surface science problem.

CHAPTER 5

Synthesis and Characterization of Strontium Titanate Nanocuboids

5.1 Introduction

We have already established that hydrothermal synthesis (solvothermal, more generally) is a versatile method for growth of metal oxides. Appropriate choice of reaction conditions and starting materials allows for a wide range of possibilities in terms of both crystal phase, size and shape. Additionally, it is possible to control not only the crystallographic faceting, but also surface chemistry, through the use of solvents, acidity, and surface active agents—also known as surfactants.

5.1.1 Motivation

Previous work done by Dr. Yuyuan Lin (see reference [65]) has demonstrated that the surface termination of STO nanocuboids can be controlled through synthetic conditions. Specifically, strontium-rich surfaces were obtained when oleic acid (IUPAC name octadec-9-enoic acid) was used as the surfactant. By comparison, acetic acid (IUPAC name ethanoic acid) yielded titania-rich surfaces. Specifically, the formation of a lamellar liquid microemulsion was believed to lead to the growth of sharply faceted nanocubes with an average size of 20 nm with SrO terminated surfaces for the oleic acid synthesis.[71] We will briefly discuss surfactants, more generally, and the differences between these molecules, to motivate the study of similar systems with the goal of achieving control over the surface chemistry.

5.1.2 Background: Surfactants

A surfactant is an amphiphile, which is a molecule that has both a hydrophobic and hydrophilic tail.[74] These are generally organic molecules, and typical examples include phospholipids and polyethlyene glycol ethers. They can be further classified as ionic and non-ionic, which depends on the hydrophilic end group chemistry. Surfactants have many applications, the most common of which is use as detergents.

It is quite common to use surfactants of various forms in colloidal nanoparticle synthesis. The polarity of the surfactant molecule can have significant effects upon the growth process by preferentially stabilizing certain crystallographic facets once the critical nucleus size has been surpassed. Additionally, the surfactants can also phase separate in distinct and interesting ways.

Figure 5.1 shows several possible structures of liquid crystals in microemulsions. Both spherical micelles and cylindrical micelles, a form of lipid bilayer, can form more complex arrangements, such as the cubic phase, hexagonal phase, and the lamellar phase. A review article by Corkhill *et al.*[75] explains in greater detail the thermodynamics behind these

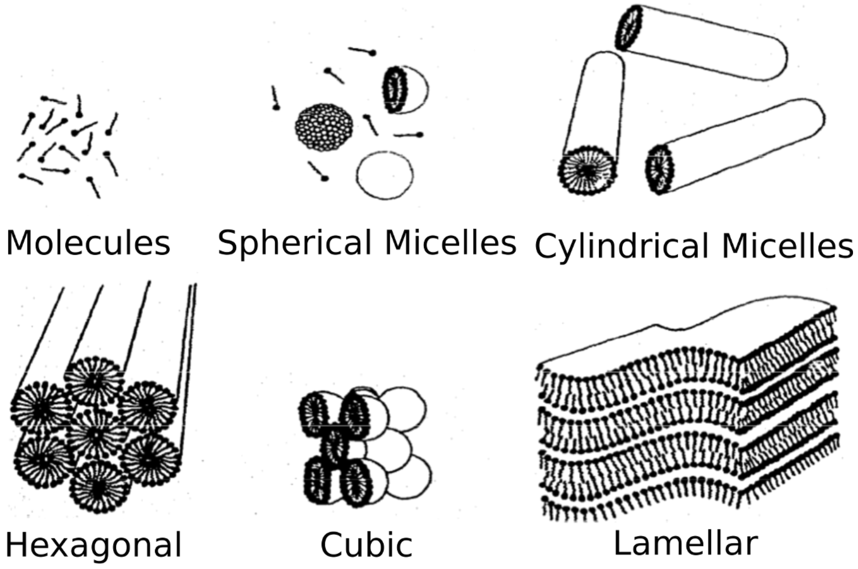

Figure 5.1. Illustration of different physical configurations of microemulsion of a surfactant and water as function of concentration. Figure adapted from reference [74], pg 7.

various phases for non-ionic surfactants in water. The formation of various molecular aggregate phases is an energy balance between the removal of the hydrophobic alkyl chains from the aqueous solution with the increase in packing of the hydrophilic head groups. It is generally non-trivial to make accurate predictions because of the complex interactions between the solvent and the functional groups, which will have both inter- and intra-molecular forces.

Phase stability diagrams are typically constructed from experimental data, using techniques such as optical microscopy, electron microscopy, and small angle X-ray scattering (SAXS) under a variety of experimental conditions. They are then extrapolated to other conditions based upon thermodynamic models. An example of a such a phase diagram appears in Figure 5.2.

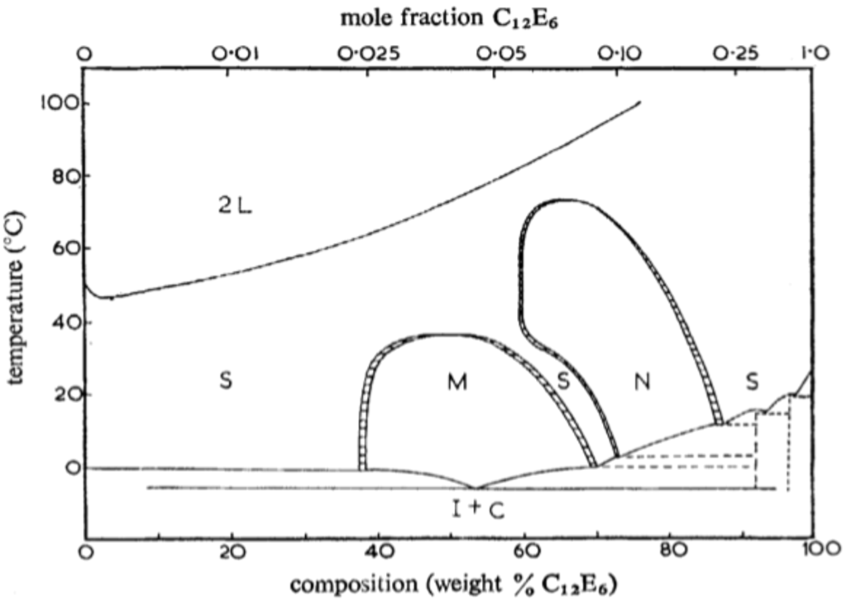

Figure 5.2. Temperature stability phase diagram of $C_{12}E_6$ as function of surfactant concentration, adapted from reference [75]. S corresponds to an isotropic solution, 2L the co-existence of two isotropic liquids, M middle (hexagonal) phase, N neat (lamellar) phase, C crystalline hydrates, and I ice.

5.1.3 Carboxylates

Both oleic acid and acetic acid are considerably simpler molecules than the surfactant described above. As carboxylates, they both are terminated with a $-COOH$ group. In solution, this group can donate a proton to form a $-COO^-$ group, and the resulting negative charge can be stabilized through resonance between the deprotonated oxygen and the carbonyl group. The length of the attached alkyl group will impact the stability of this charge, which will determine the equilibrium concentration of donated protons.

This is simply a description of the acidity of the molecule, which for weak acids is well-described by the Henderson-Hasselbalch equation:

$$HA + H_2O \rightleftharpoons H_3O^+ + A^- \tag{5.1}$$

$$K_a = \frac{[H_3O^+][A^-]}{[HA]} \tag{5.2}$$

$$pK_a = -\log_{10} K_a. \tag{5.3}$$

Here HA is a weak acid, A^- is the conjugate base (a salt), $[H_3O^+]$ the equilibrium concentration of protonated water, [HA] the equilibrium concentration of the weak acid, and $[A^-]$ the equilibrium concentration of conjugate base. The parameters K_a and pK_a are the acid dissociation constants and the logarithmic acid dissociation constant. Typically one will find pK_a values reported in the literature for various substances. The reported pK_a values for oleic acid and acetic acid are 9.85 and 4.74, respectively[76]—a difference of five orders of magnitude. As a point of reference, the pK_a of hydrochloric acid, a strong acid, is –6.[77]

The length of the hydrophobic group will have an impact upon the packing density of the molecules (see Figure 5.3 for illustration for carboxylic acids). Furthermore, this packing behavior will be altered by pH as well as the presence of surfaces and interfaces.[78] These two factors will contribute significantly to determine the final products, namely the shape and surface chemistry, when used as templates in nanoparticle synthesis.

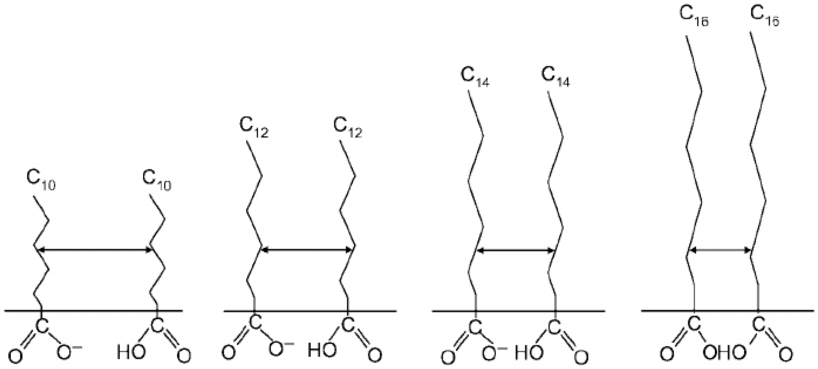

Figure 5.3. Illustration of the effect of hydrocarbon chain length upon packing distance for polar amphiphiles. Figure adapted from reference [76].

5.2 Methods

5.2.1 Goals and approach

In collaboration with Drs. Bor-Ron Chen and Robert Kennedy, I sought to study the effect that surfactants have on the shape, size, and surface termination of STO nanoparticles. The methodology relied upon using simple molecules with the same functional group, for which thermodynamic data is available with regards to the formation of liquid crystals in microemulsions. The intent was to target the lamellar phase to obtain the SrO surface termination by an alternative means to using oleic acid as the surfactant, to enable scaling of the synthesis and to ease removal of the surfactant from the surfaces of the resulting nanocrystals. Oleic acid has a carbon chain length of 18, but is unsaturated due to the double bond in the middle of the hydrocarbon tail. Given that one of the primary difficulties with the use of oleic acid is the removal of the surfactant post-synthesis, we began our study with the lowest molecular weight surfactant with a carboxylic acid functional group that is known to form liquid crystal phases. Caprylic acid (IUPAC name octanoic acid) is the surfactant molecule which met our requirements.

We also investigated other intermediate alkyl length carboxylates which are not known to form microemulsions: propanoic, butanoic, pentanoic, hexanoic, and heptanoic acid (all IUPAC names). These were all of the form $CH_3(CH_2)_{n-2}COOH$, and, taken together with acetic acid, span the range $3 \le n \le 8$.

5.2.2 Experimental

A two-pronged approach was adopted to study the effect of these different surfactants. Each of the carboxylic acids above at a fixed ratio of water, surfactant, and alcohol were tested to determine if the surface morphology was significantly altered. In parallel, several different synthesis conditions were tested using caprylic acid with varied ratios of water, surfactant, and alcohol. We also attempted the oleic acid synthesis. Previous results using oleic acid resulted in sharply faceted nanoparticles with an average size of approximately 20 nm (see references [79] and [71]), while use of acetic acid resulted in faceted nanoparticles with an average size of 60 nm (see reference [80]). The details of each of these syntheses follow.

5.2.2.1 Varied Carboxylate Synthesis

Solution A was prepared by dissolving 9 mmol of $Sr(OH)_2 \cdot 8\,H_2O$ into 50 mL of 1 M of the n-carboxylate acid, for $4 \le n \le 8$. Solution B was prepared by dissolving an equimolar amount titanium tetrachloride ($TiCl_4$) into 20 mL of ethanol. Solution A was added to solution B, and 5 g NaOH pellets were added to the resulting solution while stirring vigorously. After stirring for 15–30 min, the solution was transferred to a Teflon-lined autoclave and treated hydrothermally at 240 °C for 48 h. Samples were removed from the autoclave, washed by repeated centrifugation in water to neutral pH (7), and dried overnight in air at 80 °C. TEM samples were prepared by sonicating in ethanol and drop-casting onto lacey carbon grids.

5.2.2.2 Targeted Caprylic Acid Synthesis

Solution A was prepared by dissolving 10 mmol strontium acetate ($Sr(Ac)_2$) into varied concentrations of caprylic acid solution. Solution B was prepared by adding an equimolar amount of titanium tetrabutoxide ($Ti(OBu)_4$) was added to varied amounts of caprylic acid, water, and butanol. The molar ratios of [caprylic acid]:[butanol]:[water] was varied to target several microemulsion phases (lamellar, micellar, and hexagonal). Figure 5.4 shows all synthesis conditions attempted with relation to the sodium caprylate/butanol/water ternary phase diagram.

Otherwise, the samples were all prepared in the same manner as described above.

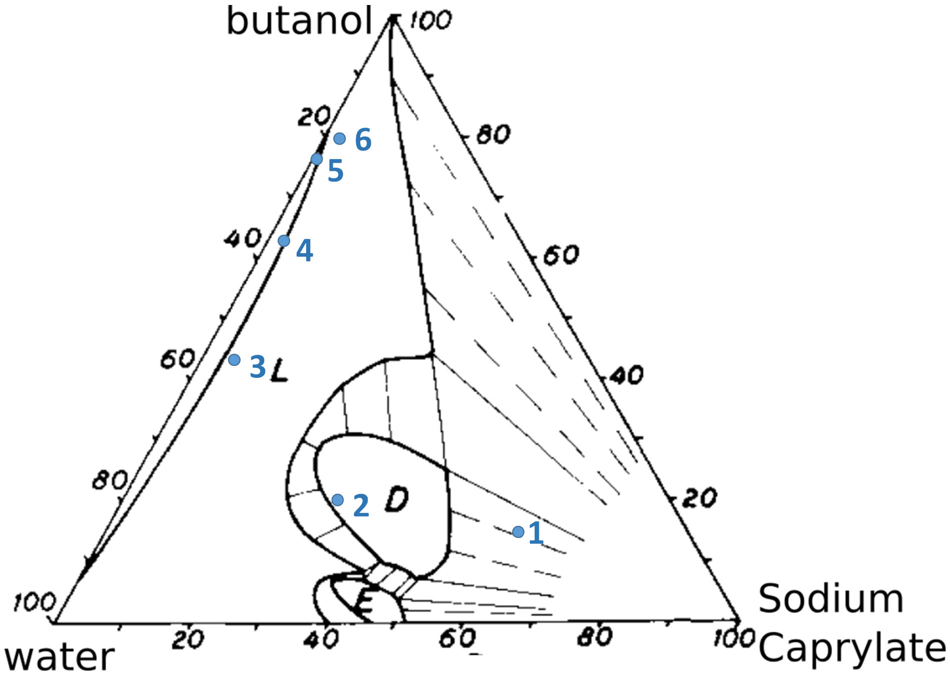

Figure 5.4. Phase diagram of the sodium caprylate/butanol/water ternary system. Note that points 1–6 marked on the diagram correspond to synthesis conditions attempted for the purpose of this study. Figure adapted from reference [81].

5.2.3 Oleic Acid Synthesis

For this synthesis, we followed a modified method based upon work by Hu *et al.*[79] Solution A was prepared by dissolving 1 mmol $Sr(Ac)_2$ in 15 mL of deionized water. Solution B was prepared by dissolving an equimolar amount $Ti(OBu)_4$ in 25 mL ethanol and 5 mL of oleic acid. Solution C was prepared by mixing 2.5 mL of 10 M NaOH to 20 mL ethanol. An additional 0.4 g of sodium oleate was added to the solution while stirring.

Solutions A and B were added to solution C and while stirring. The resulting mixture was transferred to a 125 mL Teflon-lined autoclave and treated hydrothermally for 10 h at 180 °C.

5.3 Results

5.3.1 Varied Carboxylic Acids

The synthesis of using the n-carboxylic acids ($4 \leq \leq 8$) resulted in particles similar to previous results obtained using acetic acid. Particles were cube-like, with predominantly {001} faceting and rounded corners. The particle size distributions were also similar to the acetic acid case, with an average particle size between 60 and 80 nm. See Figures 5.5–5.6 for examples of representative bright-field TEM images.

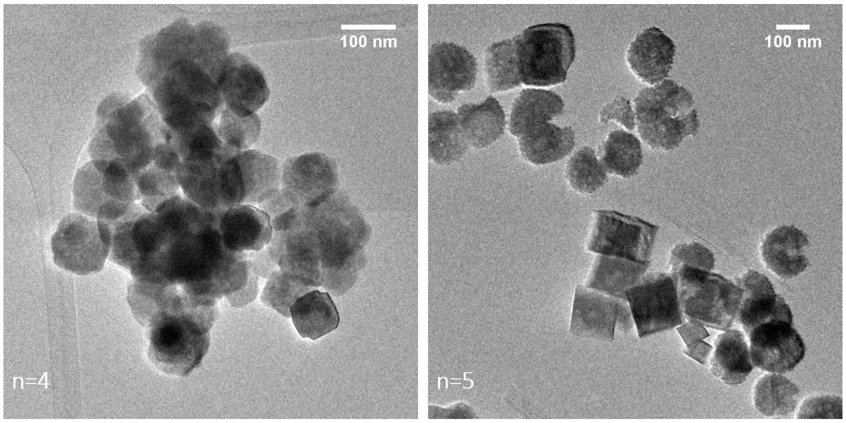

Figure 5.5. Bright-field TEM images of STO nanocuboids resulting from the use of butanoic and pentanoic acid in place of acetic acid.

Direct substitution of caprylic acid for acetic acid resulted in particles with irregular shapes and faceting. This is attributed to poor mixing between the caprylic acid and the solvents, water and ethanol as we did not change the stirring times for the different surfactants. Inhomogeneity in the distribution of the strontium and titanium and titanium aqueous species will lead to significant variation in the chemical potential, which leads

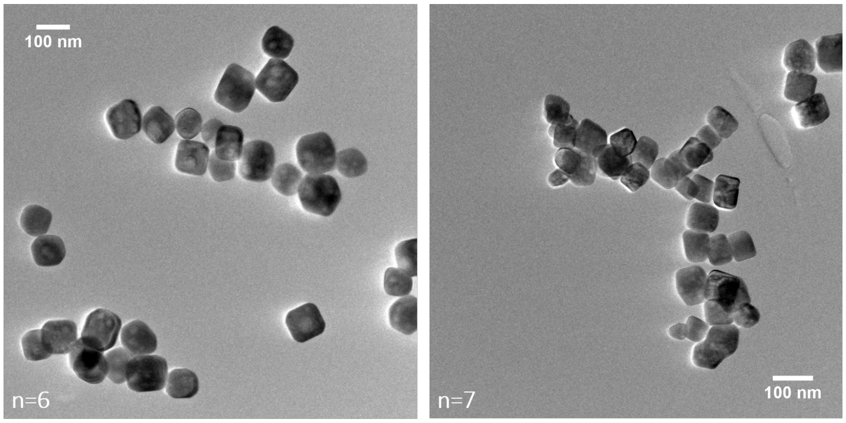

Figure 5.6. Bright-field TEM images of STO nanocuboids resulting from the use of hexanoic and heptanoic acid in place of acetic acid.

to rough surfaces compared to the more homogeneous case. Figure 5.7, a secondary electron image, shows particles which illustrate this effect.*

Substituting $Sr(Ac)_2$ for $Sr(OH)_2 \cdot 8\,H_2O$ and butanol for ethanol in equimolar ratios, we obtained more regular particle morphology. The particles had an average size of approximately 140 nm, with some particles as large as 300 nm. This synthesis corresponds to point 5 as marked on the phase diagram in Figure 5.4. A representative image of particles from keeping the volumes of solvents the same as the acetic acid synthesis while using $Sr(Ac)_2$ and $Ti(OBu)_4$ as precursors appears below section 5.3.2.

---

*Note that the process of TEM sample preparation will lead to mixing of the particles in solution, which is a probable explanation for why these two different particle types appear in the same region of the TEM grid.

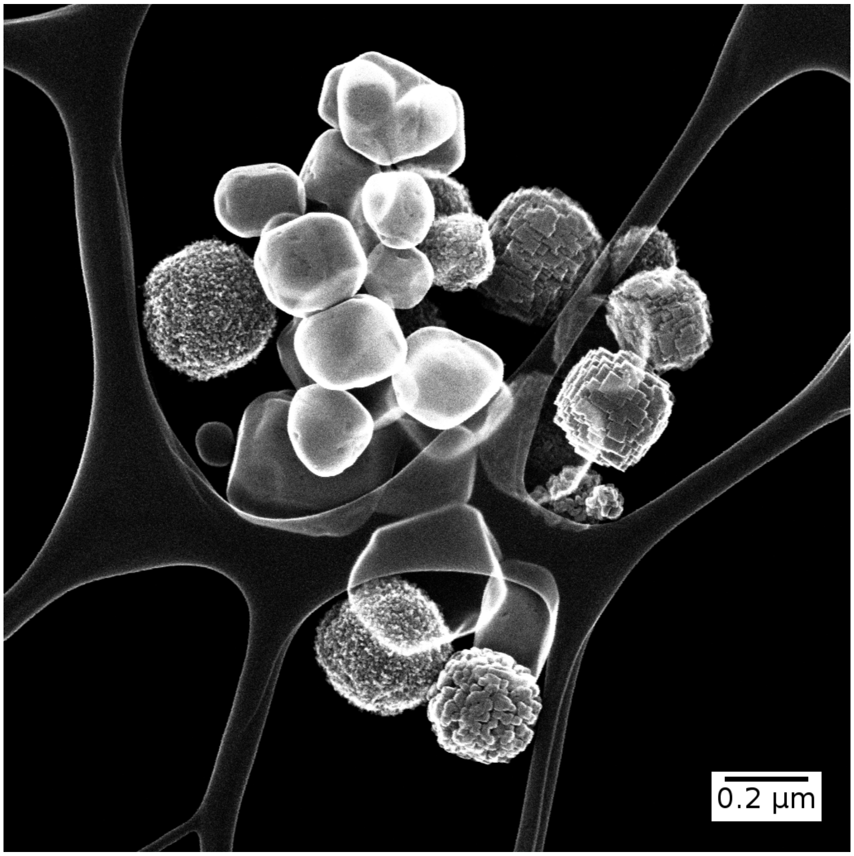

Figure 5.7. Secondary electron image showing disparate particle morphology obtained using caprylic acid in place of acetic acid when following the method developed by Federico *et al.* from reference [80]. Note that there are particles with terraces as well as smooth surfaces.

5.3.2 Caprylic Acid Phase Diagram

Changing the ratios of water, butanol, and caprylic acid led to significant changes in both the particle size and morphology.

The average particle size (edge-to-edge distance) for points 5 and 2 on the phase diagram in Figure 5.4 changed from 140 nm to 20 nm, respectively. These for particles in Figures 5.8 and 5.9. Additionally, the particles appeared to be rod-like fingers without distinct faceting that could be identified.

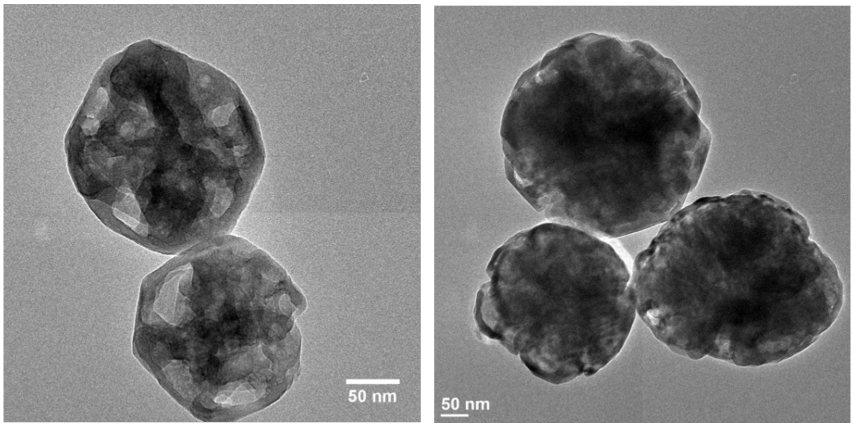

Figure 5.8. Results of synthesis using caprylic acid, butanol, and water with molar fractions of 0.007, 0.435, and 0.558, respectively. These correspond to point 5 in Figure 5.4.

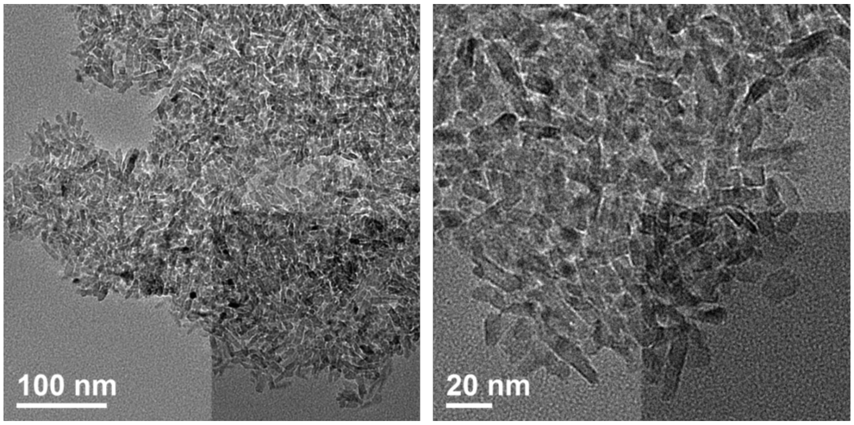

Figure 5.9. Results of synthesis using caprylic acid, butanol, and water with molar fractions of 0.07, 0.07, and 0.86, respectively. These correspond to point 2 in Figure 5.4.

Images from point 5 were investigated in greater detail using HREM; see Chapter 7 for more details.

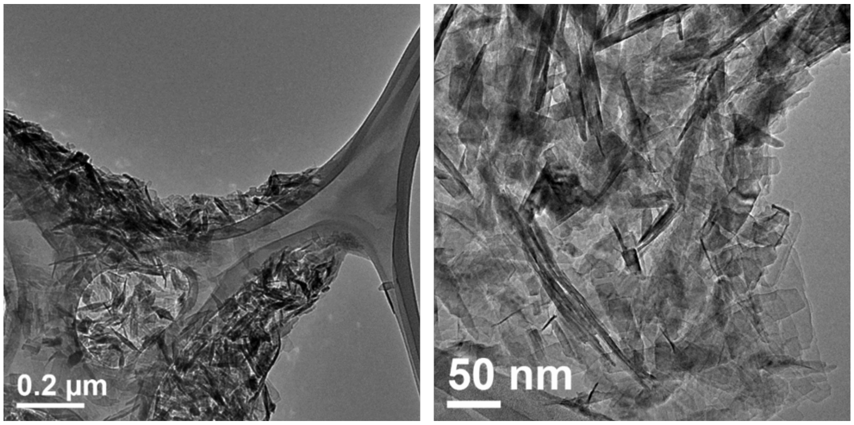

Figure 5.10. Results of synthesis using caprylic acid, butanol, and water with molar fractions of 0.01, 0.13, and 0.86, respectively. These correspond to point 3 in Figure 5.4.

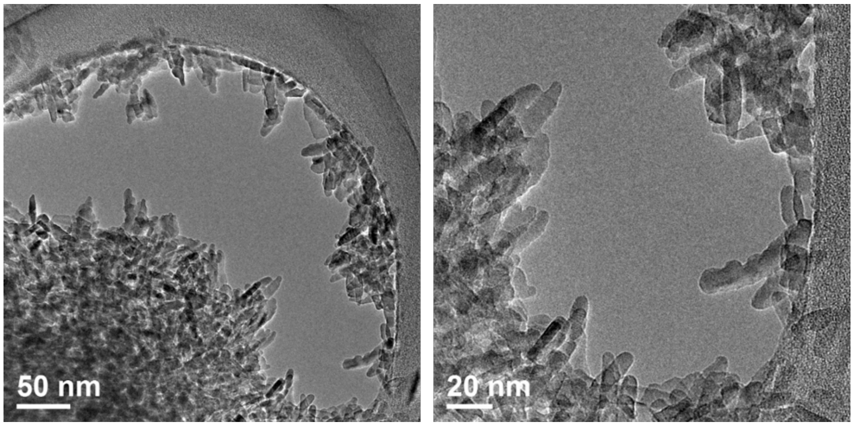

Figure 5.11. Results of synthesis using caprylic acid, butanol, and water with molar fractions of 0.21, 0.11, and 0.68, respectively. These correspond to point 1 in Figure 5.4.

5.3.3 Oleic acid synthesis

Particles which resulted from the oleic acid synthesis were similar to the cases described in the previous section. Representative images appear below in Figure 5.12.

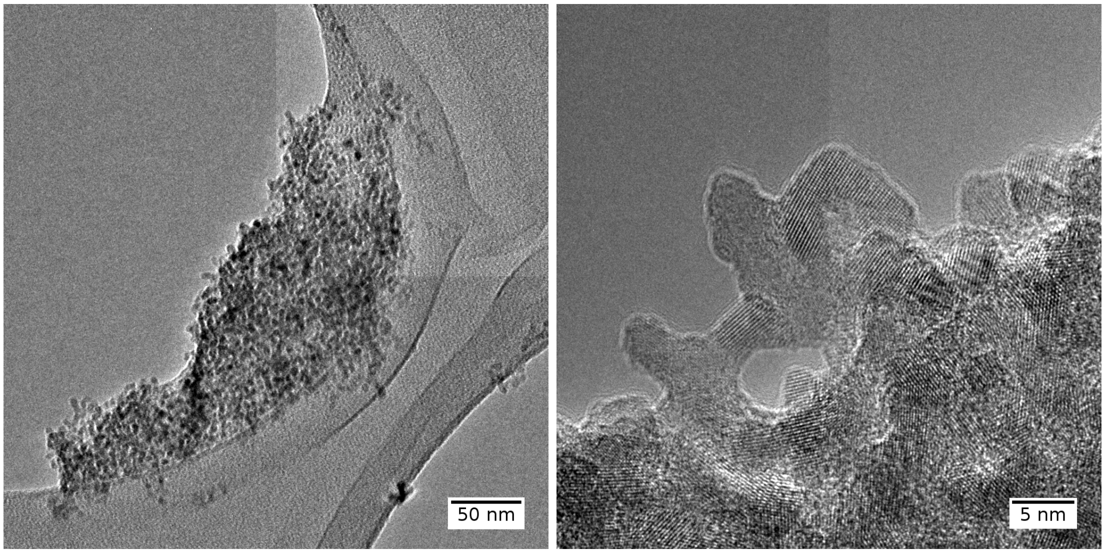

Figure 5.12. TEM (left) and HREM (right) images of STO particles resulting from oleic acid synthesis. Note that particles are on average less than 20 nm in size and lack of regular faceting. These results are similar to those in Figure 5.9. Variation in contrast is because of unequal gain calibration for the four quadrants of the CCD detector.

5.4 Discussion

The results of this study indicate that increasing the length of the surfactant hydrophobic end group has minimal effect upon the nanoparticle morphology when simply substituted for acetic acid. However, for the caprylic acid case, the introduction of the multiple liquid crystal phases does cause significant changes in the resulting nanoparticles. Point 2 on the phase diagram corresponds to a lamellar microemulsion, while 1 is a phase-separated region. These resulted in much smaller nanoparticles than the other points along the phase diagram. These results, in particular, are in agreement with reports in the literature which use long-chain fatty acids such as oleic acid.[71,82–84] Thus, caprylic acid may be sufficiently non-polar[76] to alter the surface chemistry in a manner similar to the method developed by Hu *et al.*[79]

However, we were unable to obtain shape-control through this method. For applications, this is a desirable outcome, particularly for fundamental studies of catalysis in which the support can play a significant role.

Our own attempts to obtain well-faceted nanocrystals using the oleic acid synthesis route led to similar results with regards to particle shapes and size distributions as reported in Section 5.3 above. There are a few possible explanations for this. The first is that the phase diagram is not accurate for our synthesis conditions, as it is reported for ambient conditions, whereas the nanoparticle growth occurs at elevated temperature and pressure. For the oleic acid case, the reported ratios of oleic acid:alcohol:water, when projected onto the phase diagram reported by Jing *et al.*—the true phase diagram with ethanol is not reported—will yield the points labeled 1 and 2 (see Figure 5.15) for the synthesis conditions previously reported (see reference [79]) and the conditions listed in section 5.3.3, respectively.

These two points, which target the lamellar phase, are clearly outside the stability regime for this phase. While the use of ethanol will change these stability regimes, one should be able to compare with similar systems to predict how the phase diagram will be altered. Comparing this case with the caprylic acid/alcohol/water system, one can see that the use of ethanol significantly suppresses the stability of the lamellar phase (see Region D in Figure 5.14).

This effect should be amplified in the case of oleic acid, because oleic is considerably more non-polar than caprylic acid due to the longer hydrophobic hydrocarbon tail. Consequently, ethanol, which is more polar than butanol, will be considerably less miscible

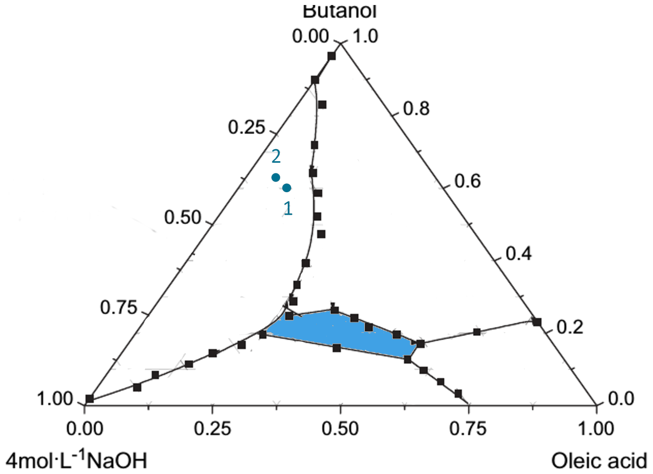

Figure 5.13. Phase diagram for the oleic acid/butanol/sodium hydroxide system, as shown in Figure 5.15. Point 1 corresponds to the synthesis conditions reported in reference [79]. Point 2 corresponds to the synthesis conditions listed in section 5.3.3. Note that the targeted region is the lamellar liquid crystal, which is highlighted in blue. Also note that substituting ethanol for butanol will alter the phase diagram.

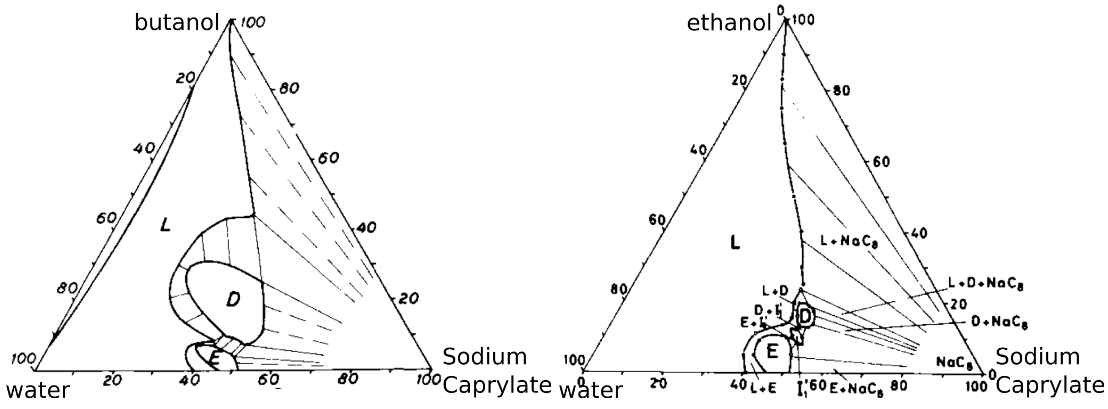

Figure 5.14. Stability equilibria for water/sodium caprylate/alcohol systems at 20 °C and atmospheric pressure. Note the reduction in area of the Region D, the lamellar phase, for ethanol compared with butanol. Figure adapted from reference [81].

with oleic acid than caprylic acid. This will likely lead to an even more dramatic reduction in the stability regime for the lamellar phase in this case.

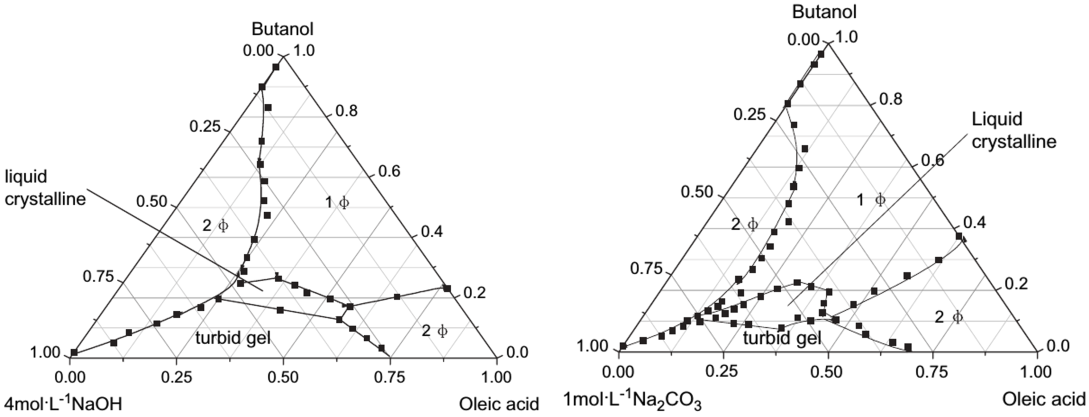

Figure 5.15. Stability equilibria for oleic acid/butanol/NaOH system at standard conditions. Note the shift of the stability region for the lamellar liquid crystal phase, labelled as liquid crystalline in the phase diagrams, upon changing the mineralizer from NaOH to $NaCO_3$. Figure adapted from reference [85].

As a result, the conditions required to obtain the lamellar phase are likely confined to an extremely narrow range of relative ratios of the fatty acid, alcohol, and water in the ethanol case. This serves as an explanation for the difficulty in reproducing the results—namely well-faceted particles with a SrO-terminated surface—using this synthetic procedure.

5.5 Conclusion

In this chapter, we discussed the synthesis of STO nanocrystals using various carboxylic acids. TEM was used as the primary characterization tool to determine that the resulting particles were either nanocuboids similar to previous results using acetic acid or small particles with ill-defined faceting. Finally, I related these conditions to literature thermodynamic references for the liquid microemulsions to provide a rationale for the observed particle morphologies. Possible future directions would be to perform a more careful study of the microemulsion stability under the hydrothermal growth conditions via in-situ study, and attempts to use butanol or other long-chain alcohols instead of ethanol.

CHAPTER 6

Synthesis and Characterization of Barium Titanate Nanocuboids

6.1 Introduction

This work is motivated, in part, by previous observations of interesting materials phenomena in BTO. For example, it is known that the stability of the tetragonal phase of BTO depends significantly upon size.[86–89] The study of well-faceted nanocrystals of BTO fits into the larger picture of extending model material systems from macroscopic single crystals to the nanoscale. Through shape-controlled, and, ideally, size-controlled nanoparticle synthesis, quasi-ideal model catalytic systems can be successfully designed, studied, and engineered. Determining synthetic routes for this is an important part of this process, to enable the future study of reaction kinetics and selectivity for catalyst-support systems.

Hydrothermal preparation is a time-proven method to obtain crystalline BTO.[36,37,90–99] The nanoparticle synthesis literature reports several methods to control size and shape of highly monodisperse particles, mostly relying upon surfactants of various kinds to accomplish this outcome.[97–99]

For applications which require subsequent deposition of active materials, such as catalysis and some electronic devices, it is important to be able to effectively remove the surfactants from the nanoparticle surfaces after synthesis. Thus, for this study, the use of high molecular weight oligomers was avoided to ensure that they could be removed using common solvents, such as water and ethanol. With these ideas in mind, a synthetic approach to obtain crystalline BTO nanocuboids is described below where relatively low molecular weight surfactants are combined with hydrothermal synthesis to obtain shape and size–controlled nanocrystals.

6.2 Synthesis

The method developed by Dr. Federico Rabuffetti for the synthesis of STO, published in reference [80], was used as a starting point, and modified as as described below. $Ba(OH)_2 \cdot 8\,H_2O$ was substituted for $Sr(OH)_2 \cdot 8\,H_2O$, and the concentrations of both the Ba and Ti precursors were doubled. Additionally, the temperature and runtime of the hydrothermal treatment was varied in order to optimize the particle size distribution. With these changes, the details of the synthesis are as follows.

Solution A was prepared by dissolving 9–18 mmol of $Ba(OH)_2 \cdot 8\,H_2O$ in 50 mL of 1 M acetic acid solution. Solution B was prepared by dissolving an equimolar amount of $TiCl_4$ in 20 mL ethanol. Solution B was added to Solution A and 5 g solid NaOH pellets were added to the resulting solution while stirring. Upon the addition of NaOH, the solution become viscous and required vigorous stirring to maintain a uniform mixture. The solution was stirred continuously for an additional 15–30 min, and subsequently transferred to a Teflon-lined autoclave (Parr) for hydrothermal treatment. Several batches were run at different temperatures and runtimes: at 240 °C and 180 °C from 12 h to 48 h. After hydrothermal treatment, the resulting white powder was centrifuged with deionized water repeatedly until a neutral pH (7) was attained, as measured by pH strips. The powder was then dried overnight (8–12 h) at 80 °C.

6.3 Characterization

Several characterization techniques were employed to investigate the products produced by this synthesis. XRD provided a macroscopic analysis of the phase of crystalline products. For X-ray data, the source was a simple Cu Kα tube source operating at 40 kV and 20 mA. XPS measured the chemical state and offered an estimate of the relative amounts of the primary product and other secondary phases present in the sample. TEM and TED enabled identification of particle morphology and size distributions, as well as information about localized crystal structure.

6.4 Results

A first attempt at producing BTO by directly substituting $Ba(OH)_2 \cdot 8\,H_2O$ for $Sr(OH)_2 \cdot 8\,H_2O$ in the method developed by Rabuffetti *et al.* while keeping all other parameters identical successfully yielded single crystal BTO nanoparticles. However, there were significant differences in the nanoparticle morphology. TEM imaging (see section 6.4.3 below) showed significant polydispersity with respect to both size and shape, with irregularly shaped particles ranging in size from tens of nanometers to one micrometer. To improve this, the reaction conditions were altered. The enthalpy of formation for BTO[100] is approximately 17 kJ/mol more exothermic than STO,[101] so the reaction temperature was reduced to 180 °C. Additionally, the solubility of the Ba precusor in water is lower than the Sr precursor. Consulting thermodynamic predictions by Lencka and Riman (see phase diagram pp 162–163 in reference [102]), the high-yield region for BTO requires a greater molality of metal precursors in solution than STO. Consequently, the concentrations of both the Ba and Ti precursors were doubled to 18 mmol while holding the other parameters the same.

6.4.1 X-ray Measurements

Powder XRD confirmed that crystalline BTO resulted from the synthesis. The diffraction pattern shown in Figure 6.1 is indexed with cubic peak positions[*] that for BTO (space group Pm$\bar{3}$m), with lattice parameter of 4 Å. Note that there is also evidence of a secondary phase. Although difficult to see against the strong reflections from BTO, fine scans (see Figure 6.1a and 6.1b) show evidence of impurity crystalline peaks.

Further analysis of the secondary phase showed it best matches the witherite structure, which is an orthorhombic phase of $BaCO_3$ (BCO) (a = 5.3126 Å, b = 8.8958 Å, c = 6.4284 Å, $\alpha = \beta = \gamma = 90°$), which is the stable phase at standard conditions. Unfortunately, the quality of the data was not sufficient to carry out quantitative analysis, such as Rietveld refinement, to determine the amount of secondary phase present using the X-ray data. The use of a monochromator and/or a brighter source, such as a synchrotron, would enable a more accurate determination from XRD.

---

[*] Note that in this case there is still the possibility of tetragonal peak splitting. The broadening effects from the instrument and particle size cannot be deconvolved from the data shown Figure 6.1. Additional data with higher resolution would be needed to confirm this.

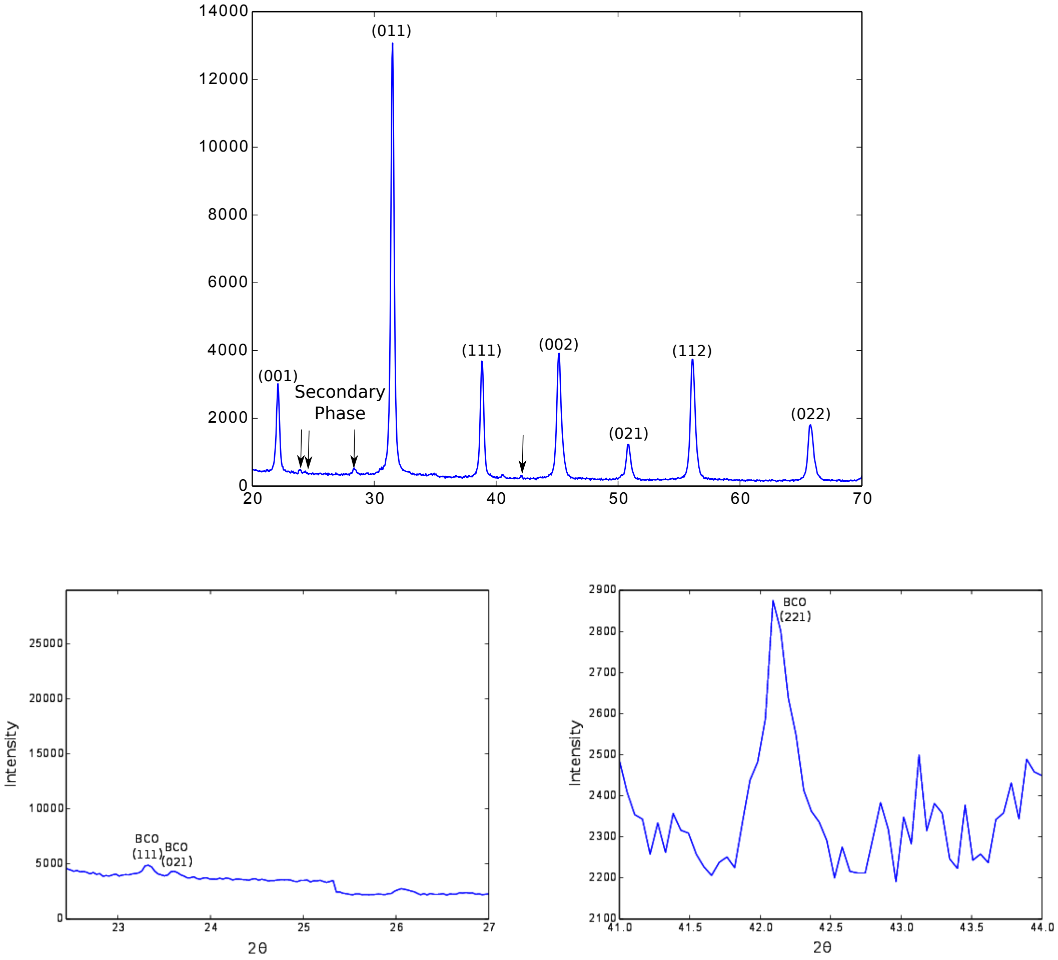

(a) Narrow range θ-2θ scan of BCO diffraction conditions.

(b) Narrow range θ-2θ scan of BCO diffraction conditions.

Figure 6.1. Powder XRD of products of BTO for run at 240 °C for 24 h. Note the presence of weak reflections resulting from the presence of a secondary phase identified as BCO.

6.4.2 X-ray Photoelectron Spectroscopy

To gain further insight, additional analysis of the BCO secondary phase was carried out using XPS. The summary of that analysis follows.

Four different synthesis runs with different parameters were characterized in the same XPS chamber to provide comparable results. All spectra were acquired using the same dwell time for each energy step to obtain comparable signal counts, although there was some variation in sample loading.

The XPS spectra acquired were processed using the Avantage software from Thermo Scientific, and each was charge shifted using the adventitious C 1s peak (284.8 eV) as the reference. Peak fitting was performed using the same software with the built-in peak-fitting subroutine. All spectra were fitted using a Gaussian-Lorentzian product hybrid with the Powell algorithm and a convergence criterion of 0.001. This performs a least-squares fit which attempts to minimize the residual for the difference between the experimental peak and the fitted peak.

The C 1s and O 1s peaks were fitted using two singlets, while the Ba 3d and Ti 2p peaks were fitted with a single doublet in order to constrain the separation of the fit.

To get a rough estimate for the quantity of secondary phase produced, the XPS peaks were integrated and compared. The goal here is to compare the quantity of BCO versus BTO for each sample by taking the integrated area of the Ba 3d, Ti 2p, C 1s, and O 1s peaks. These areas were corrected with sensitivity factors for each element to determine the atomic ratios of each. The results of this analysis appear in Table 6.1.

Table 6.1. Estimated atomic percentages of key binding energies for BTO and BCO. The C 1s peak at 289 eV was fitted based upon reference values for carbonate phases (see p 41 reference [103] as well as reference [104]). Note that C contamination from the atmosphere and hydrocarbons is unavoidable and likely also present.

Experiment	Ba 3d (at %)	Ti 2p (at %)	C 1s (at %)	O 1s (at %)
A 24 h at 240 °C	21.2	19.5	2.8	56.5
B 12 h at 180 °C	15.1	19.9	3.9	61.7
C 24 h at 180 °C	12.9	21.4	5.9	60.0
D 48 h at 180 °C	18.5	18.7	2.0	60.8

From the table, the BCO phase varies between 2 and 6 at % (approximately 1.7 and 5 wt %, respectively).

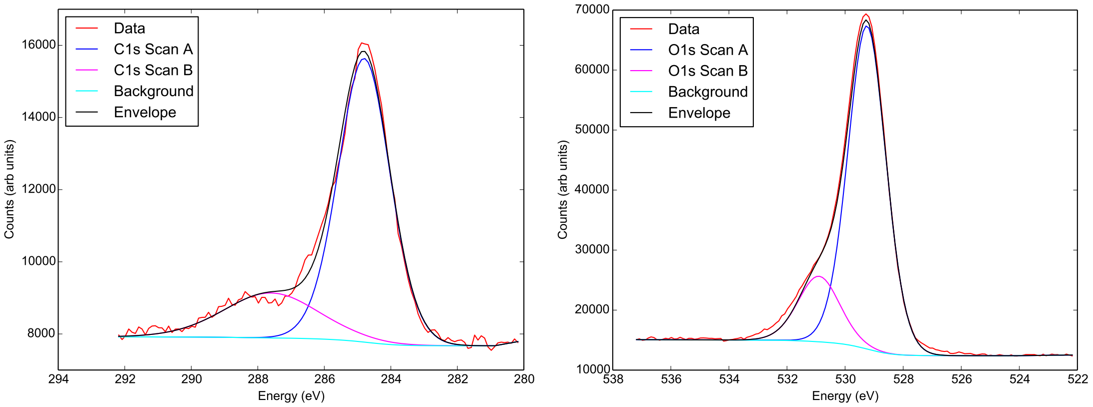

(a) XPS scan of C 1s states.

(b) XPS scan of O 1s states.

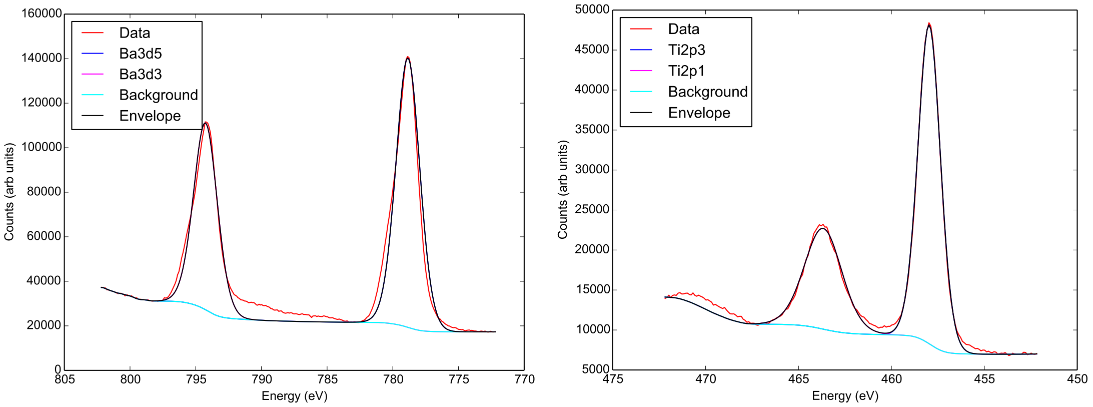

(c) XPS scan of Ba 3d states.

(d) XPS scan of Ti 2p states.

Figure 6.2. XPS spectra of products of hydrothermal reaction at 240 °C for 24 h.

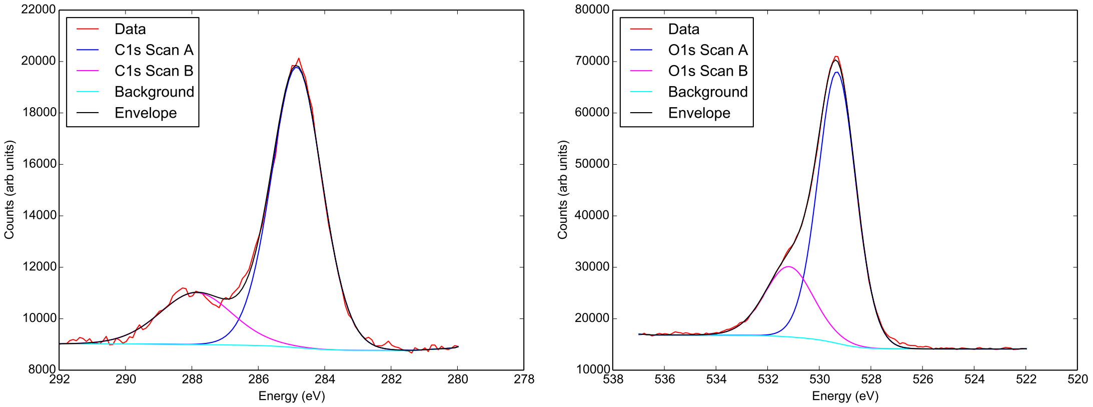

(a) XPS scan of C 1s states.

(b) XPS scan of O 1s states.

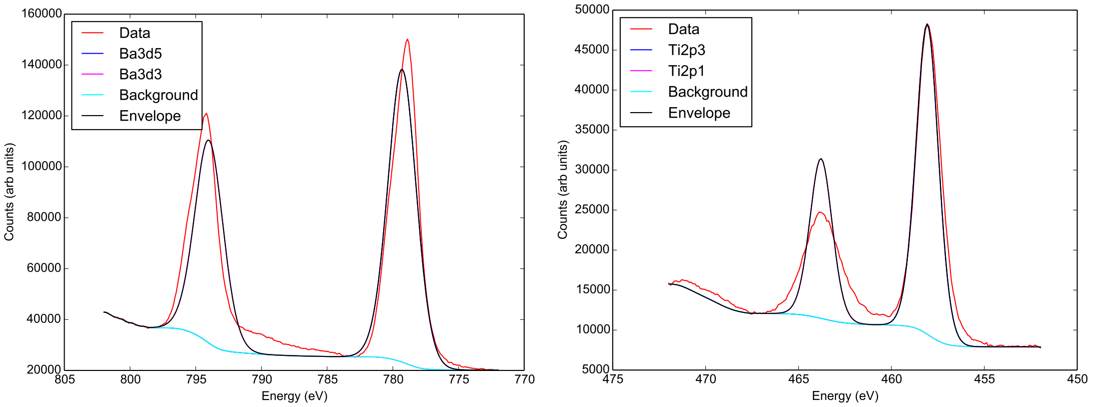

(c) XPS scan of Ba 3d states.

(d) XPS scan of Ti 2p states.

Figure 6.3. XPS spectra of products of hydrothermal reaction at 180 °C for 12 h.

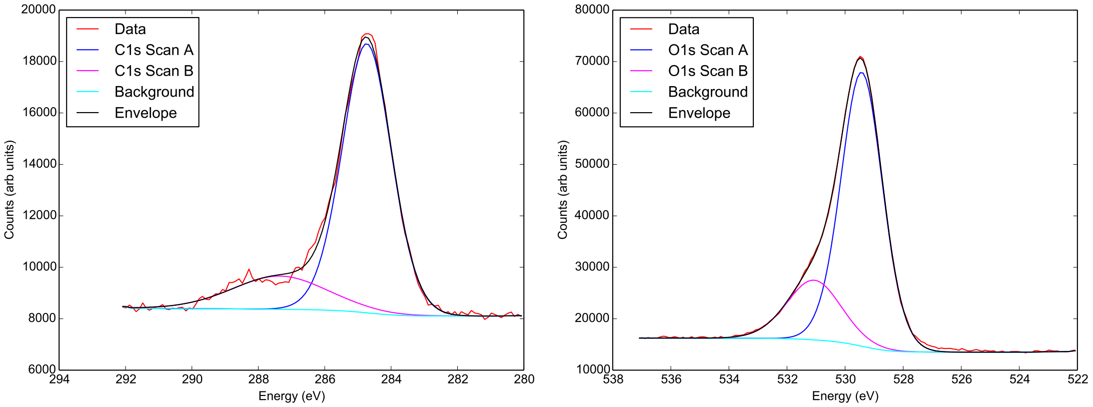

(a) XPS scan of C 1s states.

(b) XPS scan of O 1s states.

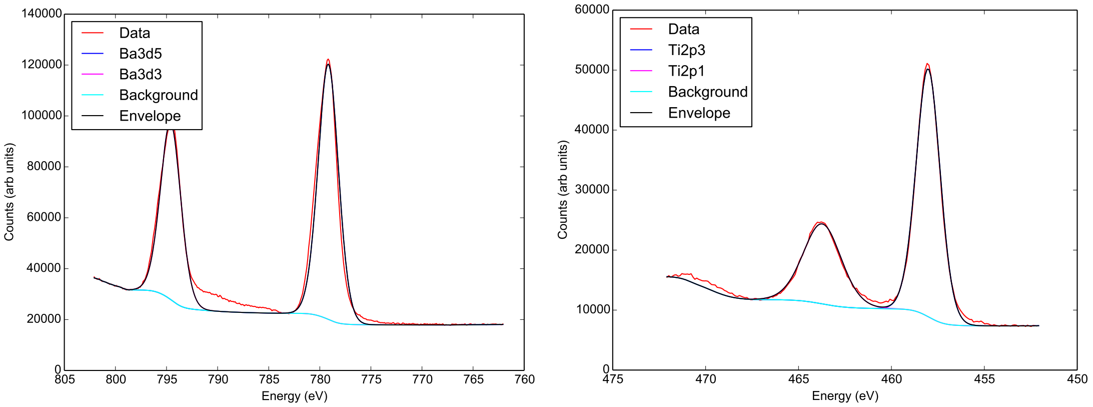

(c) XPS scan of Ba 3d states.

(d) XPS scan of Ti 2p states.

Figure 6.4. XPS spectra of products of hydrothermal reaction at 180 °C for 24 h.

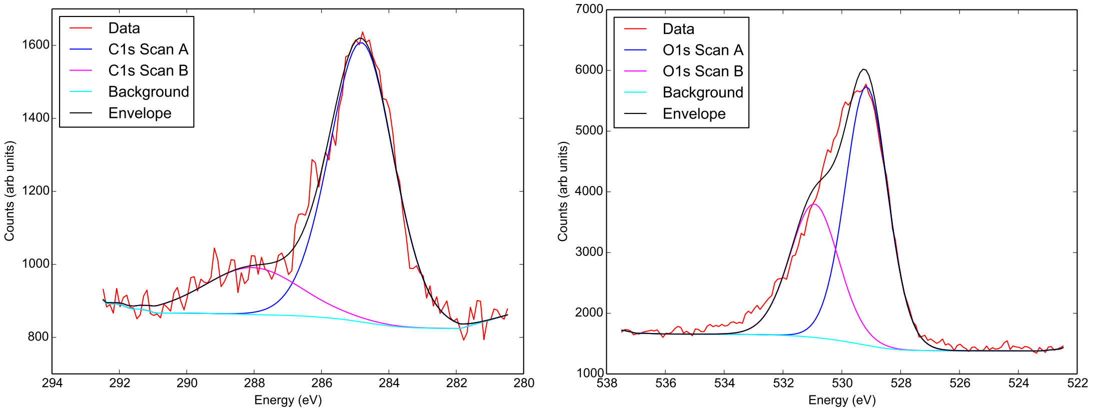

(a) XPS scan of C 1s states.

(b) XPS scan of O 1s states.

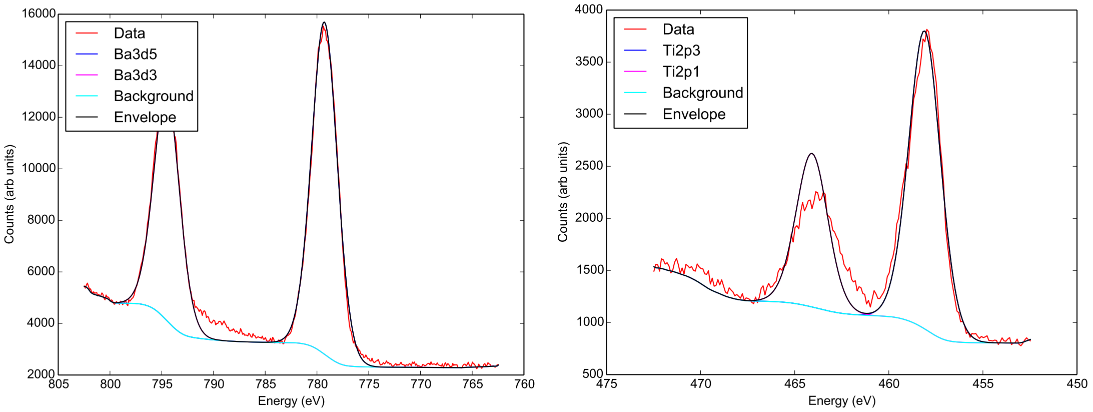

(c) XPS scan of Ba 3d states.

(d) XPS scan of Ti 2p states.

Figure 6.5. XPS spectra of products of hydrothermal reaction at 180 °C for 48 h.

6.4.3 Electron Microscopy

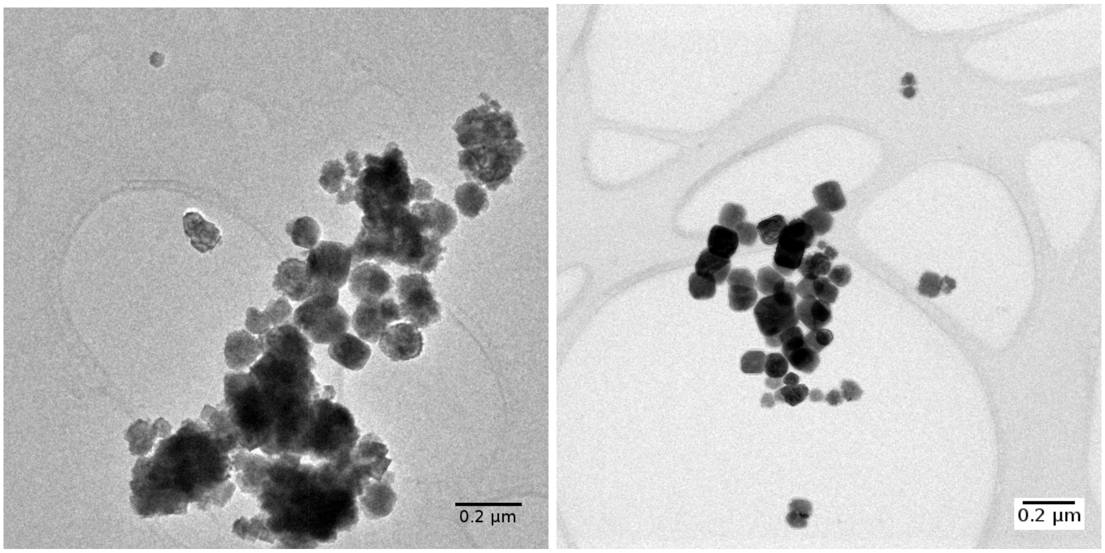

(a) Bright-field TEM image of synthesis run at 240 °C for 24 h.

(b) Bright-field TEM image of synthesis run at 180 °C for 12 h.

Figure 6.6. Bright field TEM image showing polydispersity of BTO nanoparticles resulting from direct substitution of $Ba(OH)_2 \cdot 8\,H_2O$. The effect of lowering reaction temperature on the nanoparticle morphology can be see by comparing (a) to (b).

The morphology of the BTO nanocrystals was studied with TEM imaging. Synthesis at 240 °C produced polydisperse crystals with a range of shapes and sizes, as shown in Figure 6.6a. The effect of lowering the reaction temperature to 180 °C can be seen in Figure 6.6b. At this temperature, the nanocrystals are more monodisperse, with shapes that are similar to STO nanocuboids made using the same technique. The particle size distribution is shown in Figure 6.7 for the 180 °C 48 h synthesis, with a mean particle size of 80 nm.

The sample surface was found to be TiO_2-rich, using HREM; more details can be found in Chapter 7.

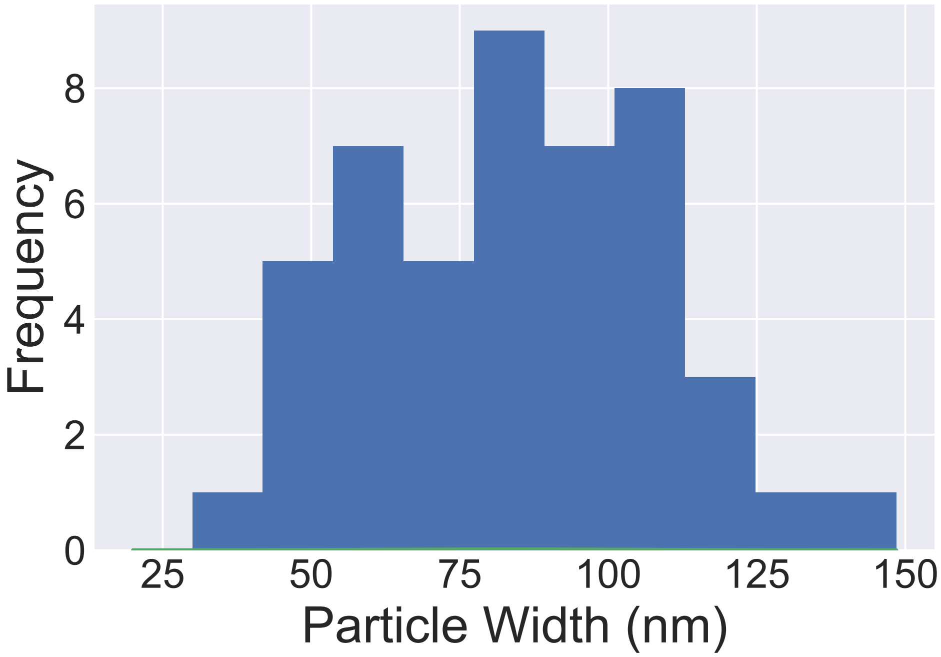

Figure 6.7. Size distribution of BTO nanoparticles produced using modified Federico synthesis.

6.5 Discussion

An unexpected by-product of the experiment was the occurrence of nanowires (see Figure 6.8) with high aspect ratios. Figure 6.8b shows a selected area diffraction pattern from the resulting BCO nanorods.

The resulting diffraction pattern is a ring pattern because multiple crystals with different orientations all contribute to the total scattering. The pattern is indexed with positions of the witherite phase of BCO. Since this is an orthorhombic structure, the interplanar spacings can be determined using the equation:

$$\frac{1}{d_{hkl}^2} = \frac{h^2}{a^2} + \frac{k^2}{b^2} + \frac{l^2}{c^2}, \tag{6.1}$$

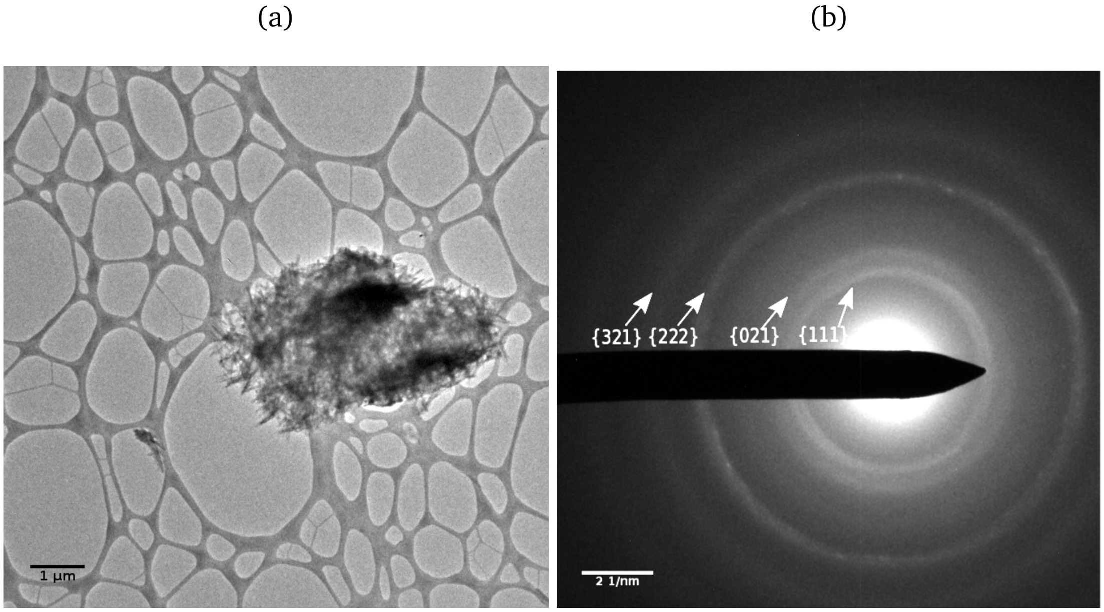

Figure 6.8. (a) Bright field TEM image of nanorods found during sample imaging. (b) Selected-area TED from nanowires, indexed with peak positions of the witherite structure of BCO.

where h, k, l are Miller indices, a, b, and c are lattice constants, and d_{hkl} is the d-spacing of a particular atomic plane. The result of applying this analysis, a comparison between kinematical positions and the measured electron diffraction d-spacings, appears in Table 6.2.

Table 6.2. Comparison of experimental peak positions and kinematical positions for ring TED pattern of BCO nanowires, showing excellent agreement between the model and experiment.

Ratios	d_{111}	:	d_{021}	:	d_{222}	:	d_{321}
Kinematical Peak Locations	1	:	0.983	:	0.5	:	0.428
Experiment (TEM)	1	:	0.964	:	0.496	:	0.424

From the literature[105] it is known that BCO will form as a by-product of chemical synthesis of BTO if CO_2 is present in the atmosphere. To eliminate this secondary phase during the synthesis, one could dissolve and mix the Ba precursor in an inert atmosphere. Alternatively, because the yield of BTO is so high (~ 98 %), the BCO could be removed post-synthesis using a dilute acid.[98]

Regarding the BCO particle morphology, there are several reports of high-aspect ratio nanorods being produced as a result of using dicoctyl sodium sulfosuccinate microemulsions.[97] By comparison, the synthesis reaction presented herein used a lower molecular-weight surfactant—acetic acid (60 g/mol) instead of dicoctyl sodium sulfosuccinate (444 g/mol)—but still contained carboxylic (-COOH) functional groups. Further study would be required to determine how the surfactants influence the growth and final shape of the BCO nanocrystals.

6.6 Conclusion

This chapter described the successful synthesis of crystalline BTO, and presented the characterization used to determine the morphology and quantity of BCO secondary phase. The BTO was found to match the cubic phase from powder XRD, and the average particle size was found to be 80 nm from TEM imaging. This provides a robust, scalable method to obtain high quality crystalline and shape-controlled BTO particles, while benefiting from using a surfactant that is easy to remove for use in applications.

CHAPTER 7

All Roads Lead to TiO_2: {001} Surfaces of Barium Titanate and Strontium Titanate Nanocrystals

7.1 Introduction

Nanoparticles with well-controlled shapes and sizes are highly desirable, and are often sought as the end goal of nanoparticle synthesis because regular shape and size can be exploited for applications. At the nanoscale, materials properties can, and often do, deviate from those of their bulk counterparts. STO and BTO are two materials of importance with a large supporting literature at both the macroscale and the nanoscale. The surface of STO has been particularly well-studied, with many reports in the literature.[106–113] The ferroelectric properties of BTO have made it a material of interest for researchers.[114,115]

While the overall shape of many oxide nanoparticles as a function of hydrothermal synthesis conditions is now established, the surface structure is known in only a few rare cases. For many applications, the surfaces are more important than the bulk—for instance when oxide nanoparticles are used as active catalyts, or supports in heterogeneous catalysis. A few examples from recent literature show that properties such as electrical conductivity[116] and photocatalytic activity[117] are facet-dependent, and ferroelectric properties have the potential to affect catalysis *in operando*.[118] While it is established that the surface of STO at the macroscale can be very complex,[119–121] whether this carries over to nanoparticles is unknown.

In this chapter, we will discuss HREM analysis to resolve surfaces of BTO and STO nanoparticles. The {001} surfaces all have experimental contrast that matches the same surface reconstruction reported in work on single crystals (see Figure 7.1).

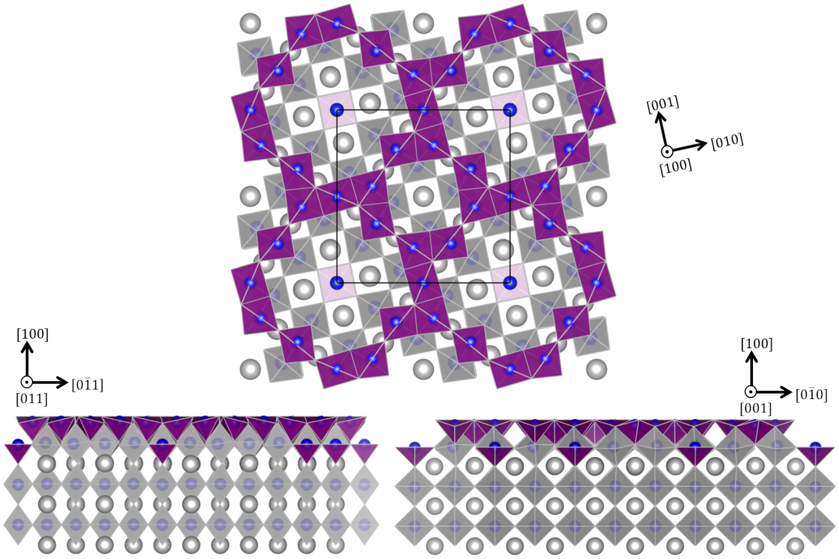

Figure 7.1. Polyhedral model of a 2 × 2 supercell of the RT13 reconstruction as reported in reference [60] viewed top-down and side-on. Note that the purple surface units correspond to TiO_5 truncated octahedra.

7.2 Methods

7.2.1 Synthesis

The solvothermal synthesis of STO developed by Rabuffetti *et al.*[80] was modified to study the effects of substituting different organic acids and Ba for Sr on the surface structure and nanoparticle shape of STO and BTO nanoparticles. STO nanocuboids were prepared using caprylic (octanoic) acid (STO-CA) as the surfactant. Equivalent molar concentrations of titanium tetrabutoxide ($Ti(OBu)_4$) and strontium acetate ($Sr(Ac)_2$) were used in place of the reagents in the previously published method, and the temperature was reduced to 180° C (see Table 7.1 for details).

Table 7.1. Table for synthesis parameters for solvothermal synthesis of BTO and STO, as discussed in this chapter. Note that only one case (with oleic acid as the surfactant) results in A-site rich surface terminations.

A site precursor	B site precursor	T(°C)	Surfactant	pK_a	Primary Faceting	Surface Chemistry	Ref.
$Sr(OH)_2 \cdot 8\ H_2O$	$TiCl_4$	240	Acetic Acid	4.74	{001}	TiO_2	[65]
$Ba(OH)_2 \cdot 8\ H_2O$	$TiCl_4$	180	Acetic Acid	4.74	{001}	TiO_2	This work
$Sr(Ac)_2$	$Ti(OBu)_4$	180	Caprylic Acid	4.89	{001}	TiO_2	This work
$Sr(Ac)_2$	$Ti(OBu)_4$	180	Oleic Acid	9.85	{001}	SrO	[65]
$Sr(Ac)_2$	$Ti(OBu)_4$	240	Glycerol	14.1	{110}	TiO_2	Chapter 4
					{001}*		This work
$Sr(Ac)_2$	$Ti(OBu)_4$	240	Ethanol†	15.9	{001}	TiO_2	Chapter 4

Further details of the BTO synthesis can be found in Chapter 6.

STO dodecahedra were prepared using glycerol (STO-G) as the surfactant; the details of the preparation appear in Chapter 4. Note that the surfactants were removed by sonicating and centrifuging the samples repeatedly in ethanol (STO-G) or deionized water (BTO, STO-CA).

STO cuboids were also prepared using only ethanol as the nominal surfactant, but with microwave heating instead of conventional heating; note that in this case, while the pK_a of ethanol is the highest of the surfactants discussed here, ethanol is fully miscible with water, and cannot play the role of a true surfactant.

---

[*] Minority faceting

[†] Note that ethanol cannot truly serve as a surfactant, as it is fully miscible with water at all concentrations.

For TEM imaging, the samples were dispersed in ethanol and drop cast onto lacey carbon TEM grids. All imaging was performed using the Argonne chromatic aberration-corrected TEM (ACAT) operating at 200 kV.

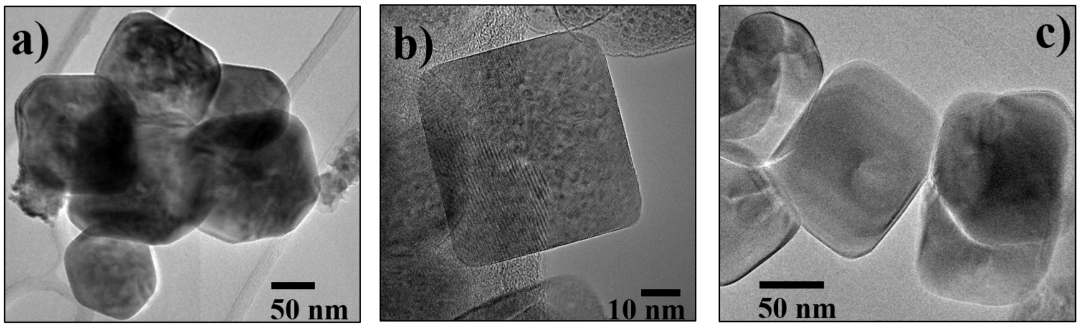

Figure 7.2. Low resolution TEM images of a) BTO b) STO-G and c) STO-CA

7.2.2 Image Simulations

To identify the experimental surface structure, several trial surface structures were used to simulate HREM images using the MacTempas software program. All CIF structures used as input for simulations have been previously reported (see Supporting and/or Supplemental information of references [60] and [122]) with the exception of bulk AO and TiO_2 supercells, which appear in Appendix A. Microscope parameters for all simulations were as follows: spherical aberration coefficient C_s=-0.0050 mm, defocal spread due to chromatic aberration Δf=30 Å, convergence angle α=0.5 mrad, C_5=0, and coma=0. The thickness was varied to fit the experimental images, paying attention to geometric constraints imposed by the shape of the nanoparticles. The defocus was also varied to obtain a good fit to the bulk, so that the agreement with the surface was an unbiased result.

7.3 Results

7.3.1 Experimental Results

The various solvothermal syntheses resulted in nanoparticles with a range of mean particle sizes (defined as the distance between parallel facets): 100 nm for BTO (Figure 7.2a), 140 nm for STO-G (Figure 7.2b), and 80 nm for STO-CA (Figure 7.2c). The particles ranged in size from 50 nm to 130 nm for the BTO case, 20 nm to 200 nm for STO-G, and 40 nm to 80 nm for STO-CA.

The particles synthesized using organic acid surfactants (BTO and STO-CA) resulted in cuboidal shapes, which are predominantly {001} terminated with rounded corners. The STO-G synthesis resulted in rhombic dodecahedra, which are predominantly {110} terminated. (We note that there is minor faceting of {001} present for these particles as well; see Table 7.1.)

HREM revealed the surface morphology of the three different preparations as described in the methods section. All particle surfaces were imaged using profile view imaging,[4,123] which is sensitive to atomic number for thin samples. For the {001} facets, the best structural match was obtained using the RT13 reconstruction (see Figure 7.1) as shown for STO-G (Figure 7.3), BTO samples (Figure 7.4), and STO-CA (Figure 7.5).

There is also a small region (see Figure 7.3 Region 1) that possibly matches a triple layer structure, which matches reasonably well to anatase titania [001] for the extra half unit cell (see Figure 7.3).

Measurements of the *d*-spacings of the surface and subsurface layer were 2.1 Å for the experimental image as depicted in Figure 7.4c and 2.3 Å for the simulation shown in Figure 7.4d. This is a deviation of approximately 10%, which is comparable with the

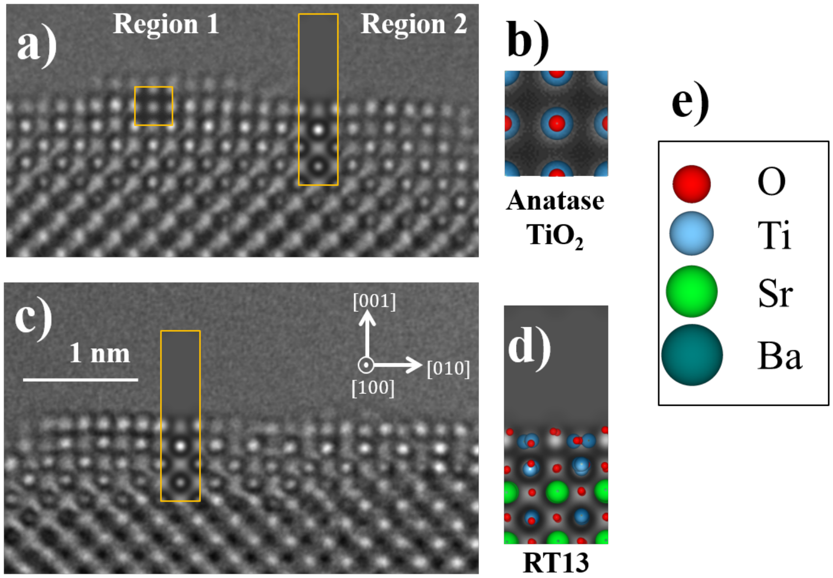

Figure 7.3. a) Experimental image of STO-G (001) surface imaged along the [100] zone axis, with simulated image insets of anatase titania [001] (Region 1) and the RT13 reconstruction (Region 2). b) Atomic structure of anatase TiO_2 unit cell along the [001] zone axis. c) Second experimental image of STO-G (001) surface along the [100] zone, with simulation of STO RT13 inset. d) Atomic structure of the STO RT13 reconstruction viewed along the [100] zone axis. e) Key for colors corresponding to O, Ti, Sr, and Ba used in atomic models. Note that the simulations correspond to a single bulk unit cell (orange box) along the projected direction. The conditions for all simulations were: thickness=39 Å, focus=40 Å, and crystal tilt=0.

difference in the atomic radii between Ba and Sr. Given that the BTO RT13 simulation supercell was constructed by adapting the solved STO structure[60] cells and substituting the Sr atoms with Ba, this is quite good agreement between the simulated and experimental contrast.

Simulated HREM for other possible surface structures appear in Figures 7.8-7.11, including the $(\sqrt{5}\times\sqrt{5})\ R\ 26.6^\circ$ (RT5) and 3×3 as reported in previous work by Kienzle *et al.*[60] as well as the c(6×2) structure reported in work by Ciston *et al.*[122] None of the

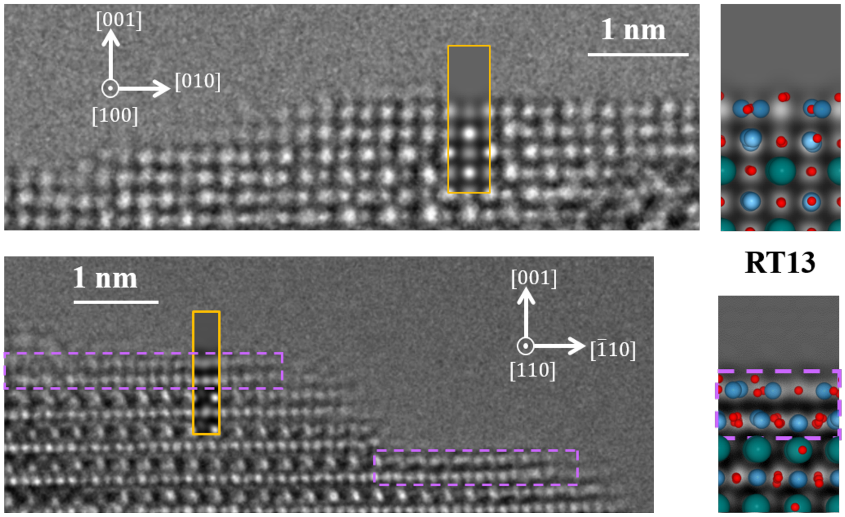

Figure 7.4. a) Experimental image of BTO particle (001) surface imaged along the [100] zone axis and with simulated images of the BTO RT13 reconstruction inset. b) Atomic structure of BTO RT13 along the [100] zone axis. c) Experimental image of BTO particle (001) surface along the [110] zone axis, with simulated image contrast of the BTO RT13 reconstruction inset. d) Atomic structure of the BTO RT13 along the [110] zone axis. The simulations correspond to a single bulk unit cell (orange box) along the projected direction. The conditions for all simulation were: thickness=84 Å, focus=50 Å, and crystal tilt 7 mrad with an azimuthal angle of -45°. Note contrast matching a TiO_2 double layer at the surface terraces (the surface and subsurface layers are highlighted with dashed purple rectangles).

alternatives were an adequate match to the experimental results. Comparable analysis for the {110} facets of STO-G can be found in Chapter 4.

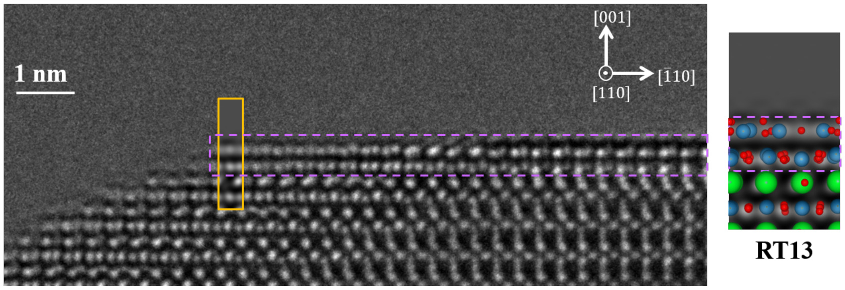

Figure 7.5. a) Experimental image of STO-CA particle (001) surface imaged along the [110] zone axis, with simulated image inset of the STO RT13 reconstruction. b) Atomic structure of the STO RT13. Note that the simulation corresponds to a single bulk unit cell (orange box) along the projected direction. The simulation conditions were: thickness=84 Å, focus=40 Å, and crystal tilt 7 mrad with an azimuthal angle of 45°. Note contrast matching a TiO_2 double layer at the surface (the surface and subsurface layers are highlighted with dashed purple rectangles).

7.3.2 HREM Simulation Results

Here we describe the analysis for surface HREM imaging. Wide-area HREM images of STO along the [110] and [100] zone axes appear in Figure 7.6 below.

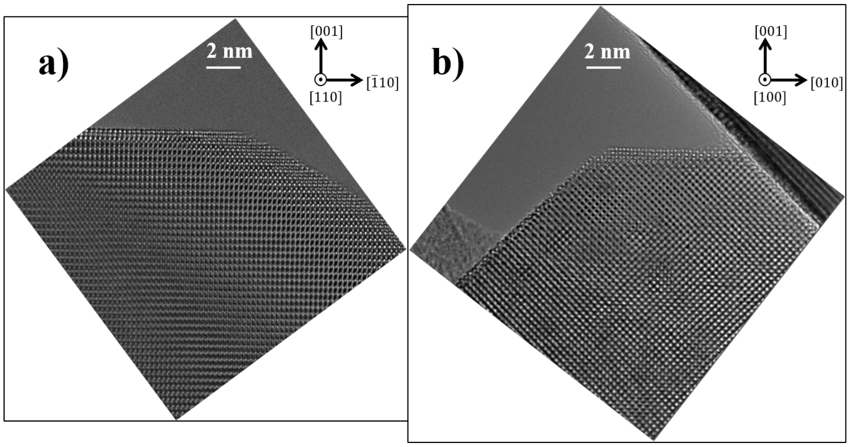

Figure 7.6. Wide area HREM images of a) STO-CA viewed along the [110] zone axis and b) STO-G viewed along the [100] zone axis.

Several candidate structures were used as inputs to simulate images for reasonable estimates of the experimental microscope conditions using the MacTempas software program. MacTempas is an implementation of non-linear imaging theory using the multislice algorithm.[40] As a starting point, bulk crystallographic motifs for STO and BTO were used to construct a map consisting of a montage of images spanning a range of thicknesses and foci. Following this, crystal tilt was added to more closely match the experimental images. The result of this process appears in Figure 7.7 for both STO and BTO.

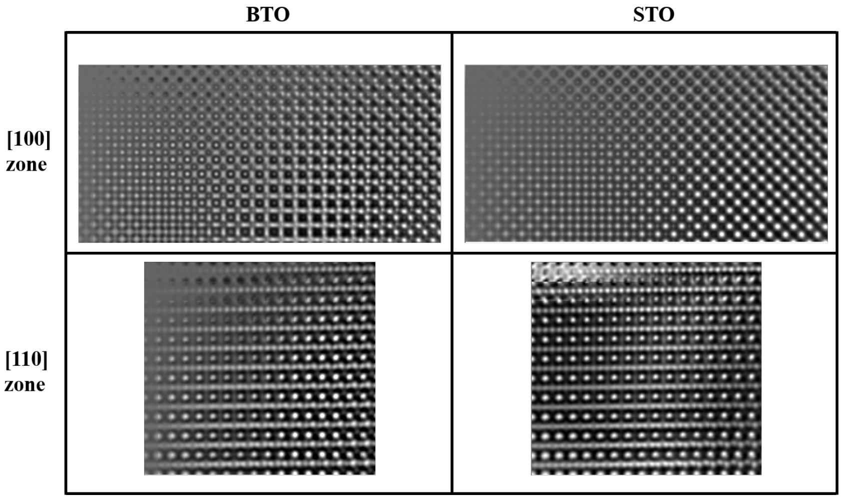

Figure 7.7. Montage of BTO and STO simulated motifs along the [100] and [110] zone axes. Thickness increases from left to right, and focus increases from top to bottom.

Structures that were identified as possible candidates to match the surface contrast include the c(6 × 2), RT13, RT5, (3 × 3), TiO_2 1 × 1, and AO (A=Ba, Sr) 1 × 1. The results of simulations which match best are shown side-by-side with the experimental images, and appear below in Figures 7.8–7.11. For all of the simulations shown, only the top 5 layers (surface, subsurface, and one bulk unit cell) are shown for purposes of comparison.

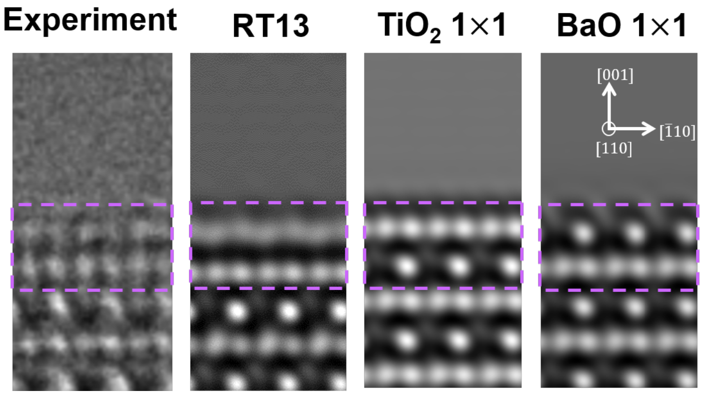

Figure 7.8. Comparison between experiment and simulations for the BTO RT13, TiO_2 1×1, and BaO 1×1 surface structures along the [110] zone axis. The conditions were: thickness of 84 Å, focus of 50 Å, crystal tilt 7 mrad with an azimuthal angle of -45°. From the surface and subsurface layers (purple box), the TiO_2 double layer structure best matched the experimental results.

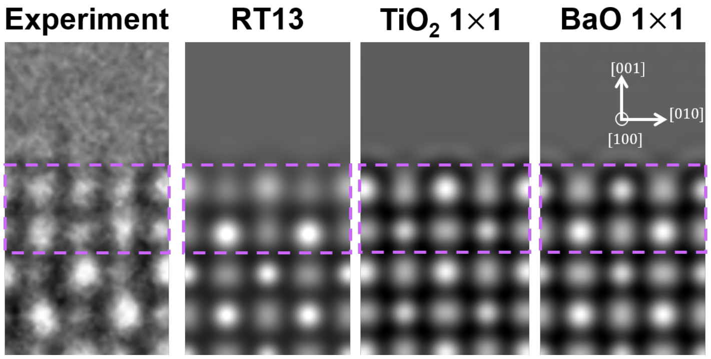

Figure 7.9. Comparison between experiment and simulations for the BTO RT13, TiO_2 1×1, and BaO 1×1 surface structures along the [100] zone axis. The conditions were: thickness of 20 Å, focus of 90 Å, crystal tilt 0. Note that the contrast for both TiO_2 1×1 and BaO 1×1 appears the same along this zone axis.

Note that the BTO RT13 simulation supercell was constructed by adapting the solved STO structure[60] cells and substituting the Sr atoms with Ba.

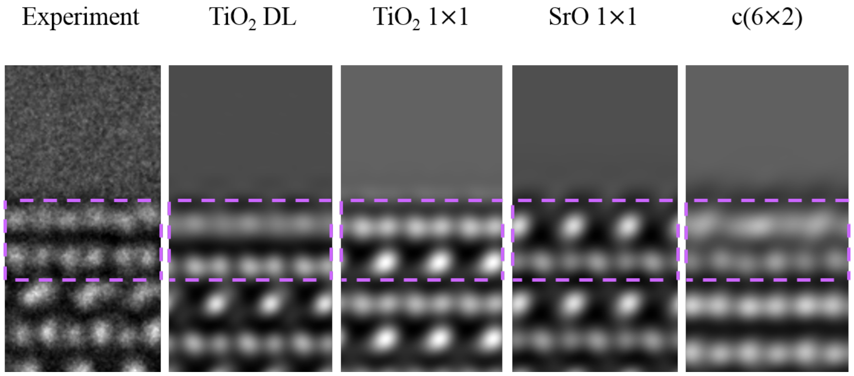

Figure 7.10. Comparison between experiment and simulations for the STO RT13, TiO_2 1 × 1, SrO 1 × 1, and c(6 × 2) surface structures along the [110] zone axis. The conditions were: thickness of 84 Å, focus of 40 Å, crystal tilt 7 mrad with an azimuthal angle of 45°. From the surface and subsurface layers (purple box), the TiO_2 double layer best matched the experimental results.

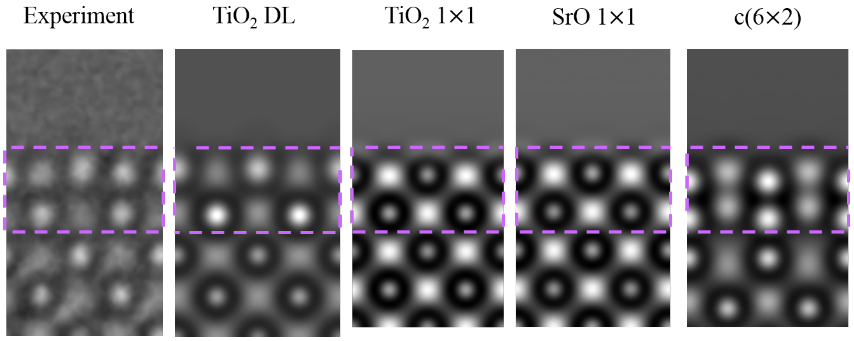

Figure 7.11. Comparison between experiment and simulations for the STO RT13, TiO_2 1 × 1, SrO 1 × 1, and c(6 × 2) surface structures along the [100] zone axis. The conditions were: thickness of 39 Å, focus of 40 Å, crystal tilt 0. Note that the contrast for both TiO_2 1 × 1 and SrO 1 × 1 appears the same along this zone axis.

Simulations for the RT5 and (3 × 3) STO structures appear in Figure 7.12. Both these structures are terminated with TiO_2 double layers, and agree well with experimental contrast along the [110] zone axis. However, neither agrees well when viewed along the [100] direction. This, combined with the relative positions of these structures on the convex hull, makes the RT13 reconstruction the most likely surface termination for the experimental conditions.

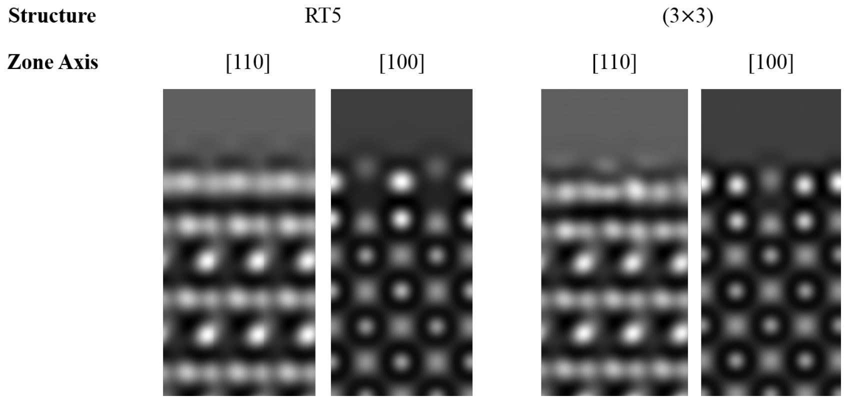

Figure 7.12. Simulated images for the RT5 and (3 × 3) surface structures along the [110] and [100] zone axes. The conditions were the same as the STO simulations in Figure 7.10 and Figure 7.11 along their respective directions.

The small region which matches an extra half-unit cell of anatase titania, agrees with observed growth of anatase titania on STO single crystals.[124]

7.4 Discussion

7.4.1 Surface Structure

All syntheses discussed here resulted in surfaces terminations that match contrast of the RT13 structure. The RT13 structure has a TiO_2 double-layer (DL) at the surface, and has previously been observed on STO nanocuboids prepared using acetic acid, as well as single crystals.[60,65,125] The observation of a small region which matches the anatase titania structure confirms literature reporting stable epitaxial growth of anatase titania on STO single crystals.[124] The results for both the {001} and the {110} indicate that TiO_2-rich surfaces are very common, and are likely pervasive for hydrothermal synthesis.

7.4.2 Role of Surfactants and Water

It is well-known that acid etching preparation of bulk single crystal STO produces TiO_2-rich surfaces.[126–129] In fact, there are several reports of deionized water etching STO to obtain TiO_2-terminated surfaces.[130,131] In these cases the pH was in the acidic range (below 7), which preferentially etches SrO, a basic oxide.

In our case, the pH of the solution is significantly higher (~14) during the growth phase of the nanoparticle synthesis. Alkaline conditions are required to stabilize the formation of crystalline BTO and STO.[102,105] Comparing the nanoparticle growth conditions with the etching conditions reported for single crystal studies, the presence of surfactants is a key difference between the two. Thus, for our case, the surfactants will play a key role in determining the final surface chemistry of the nanoparticles.

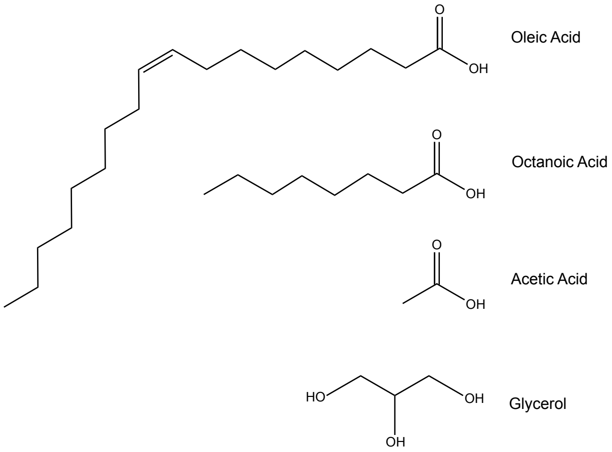

Figure 7.13. Molecular structure of various surfactants used in hydrothermal synthesis of titanates. All except oleic acid are used in this study.

It is also well-known that surfactant molecules can significantly change the shape of nanoparticles through preferential adsorption during the growth process. Several surfactants were investigated in this study. Acetic acid and caprylic acid are both carboxylates with the same functional group. Glycerol is a multidentate poly-ol with a very different molecular structure from the organic acids employed in our study (see Figure 7.13 for a direct comparison). Large differences in acidity can be seen by the wide range pK_a values in Table 7.1. Despite these differences, all syntheses yielded titania-rich surfaces. A discussion of stabilization of alkali and alkaline earth metal ions by various ligands can be found in work by Daniele *et al*.[132] The instability of such ionic complexes with alcohol compared with carboxylates can inform the observation of titania-rich {110} surfaces as reported in previous work,[133] and {001} surfaces in this study.

In studies on single crystals, SrO_x surfaces are obtained by annealing at high temperatures in oxygen-rich environments.[134–137] Water is known to react with SrO to form $Sr(OH)_2$.[138] The case of BaO is similar;[139] like SrO,[140] it will readily form a hydroxide, which will not revert to the oxide unless heated in an inert atmosphere to temperatures between 530 and 600 °C. Thus, it is important to protect A-site terminated surfaces to prevent hydrolysis and subsequent dissolution.

To date, the only nanoparticle syntheses reported in the literature that result in A-site terminated surfaces involve the use of liquid microemulsions.[71,79] For the purposes of this study, the molecular structure is the important factor to determine the surface chemistry; see differences in Figure 7.13. With sufficient packing density of the surfactant,[78] and a sufficiently long hydrocarbon tail, the surfaces should be protected from aqueous dissolution by steric hindrance. By targeting a water-poor region of the water/oil/alcohol phase diagram in which lamellar liquid crystals form, SrO-terminated nanocrystals were obtained using oleic acid in previous work by Hu *et al.*[65,71,79] While it is likely that other reports in the literature which use similar reaction conditions also result in A-site terminated surfaces, characterization to determine this is not reported.[141,142]

7.4.3 Comparison with first-principles predicted structures

Turning now to the specific surface structure, the RT13 surface structure was observed for all materials discussed in this article, independent of the choice of organic acid or glycerol, with the exception of oleic acid (see HREM work by Dr. Yuyuan Lin *et al* in reference [65]). The RT13 surface reconstruction is one of the low energy structures as evidenced by the convex hull construction shown in Figure 7.14. It was first produced and solved for flat surfaces by treating large single crystals using buffered etching conditions, and annealed in oxidizing environments. It has since been observed for many other cases with the (001) surface of STO[125,128] and has been reported in one paper for BTO.[143]

7.4.4 Thermodynamic analysis

The STO (001) surface energies vary as function of the excess of TiO_2 as shown in Figure 7.14. Here, the surface energies computed from DFT calculations correspond to enthalpies of formation. These are calculated with reference to bulk STO and rutile TiO_2, and are normalized to a single unit cell of (001) STO, in equilibrium with vacuum.

For the hydrothermally synthesized BTO and STO nanoparticles, we must also consider the thermodynamics of the surface dissolution in the aqueous synthesis enviroment. Specifically, the enthalpies of the following reactions which describe the dissolution of

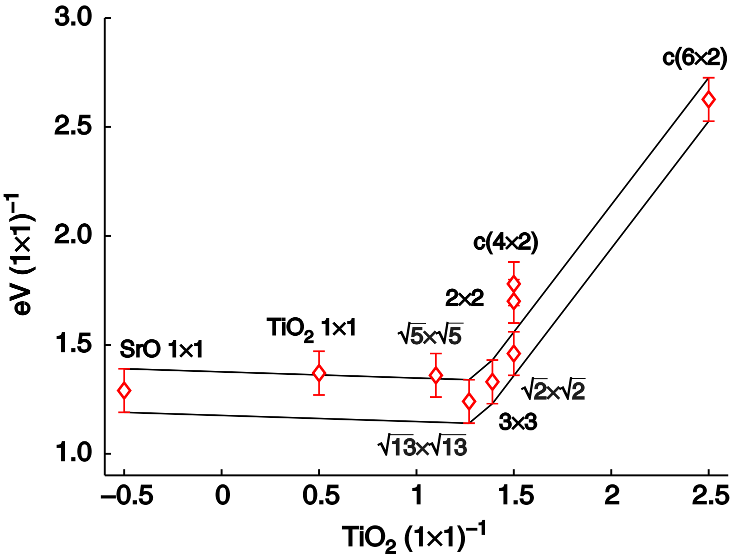

Figure 7.14. Surface enthalpies versus excess TiO_2 at the surface, calculated from DFT known reconstructions on strontium titanate {001} surfaces. The energies are referenced to bulk STO and rutile TiO_2. Reproduced with permission from reference [122].

the surface STO layer are considered:

$$\mathrm{SrTiO_3\,(bulk)} \rightleftharpoons \mathrm{SrO\,(s)} + \mathrm{TiO_2\,(s)} \tag{7.1}$$

$$\mathrm{SrTiO_3\,(bulk)} + 2\,\mathrm{H_2O} \rightleftharpoons \mathrm{SrO\,(s)} + \mathrm{Ti^{4+}\,(aq)} + 4\,\mathrm{OH^-\,(aq)} \tag{7.2}$$

$$\mathrm{SrTiO_3\,(bulk)} + 2\,\mathrm{H_2O} \rightleftharpoons \mathrm{SrO\,(s)} + \mathrm{Ti(OH)_4\,(s)} \tag{7.3}$$

$$\mathrm{SrTiO_3\,(bulk)} + \mathrm{H_2O} \rightleftharpoons \mathrm{TiO_2\,(s)} + \mathrm{Sr^{2+}\,(aq)} + 2\,\mathrm{OH^-\,(aq)} \tag{7.4}$$

$$\mathrm{SrTiO_3\,(bulk)} + \mathrm{H_2O} \rightleftharpoons \mathrm{TiO_2\,(s)} + \mathrm{Sr(OH)_2\,(s)} \tag{7.5}$$

$$\mathrm{SrTiO_3\,(bulk)} + 9\,\mathrm{H_2O} \rightleftharpoons \mathrm{TiO_2\,(s)} + \mathrm{Sr(OH)_2 \cdot 8\,H_2O\,(s)}. \tag{7.6}$$

In general, the surface STO (nominally a linear combination of SrO and TiO_2) will dissociate into the constituent components of bulk rutile TiO_2 and rock salt SrO according to reaction 7.1. For TiO_2 dissolution, we compare the enthalpies of reactions 7.1–7.3, and similarly, for SrO dissolution, we compare the enthalpies of reactions 7.1, 7.4, 7.5, and 7.6. The referenced standard enthalpies of formation appear in Table A.1 in Appendix A.

The most energetically favorable reactions for the TiO_2 dissolution will be given by

$$\Delta H_{\text{dissolution, Ti}} = \min\left\{\Delta H_{7.1}, \Delta H_{7.2}, \Delta H_{7.3}\right\}, \tag{7.7}$$

where ΔH_n on the right hand side of the equation are the enthalpy changes for reactions 7.1–7.3, and $\Delta H_{\text{dissolution, Ti}}$ is the minimum enthalpy required for TiO_2 dissolution. According to Table 7.2, this corresponds to 1.39 eV/1×1 for reaction 7.1.

The most energetically favorable reaction for the SrO dissolution will be given by

$$\Delta H_{\text{dissolution, Sr}} = \min\left\{\Delta H_{7.1}, \Delta H_{7.4}, \Delta H_{7.5}, \Delta H_{7.6}\right\}, \tag{7.8}$$

where ΔH_n on the right hand side of the equation are the enthalpy changes for each of reactions 7.1, 7.4, 7.5, and 7.6, and $\Delta H_{\text{dissolution, Sr}}$ is the minimum enthalpy required for the dissolution of SrO. From Table 7.2, this corresponds to −0.64 eV/1×1 for reaction 7.6.

For a given surface composition, the enthalpy of the TiO_2/SrO dissolution reaction must be added to the surface enthaply to give a net enthalpy H_{net} described by

$$H_{\text{net}}(x) = \begin{cases} H_{\text{DFT}}(x) + |x|\Delta H_{\text{dissolution, Ti}}\,, & x \leq 0 \\ H_{\text{DFT}}(x) + |x|\Delta H_{\text{dissolution, Sr}}\,, & x > 0 \end{cases} \tag{7.9}$$

where x is the excess surface TiO_2 (in units of TiO_2/1×1), H_{DFT} is the vacuum surface enthalpy of surface structures along the convex hull, and $\Delta H_{\text{dissolution, Ti}}$ and $\Delta H_{\text{dissolution, Sr}}$

are the enthalpy changes for the dissolution of TiO_2 and SrO, respectively, also normalized to units of eV/1×1. The result of adding these dissolution terms is reflected by a shift in the convex hull, as shown in Figure 7.15.

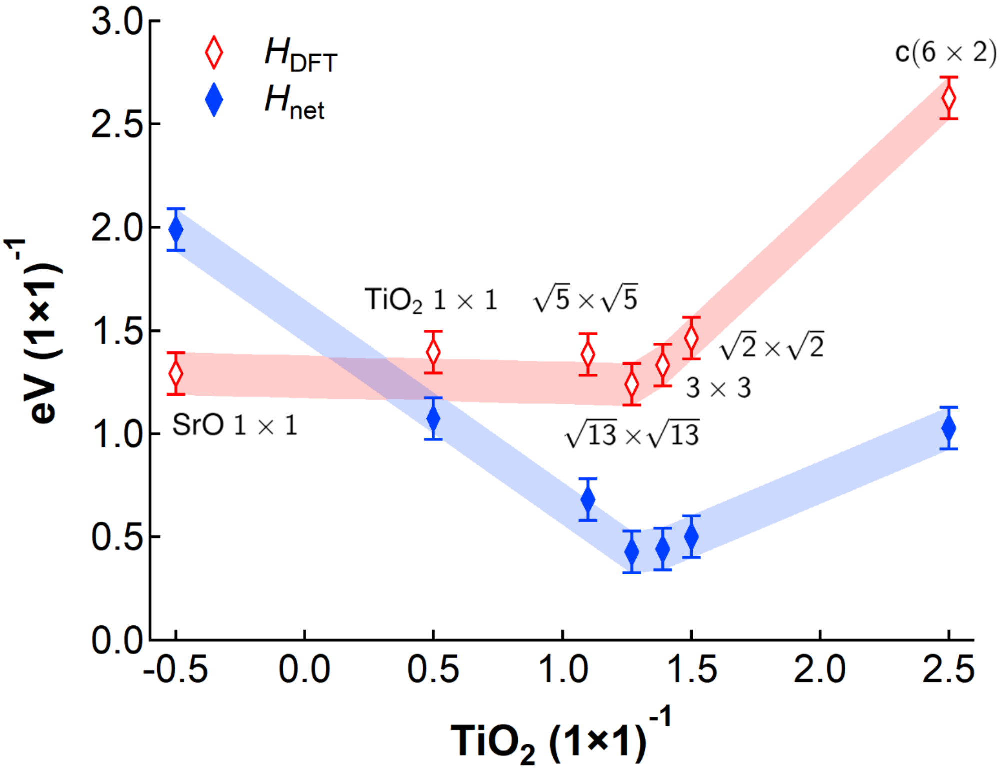

Figure 7.15. Effect of dissolution and hydrolysis of STO surface SrO and TiO_2 on the convex hull. The red points and shaded region correspond to the vacuum DFT surface enthalpies within DFT error of the convex hull, and blue points and shaded region correspond to the net surface enthalpies taking dissolution of SrO and/or TiO_2 into consideration.

This shift is asymmetric because of the greater increase in enthalpy for dissolving TiO_2, which further favors structures on the right hand side ($x > 0$) of the convex hull. Thus, SrO dissolution is favored over that of TiO_2. Note that the RT13 structure is the minimum energy structure with respect to the vacuum energies from DFT and the shifted values after dissolution of surface SrO.

Table 7.2. Dissolution enthapies for TiO_2 and SrO dissolution reactions 7.1–7.6.

Reaction	$\Delta H^{o}_{\text{reaction}}$ (kJ/mol)	$\Delta H^{o}_{\text{reaction}}$ (eV/1×1)
(7.1)	134.35	1.39
(7.2)	241.61	2.50
(7.3)	140.72	1.46
(7.4)	1.25	0.013
(7.5)	0.62	0.006
(7.6)	−61.74	−0.64

7.5 Conclusion

Hydrothermal routes to synthesize titanate nanomaterials in aqueous environments generally result in TiO_2-rich surfaces. These surfaces are stable as 4- and 5-coordinated polyhedra, as confirmed by HREM. While TiO_6 octahedra are preferred, truncated octahedral TiO_5 units[60] form the framework of the RT13 reconstruction observed on STO (001), and TiO_4 tetrahedra are the building blocks of the $(n \times 1)$ homologous series of reconstructions[64,113] observed on the STO (110) surface. The driving for the formation of the TiO_2-rich surfaces is thermodynamics in aqueous conditions.

CHAPTER 8

Adhesion of Pt and Pd Nanoparticles on Oxide Supports

8.1 Introduction

Previous chapters described work to synthesize and characterize shape-controlled nanoparticles. The motivation is to use them in applications that depend upon surface chemistry, such as heterogeneous catalysis. This chapter details work to engineer catalytic systems using {110}- and {001}-faceted STO particles as catalyst supports. Two noble metals, platinum and palladium, were studied as candidates because of their close lattice match (3.92 Å and 3.89 Å, respectively) compared to 3.905 Å for STO.

8.1.1 Winterbottom Modeling

When depositing a material onto an idealized flat substrate, one must consider the vapor (or liquid) phase, substrates, and the deposited material.[144]

Typically, one would use the Winterbottom construction[145] to model the equilibrium shape for a particle in contact with a flat substrate. The minimum energy configuration takes the intersection between the thermodynamic Wulff shape (see Chapter 3 for a description) and the substrate. For a flat material, this amounts to slicing through the Wulff shape at a height which will be determined by a single energy term, which we can define as the interfacial energy:

$$\gamma_{\text{int}} = \gamma_{\text{pv}} + \gamma_{\text{bond}}. \tag{8.1}$$

Here the interfacial energy γ_{int} will depend upon the particle-vapor surface energy of γ_{pv}, and an affinity or bonding term γ_{bond}. The interfacial energy can be either positive or negative depending upon the local material structure at the interface, material properties such as lattice misfit, polarity, and the chemical affinity between the particle and substrate. Figure 8.1 shows the effect of changing the interfacial energy upon the particle adhesion to the substrate. The two limiting cases, total wetting and total dewetting, will occur when $\gamma_{\text{int}} \leq -\gamma_{\text{pv}}$ and $\gamma_{\text{int}} \geq \gamma_{\text{pv}}$, respectively.

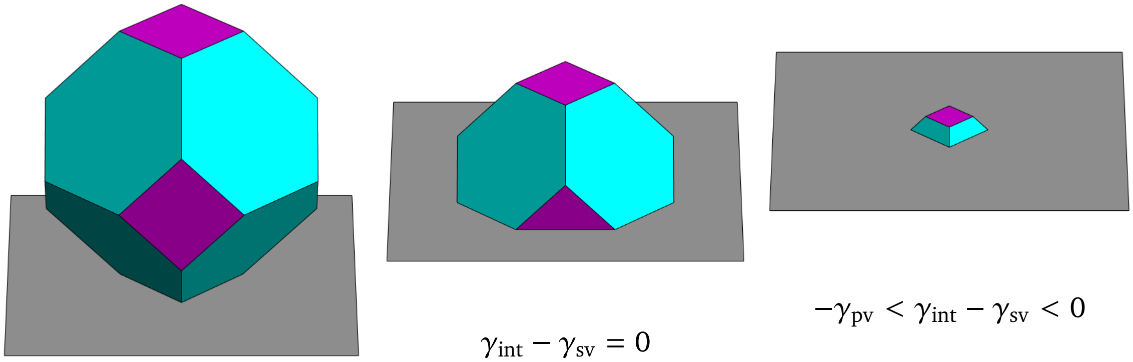

$\gamma_{\text{int}} - \gamma_{\text{sv}} = \gamma_{\text{pv}}$

$\gamma_{\text{int}} - \gamma_{\text{sv}} = 0$

$-\gamma_{\text{pv}} < \gamma_{\text{int}} - \gamma_{\text{sv}} < 0$

Figure 8.1. Schematic showing three distinct cases of wetting of a crystalline material on a substrate. Left shows complete dewetting, where $\gamma_{\text{int}} - \gamma_{\text{sv}} = \gamma_{\text{pv}}$. The middle illustrates the case where $\gamma_{\text{int}} = 0$. Right shows near complete wetting, where γ_{int} is negative but greater than the absolutive value of the particle surface energy. Not shown is the case where where $\gamma_{\text{int}} \leq -\gamma_{\text{p}}$, which would be complete wetting. Graphic generated using the WulffMaker Winterbottom Mathematica code.[52]

8.1.2 Multiply Twinned Particles and a modified Winterbottom construction

For defect-free crystalline materials, the minimum energy shape will be given by the thermodynamic Wulff construction. However other shapes are possible. For FCC metals in particular, it is well-known[146–151] that one can form a variety of twinned shapes. These shapes, which are modeled by the modified Wulff construction,[147,149] include lamellar twinned particles, decahedra, and icosahedra, as well as several variants with re-entrant faceting. Both decahedra and icosahedra are classified as multiply twinned particle (MTP) and are constructed of tetrahedra units joined along {111} planes (see Figure 8.2 for an illustration of a decahedron wetting a substrate).

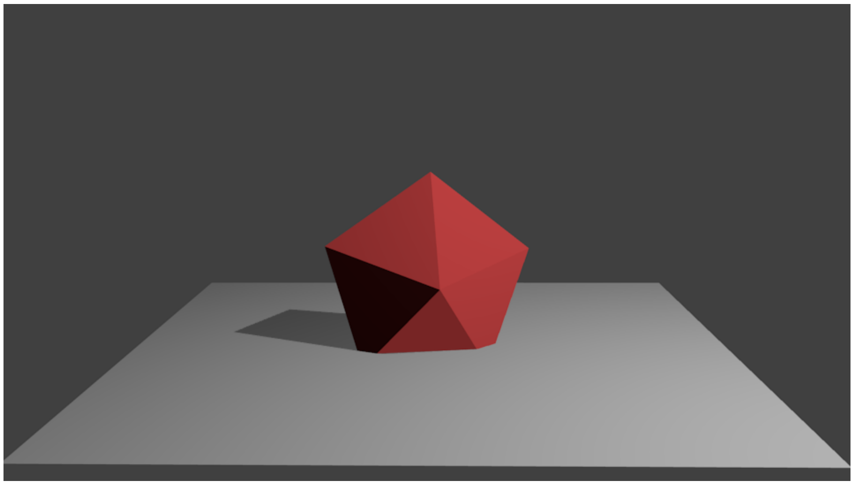

Figure 8.2. Illustration of decahedral MTP composed of five tetrahedra wetting a substrate. Note that joining tetrahedra together in this manner will not fill space, leaving a gap. This gap is closed by straining the tetrahedra, introducing a defect known as a disclination. See reference [147] for more details.

There are several reasons why twins can change the adhesion of particles to a substrate. One is that local coordination environment around the twin will be changed from that of a single crystal, resulting in a change in γ_{bond}. Another is the introduction of strain, both internal to the particle, and between the particle and substrate. The presence of twins will also introduce rotations between the particle lattice and the substrate lattice due to the multiplicity of segments in contact with substrate. This will be a dominating term because it is no longer possible to have a single particle/substrate interface, as will be discussed next.

The first order correction to the Winterbottom construction for the case of MTPs would be to consider the addition of new interfaces for each twin segment in contact with the substrate. Doing so, we can define total interfacial energy of the system as

$$E_{\text{int}}^{\text{tot}} = \sum_i \gamma_{\text{int}}^i A_{\text{int}}^i , \tag{8.2}$$

where γ_{int}^i are the interfacial energies for each of the particle segments in contact with the substrate, A_{int}^i are the contact areas for each of these segments, and $E_{\text{int}}^{\text{tot}}$ is the total interfacial energy. To facilitate the comparison of different particle shapes, we can define an effective interfacial energy:

$$\gamma_{\text{int}}^{\text{eff}} = \frac{\sum\limits_i \gamma_{\text{int}}^i A_{\text{int}}^i}{\sum\limits_i A_{\text{int}}^i}, \tag{8.3}$$

where $\gamma_{\text{int}}^{\text{eff}}$ is the effective interfacial energy and the other variables are the same as above.

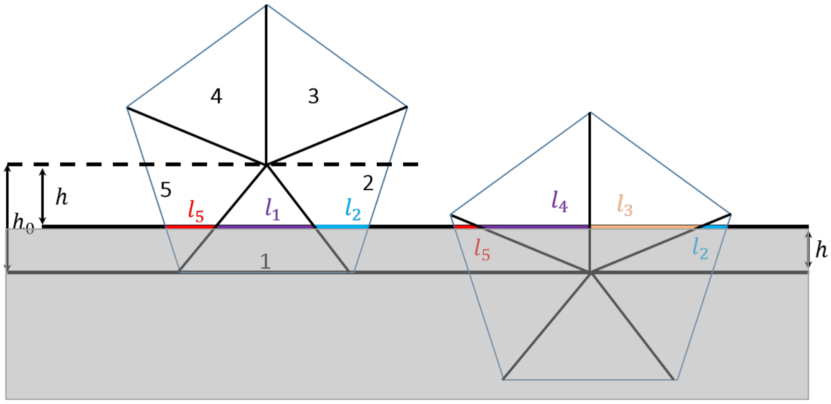

Figure 8.3. Two-dimensional illustration of a decahedron wetting a substrate surface. The segments are labeled from 1 through 5 counterclockwise. On the left is a case with three segments in contact with the substrate, with lengths l_1, l_2, and l_5. On the right is a case with four segments in contact with the substrate, with lengths l_2, l_3, l_4, and l_5.

To demonstrate this analysis, we will consider a two-dimensional analogue, as shown in Figure 8.3. Instead of a contact area, we will have a contact length, l. For the case of a decahedron with five twins, which is a pentagon when projected in two dimensions, there will a total of five tetrahedral units, shown as triangles in the illustration.

If we assign interfacial energies γ_i for all of the segments, we can determine what level of wetting will be optimal for the system. As an example, let us take the case of three segments in contact as shown on the left. The total length l will be the sum of the segments in contact with the substrate i.e. The total length l will be the sum of the segments in contact with the substrate i.e.

$$l = \begin{cases} l_1 + l_2 + l_5 & 0 \leq h < h_0 \\ l_2 + l_3 + l_4 + l_5 & -h_{\text{crit}} < h < 0 \\ l_3 + l_4 & h \leq -h_{\text{crit}} \end{cases} \tag{8.4}$$

where l_i are the segment contact lengths, h is the exposed height as shown in Figure 8.3, h_0 is the Wulff center distance, and h_{crit} is a critical h value at which the contact length for segments 2 and 5 goes to zero. The value of h_{crit}, determined using geometry, is $h_0 \frac{\sin 72° \sin 18°}{\sin 54° \sin 108°} \approx 0.382 h_0$. By symmetry we can simply this expression by substituting $l_2 = l_5$ and $l_3 = l_4$:

$$l = \begin{cases} l_1 + 2l_2 & 0 \leq h < h_0 \\ 2l_2 + 2l_3 & -h_{\text{crit}} < h < 0 \\ 2l_3 & h \leq -h_{\text{crit}} \end{cases} \tag{8.5}$$

In the fully dewetted case $l_1 = h$, $l_2 = 0$, and the total contact length l will be l_1. The effective surface energy will be γ_{100} in this case for the figure as drawn. For the case where the particle exposed height h is positive and less than the Wulff center distance h_0 we will have the following relationships for l after accounting for geometry:

$$l = l_1 + 2l_2 \qquad 0 \leq h < h_0 \tag{8.6}$$

$$l = 2h \tan 36^\circ + \frac{2(h_0 - h)}{\sin 72^\circ} \tag{8.7}$$

$$\approx 2.103\, h_0 - 0.65\, h \tag{8.8}$$

In the partially wetted case where $-h_{\text{crit}} < h < 0$ we will have

$$l = 2l_2 + 2l_3 \qquad h_{\text{crit}} < h < 0 \tag{8.9}$$

$$l = 2|h_{\text{crit}} - h| \frac{\sin 54^\circ}{\sin 18^\circ \sin 72^\circ} + 2|h| \tan 72^\circ \tag{8.10}$$

$$\approx 5.51|h_{\text{crit}} - h| + 6.156h \tag{8.11}$$

And for the case with partial wetting where $h \leq -h_{\text{crit}}$ the effective surface energy will be γ_{110} and the contact length will be given by

$$l = 2l_3 \qquad h \leq -h_{\text{crit}} \tag{8.12}$$

$$l = 2|h - h_{\text{crit}}| \frac{1}{\tan 36^\circ} \tag{8.13}$$

$$\approx 2.75|h - h_{\text{crit}}| \tag{8.14}$$

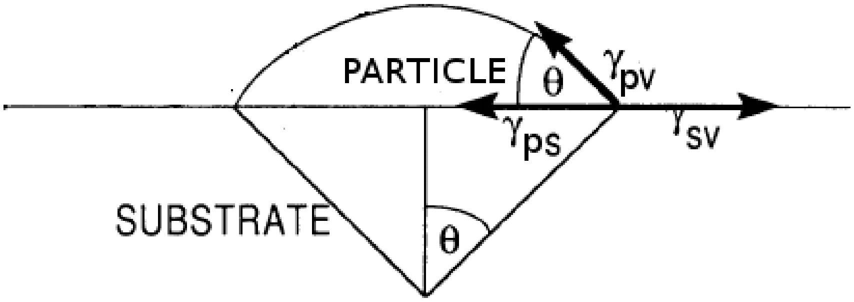

Figure 8.4. Illustration of wetting of a droplet on a substrate according to the Young-Dupré model. Figure adapted from reference [144].

8.1.3 Relation to droplet wetting model

With many segments in contact with the substrate, it should be a reasonable approximation to use the spherical droplet model. While this model does not account for anisotropy of faceting, it does provide a good measure of the level of truncation. The contact angle for a droplet in equilibrium with a surface is related to the surface energies of the substrate and the particle through the Young equation:

$$\gamma_{\mathrm{sv}} = \gamma_{\mathrm{pv}} \cos\theta + \gamma_{\mathrm{sp}}, \tag{8.15}$$

where θ is the contact angle, γ_{sv} is the substrate surface energy, γ_{pv} is the particle surface energy, γ_{sp} is the particle-substrate interfacial energy. Both the substrate and particle surface energies are implicitly in equilibrium with a vapor phase, which is taken to be vacuum for modeling purposes.

8.2 Experimental

8.2.1 Deposition of Pt and Pd on STO

ALD is a technique that leverages gas-phase chemistry to deposit materials onto a substrate in a rate-controlled fashion. Carried out in a viscous flow reactor,[152] ALD has the property of being self-limiting based upon available binding sites on the substrate. To grow metals, typically organometallic complexes are used, and they are cycled with a radical generating gas such as water or ozone to remove the organic ligands and leave behind the metal adsorbates. These adsorbates can migrate along the surface to nucleate and grow into particles. There are cases where small clusters and even single atoms of metals have been deposited and stabilized using this technique.[153] ALD was used to deposit both platinum and palladium onto STO nanoparticles.

Wet impregnation is a deposition technique that uses solution-based chemistry to adsorb coatings and small particles on another material. It relies upon chemical potential gradients and electrostatic forces to drive the nucleation and growth from aqueous species in the liquid phase to the solid that is being coated. By comparison with ALD, wet impregnation can quickly deposit large quantities of material, but in a less controlled manner.

Platinum samples were prepared by collaborator Ryan Hackler. The precursor used for platinum ALD was (methylcyclopentadienly)trimethly platinum ($MeCpPtMe_3$). The platinum ALD used alternating 120 s exposures of $MeCpPtMe_3$ followed by 120 s of 10% ozone in oxygen at 300 °C. Each cycle was followed by a 120 s purge under nitrogen. Samples were prepared with 1 and 3 cycles on both supports. They were deposited onto the {110}-faceted STO dodecahedra as well as anatase titania supports purchased from Sigma Aldrich. More details about the platinum-titania samples can be found in Chapter 9.

Palladium samples were prepared by collaborators via both wet impregnation and ALD. Dr. Cassie George carried out the ALD deposition, using palladium(II) hexafluoroacetylacetonate ($Pd(C_5HF_6O_2)_2$ or $Pd(hfac)_2$) and formalin the palladium precursors. The palladium ALD used alternating 300 s exposures of $Pd(hfac)_2$ and formalin followed by 300 s of 10% ozone in oxygen at 200 °C. Each cycle was followed by a 300 s purge under nitrogen. Samples were prepared with 1, 5, and 10 cycles. Dr. Bor-Rong Chen prepared additional samples via wet impregnation using palladium nitrate $Pd(NO_3)_2$ was used as the metallic salt under ambient conditions. Both deposition techniques were employed to deposit palladium on both STO nanocuboids and dodecahedra.

8.2.2 HREM Imaging of Metal–Oxide interface

Several microscopes were used to study the particle wetting using HREM. A probe-corrected JEOL ARM 200CF at UIC was used primarily for atomic resolution HAADF imaging. The ACAT, a C_s/C_c corrected Titan 80-300ST was used for HREM in parallel illumination. A JEOL 2100F was used for conventional HREM imaging. All microscopes were operated at 200kV.

8.2.3 Measurement of contact angle

For the case of multiply-twinned particles, contact angle measurements were carried out to measure the particle wetting to facilitate comparison of metal particle adhesion on the oxide supports. The contact angle was measured by fitting a circle of radius r to particles identified in experimental HREM images. The edge of the substrate was marked with a line, and the contact length was measured at this height. These two values can be related to the contact angle θ through the equation

$$\theta = \begin{cases} \frac{\pi}{2} - \arccos \frac{l}{r} & h_{\text{exp}} \geq r \\ \frac{\pi}{2} + \arccos \frac{l}{r} & h_{\text{exp}} < r, \end{cases} \tag{8.16}$$

where l is the contact length, r is the particle radius h_{exp} is the exposed height of the particle, and θ is the contact angle as defined above. Figure 8.5 illustrates the geometrical relationship between the contact angle, the contact length and the radius for a spherical droplet. All measurements were performed using the ImageJ software.

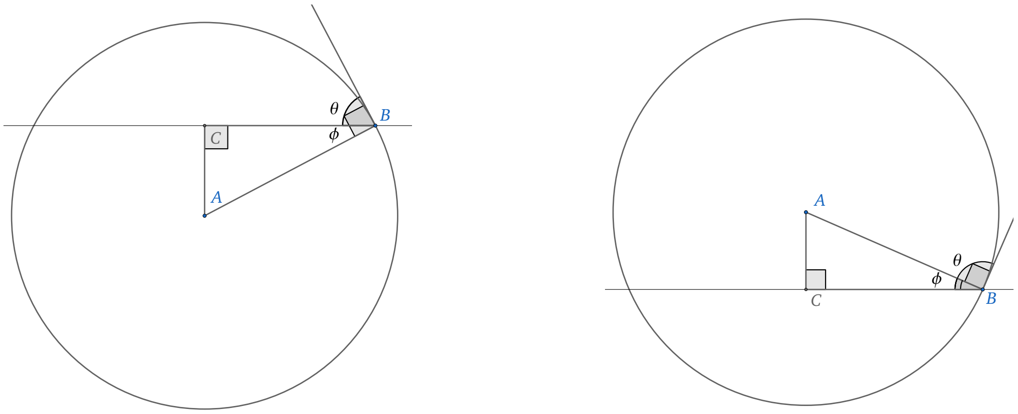

Figure 8.5. Geometrical illustration of contact angle and particle wetting. The left case shows particle wetting, where $h_{\text{exp}} < r$. The right shows the dewetting case, where $h_{\text{exp}} \geq r$.

8.3 Results

The platinum samples with 1 and 3 ALD cycles were confirmed by inductively coupled plasma (ICP) analysis to have 1.1 and 3 wt%, respectively. Platinum particles for the two ALD preparations were found to have average particle sizes of 1.38 nm with a standard deviation of 0.84 nm and 2.69 nm with a standard deviation of 0.67 nm, respectively. Palladium samples grown by ALD were confirmed by ICP to have 0.2, 1.0, and 1.2 wt% loadings for 1, 5, and 10 cycles, respectively. The palladium particles had averages sizes of 2.6 nm with a standard deviation of 0.8 nm, 2.9 nm with a standard deviation of 0.5 nm, and 3.2 nm with a standard deviation of 0.7 nm for the three respective loadings. The wet impregnation samples had 3 wt% mass loading, with an average particle size of 7.6 nm with a standard deviation of 1.9 nm.

HREM imaging revealed that the particle shape and wetting varied significantly depending upon the particle material and the support. Additionally, there were significant numbers of MTPs for palladium. These phenomena motivated further study, the description of which follows.

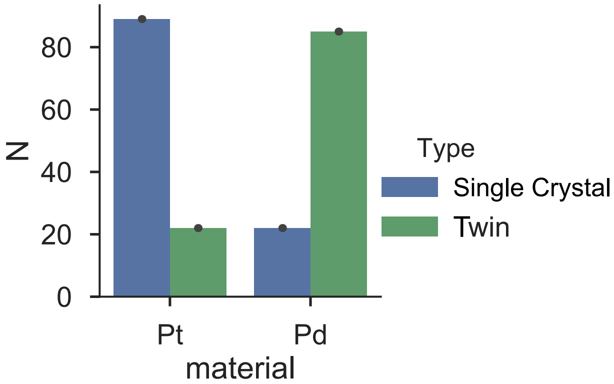

Figure 8.6. Population statistics for images of platinum and palladium nanoparticles observed by HREM. *N* is the total number of particles observed for each material. More that 100 particles were counted for each material, and 80% of the platinum particles were single crystals, while about the percentage were twinned particles for palladium.

8.3.1 Populations of single crystals and twinned particles for platinum and palladium

A comparison of platinum and palladium populations appears in Figure 8.6. For platinum, 111 particles were counted, and 80% identified as single crystals. This observation agrees with previous work by Dr. James Enterkin[54,154] for platinum deposited on STO nanocuboids. For palladium, 107 particles were counted, and 78% of the particles were identified as MTPs or lamellar twinned particles. Note that for the palladium case, the majority of the particles are MTPs, which is the opposite of the platinum case.

A visual summary of the different particle types observed for palladium appears in Figure 8.7. Several types of MTPs were observed, including icosahedra and decahedra.

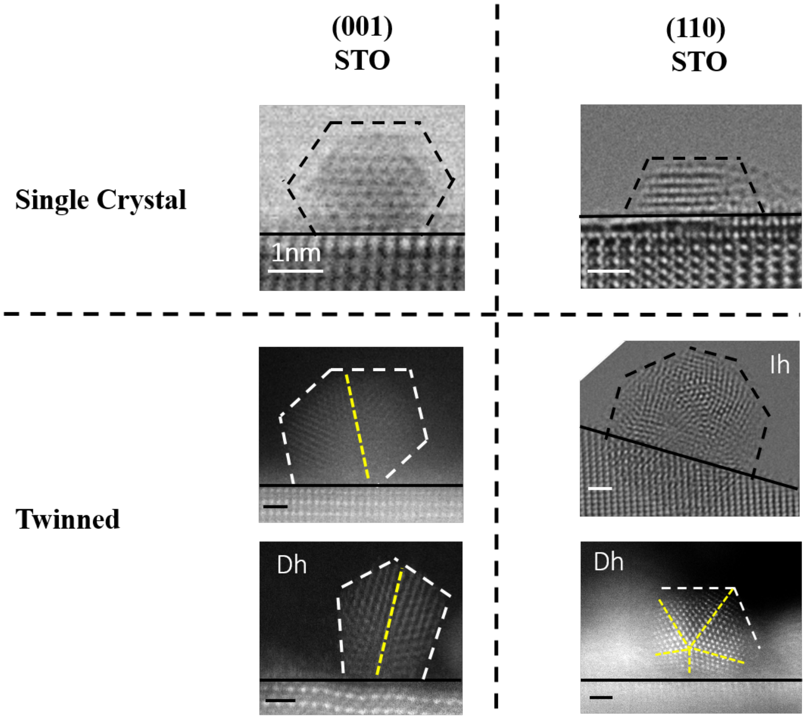

Figure 8.7. Summary of types of palladium particles observed after deposition on both (001) and (110)-faceted STO nanoparticles. The labels Dh and Ih refer to decahedron and icosahedron, respectively. The scale bar of 1 nm applies to all images.

Figure 8.8 shows the contact angle distribution for palladium nanoparticles. Note that this includes particles grown by both wet impregnation and ALD, and both STO supports. The mean contact angle was 114° with standard deviation of 18.1.

For platinum, the majority of the particles were single crystals, and no MTPs that could be identified were observed. A representative image of the particle morphologies appears in Figure 8.11. The contact angle distribution for platinum appears in Figure 8.12. The mean contact angle was 101° with a standard deviation of 30°. Note that there are two maxima, which correlate well with two different STO supports.

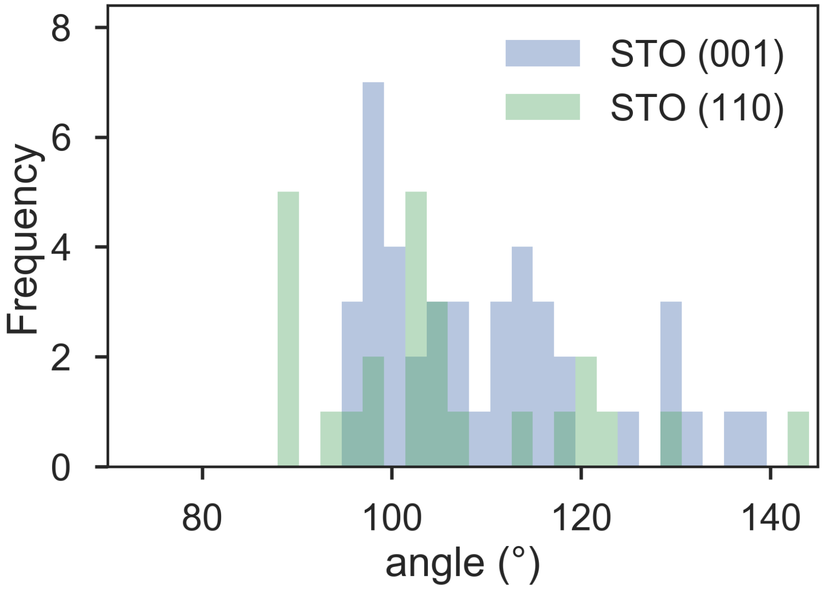

Figure 8.8. Histogram showing the distribution in contact angles measured for palladium nanoparticles after deposition on STO supports. Note that this includes both single crystals and twinned particles.

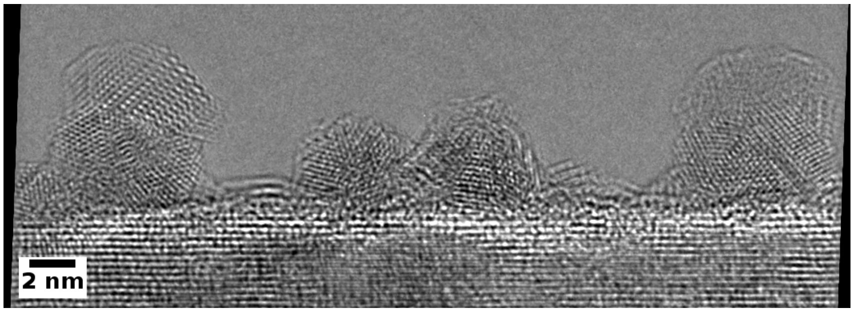

Figure 8.9. HREM image of palladium nanoparticles on STO (110) surface. Note several decahedra as well as other twinned particles observed.

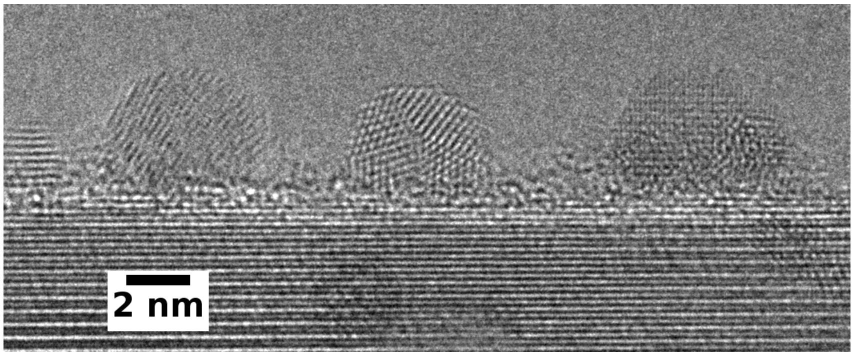

Figure 8.10. HREM image of palladium nanoparticles on STO (001) surface. Note several decahedra as well as other twinned particles observed.

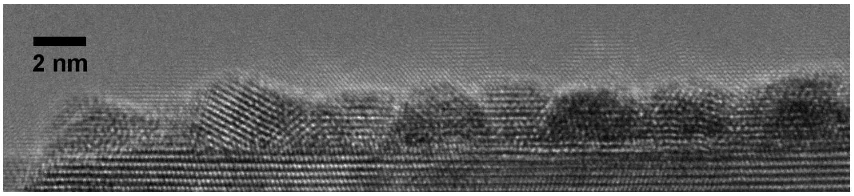

Figure 8.11. HREM image of platinum nanoparticles on STO (110) surface. Note that the majority of the particles are single crystals.

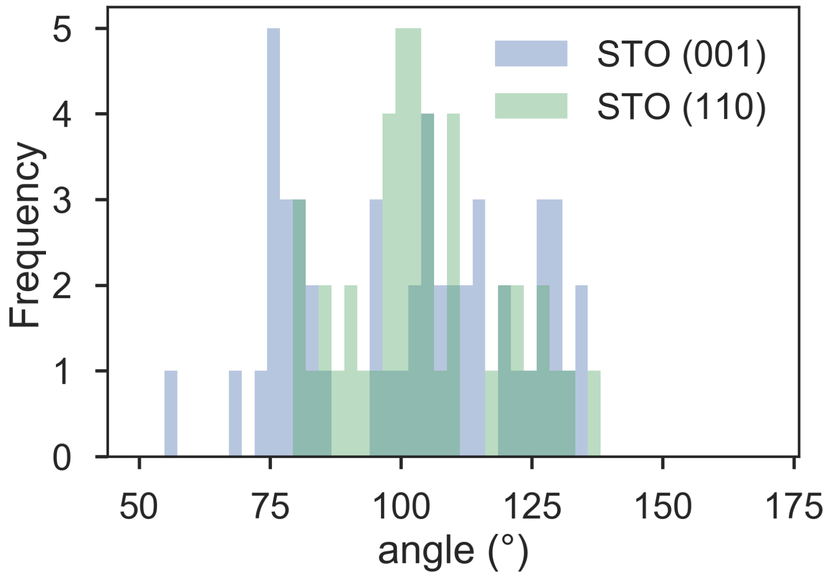

Figure 8.12. Histogram showing the distribution in contact angles measured for platinum nanoparticles after deposition on STO supports. Note that there is a support-dependence effect, splitting the dataset into two shows that the there is maximum around 75° for the (001) STO, and at 100° for (110) STO.

8.4 Discussion

8.4.1 Effect of ALD precursor

An initial hypothesis regarding the stark difference in population statistics was that the ligands from the precursor used for the palladium ALD remained adsorbed to the STO surface, and in some manner influenced the growth. Previous work done in collaboration with Dr. Bor-Rong Chen found that these ligands bind more strongly to SrO-terminated STO nanocuboids than TiO_2-terminated ones (see reference [155]). To test this, we can compare the results for palladium deposited onto STO using a different method. The wet impregnation method does not use organic ligands, and thus the ligands leftover from the ALD process can be ruled out as the cause of twin formation.

A total of ten particles were able to be identifed as either single crystals or twinned, of which five could measured to determine the contact angle. Figure 8.13 shows the histogram for contact angles and for both ALD and wet impregnation. There are no statistically significant differences between the contact angles, and while the number of particles counted is low relative to the number of particles counted for the ALD technique, 100 % of the particles observed were either MTPs or lamellar twinned particles.

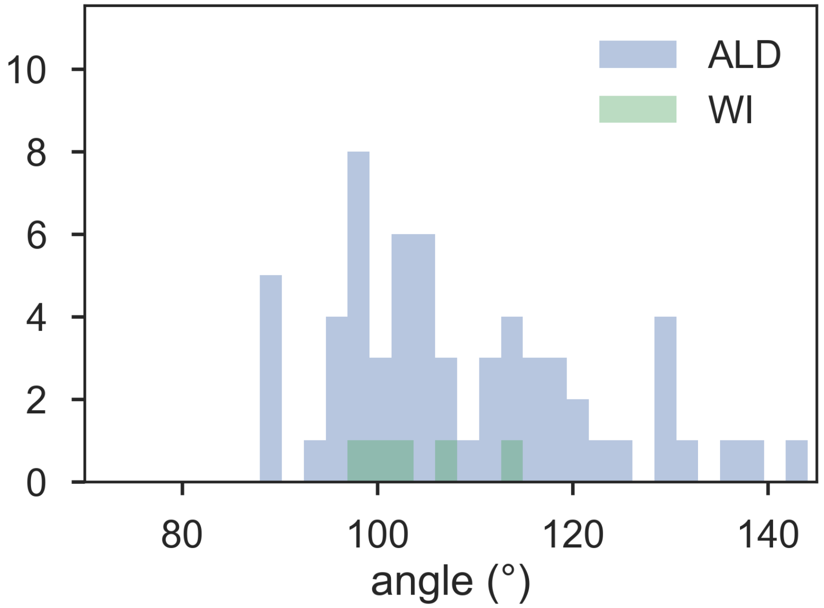

Figure 8.13. Histogram showing the distribution in contact angles measured for palladium nanoparticles separated by deposition technique. Note that while the number of counts for the wet impregnation (label WI), is low, 100% of the particles observed were either MTPs or lamellar twinned particles.

8.4.2 Support effect

For palladium, studies using single crystal supports of STO have shown preference for single crystals, although the orientation can be changed through control of the surface reconstructions present in the substrate.[156,157] Additionally, the growth conditions were not the same as our conditions. Changing the STO support in our case did not have a significant effect on the population of single crystals. The (001) faceted STO had 22% single crystals, while the (110) had 26% single crystals. Both of these numbers are lower than expected based solely upon the lattice mismatch, which is smaller in magnitude for the palladium-STO system compared to the platinum-STO system. It is possible that there is a lattice contraction at these particle sizes which destabilizes these particles on STO; a more careful analysis would be required to confirm this.

For the platinum case, there is a significant difference in the contact angle as a function of the support effect. However, in this case, the majority of the particles are single crystals, which should be modeled using the Winterbottom construction. This has already been done for platinum on STO nanocuboids, see reference [154]. There is literature which reports twinning in platinum as well,[158–160] so there is no intrinsic reason why platinum should exhibit such a marked decrease in twinned particles relative to palladium.

8.5 Conclusions and Future Work

Additional study is needed to determine the origin of the significant increase in the number of twinned particles for palladium. Since platinum is known to twin like other FCC metals, the first variable to control for would be the substrate material. Additional imaging experiments on the platinum-titania samples using high-resolution HAADF imaging should enable identification of single crystals and MTPs in these samples. Future work could also investigate the effect of additional supports, such as lanthanide scandates, which have markedly different electronic structure and chemical environments compared to STO and titania. While elucidating the effects of the twinning on catalysis would be interesting, it would likely be extremely challenging to deconvolve other effects such as the metal-support interaction and changes in the electronic structure. If the selectivity towards twinned particles or single crystals could be controlled, then it would merit additional attention to determine whether there is a large impact on materials properties for catalysis applications.

CHAPTER 9

Catalysis on oxide supports

9.1 Introduction

Much work has been done to study catalysis using supported noble metals. Controlling the faceting of the support material is important because support facets can control the catalyst particle shape, stabilize the catalysts from deactivation due to sintering over time, and introduce new perimeter sites at the interface between the catalyst and support. All of these factors can dramatically impact catalytic performance. Additionally, a plethora of effects can play significant roles during reactions, including exposed crystallographic planes,[161] charge transfer between the catalyst and support,[162,163] the participation of support oxygen in the reaction[164–166] and migration of support atoms[167,168] through the SMSI effect. To enable the deconvolution of these effects, it is useful to leverage knowledge gained from surface science studies of large, flat single crystals.[169–175] However, the surface area of such samples is too low to allow for catalytic testing in reactor studies. The resulting "materials gap," brought about by the lack of applicability of the single crystal to industrially relevant catalysts, is a known problem.[176–180]

Building on previous work by Drs. James Enterkin, Yuyuan Lin, and Chuandao Wang, I have leveraged shape-controlled particles to address this gap. The gravimetric surface areas are high enough to allow reactor studies, while simultaneously enabling use of the knowledge gained from studies of single crystal surfaces. These studies include work done using platinum[53,181–185] and palladium[156,157,186,187] deposited on STO single crystals. The synthesis and characterization of these supports has been described previously (see references [79, 80, 188] and Chapter 4).

This chapter describes work using platinum supported by STO polyhedra, with a control support material of anatase titania purchased from a commercial vendor. The reason for this choice is to compare a titania-rich surface termination with a titania material that is not shape-controlled. In particular, platinum-catalyzed CO oxidation on {110}-faceted STO and acrolein hydrogenation on {100}-faceted STO nanocuboids are the primary foci.

9.1.1 CO Oxidation

There are many economically relevant chemical processes, almost all of which rely upon catalysts. Among these is CO oxidation, which is important for emissions control devices in internal combustion engines. There is significant interest in improving efficiencies at low temperature,[181,189–196] primarily because the majority of pollutants are emitted before the catalytic converter has had time to warm up. Additionally, increased stability of the catalyst as a function of time is another desired trait, to reduce cost of replacement due to catalyst deactivation. These two parameters were investigated through temperature and time studies of CO oxidation of platinum catalysts supported by both STO and anatase titania. Comparing these two materials is relevant given that the surface termination of the STO nanocrystals is TiO_2-rich (see Chapter 4 and Chapter 7), and anatase TiO_2 is a standard reducible oxide support that is commercially available.

9.1.2 Strong Metal Support Interaction via ALD

Additional reactor studies using {100} faceted STO nanocuboids were carried out by collaborator Dr. Robert Kennedy . The primary goal was to study the effect of ALD overcoats on the selectivity for acrolein hydrogenation. The introduction of chemically different reactive sites via oxide overcoats (either titania or alumina) should result in selectivity towards one of these products over the other. My role in this work was to perform experiments to determine the overcoat thickness.

9.2 Experimental Methods

9.2.1 Preparation of catalyst samples

STO nanocuboid catalyst supports were synthesized following the method previously published by Rabufetti *et. al.*[80] STO dodecahedra supports were synthesized as described in Chapter 4. Anatase titania supports were purchased from Sigma Aldrich. Catalyst samples for CO oxidation were prepared by depositing platinum via ALD onto STO nanocuboids, STO dodecahedra, and anatase titania. The platinum ALD was carried out under conditions reported in Chapter 8. In this case, 1 and 3 cycles of platinum deposition were carried out.

For samples used to study SMSI, 5 cycles of platinum ALD were deposited onto STO nanocuboids. Further ALD was performed to deposit titania and alumina overcoats. For titania, titanium tetraisopropoxide (TTIP) and deionized water were dosed at 200 °C for 120 s, followed by a 120 s nitrogen purge. A total of 10 cycles of titania was overcoated onto the platinized STO nanocuboids. For alumina, trimethyl aluminum (TMA) and deionized water were dosed at 200 °C for 120 s, followed by a 120 s nitrogen purge. A total of 5 cycles of alumina was overcoated onto the platinized STO nanocuboids.

9.2.2 Characterization

Electron microscopy was carried out using several microscopes. A JEOL 2100F was used for conventional HREM imaging. A Hitachi HD-2300 equipped with a secondary electron detector was used for both secondary electron and HAADF imaging. A probe-corrected JEOL 200CF was used in STEM mode to obtain atomic resolution HAADF images and high resolution EDS scans. All microscopes were operated at 200 kV.

Adsorption isotherms were measured using a Micromeritics 3Flex instruments to determine the gravimetric surface areas via BET analysis for each sample.

Inductively coupled plasma optical emission Spectroscopy (ICP-OES) was used to measure the catalyst mass loadings using a Thermo iCAP 7600 ICP-OES instrument. Oxygen was assumed to be stoichiometric to calculate the relative mass loadings, as ICP-OES is not sensitive to oxygen.

Diffuse reflectance infrared Fourier transform spectroscopy (DRIFTS) characterization was performed using a Nicolet 6700 equipped with a Praying Mantis diffuse reflectance cell and sample chamber with heating stage and temperature controller. All samples were pre-reduced under flowing H_2 in-situ for 2 h at 250 °C.

XPS measurements were carried out by Christopher Mizzi using a Thermo Scientific ESCALAB 250Xi using a monochromatic Al Kα (1486.6 eV) X-ray source. Survey scans, as well as scans of the relevant Sr, Ti, Pt, and O binding energies, were acquired for all samples in the same run.

9.2.3 Catalytic testing

9.2.3.1 CO Oxidation

CO oxidation experiments were carried out using an Altimara BenchCAT 4000 microreactor. Samples were diluted with between 600 and 1200 mg silicon dioxide sand and loaded into a 1/400 silica tube with a glass wool catalyst bed. The temperatures were set to 80 °C, 100 °C and 120 °C and flow rates were varied from 15 sscm to 100 sscm.

Reaction products were analyzed using an Agilent gas chromatograph (GC) equipped with a temperature conductivity detector (TCD). The reactant gas stream consisted of 0.5 mol% CO and 20 mol% O_2 balanced with helium. The GC column separation resulted in an absence of CO_2 detected by the TCD, so conversion was calculated by monitoring the amounts of O_2 and CO. The platinum catalyst weight W was calculated from the measured catalyst placed into the reactor tube and the weight fraction from the ICP-OES mass loadings:

$$W = \frac{f_{\mathrm{Pt}} m_{\mathrm{total}}}{M_{\mathrm{pt}}}, \tag{9.1}$$

where W is the catalyst weight, f_{Pt} is the weight fraction of platinum from ICP, m_{total} is the total catalyst mass loaded into the reactor, and M_{Pt} is the molecular weight of platinum (195.05 g/mol). W will have units of mol of platinum. At constant temperature and pressure, the flow F can be calulated by combining the ideal gas law:

$$PV = nRT \tag{9.2}$$

with the equation:

$$F = J = \frac{\partial n}{\partial t} = \frac{P}{RT}\frac{\partial V}{\partial t} \approx \frac{P}{RT}\frac{\Delta V}{\Delta t}, \tag{9.3}$$

where P is pressure, R is the gas constant, T is temperature in Kelvin, t is time, n is the number of moles, V is volume. F will have units of mol/s of the reagent gases. Conversion is defined as as the fraction of products to reagents after leaving the reactor:

$$\text{Conversion} = \frac{F^0_{\mathrm{CO}} - F_{\mathrm{CO}}}{F^0_{\mathrm{CO}}} \tag{9.4}$$

where F_{CO}^{0} is the flow of CO at zero conversion, and F_{CO} is the flow of CO at the reaction conditions. The zero conversion area F_{CO} was determined by measuring the flow through a tube filled with silica sand at room temperature.

9.2.3.2 Acrolein Hydrogenation

Collaborator Dr. Robert Kennedy carried out all catalytic testing of acrolein hydrogenation. The details can be found in his PhD dissertation, see reference [197] (also in a submitted manuscript).

9.3 Results

The platinum ALD on STO dodecahedra resulted in well-dispersed particles with average sizes of 1.38 nm and 2.94 nm for 1 and 3 ALD cycles, respectively. The BET surface areas were 10 m^2/g before deposition, which increased to 12.9 m^2/g and 14 m^2/g, for the 1 cycle and 3 cycle samples. The mass loadings measured by ICP for these samples were 1 wt% and 3 wt%, respectively. Images showing the particles and their size distributions appear in Figure 9.1.

The anatase titania supports had significantly higher surface areas, with BET analysis showing 85 m^2/g. The mass loadings from ICP were 0.2 and 2 wt% for 1 and 3 ALD cycles, respectively. The BET surface areas for these samples 100 m^2/g and 105 m^2/g. The average platinum particle size was $\sim$ 1 nm for 1 ALD cycle and 1.38 nm for 3 ALD cycles.

Samples for acrolein hydrogenation had an average platinum particle size of 2 nm and mass loadings of 4 wt% platinum prior to oxide overcoat deposition. The mass loadings of the overcoats were 2.7 wt% for alumina and 3.8 wt% for titania.

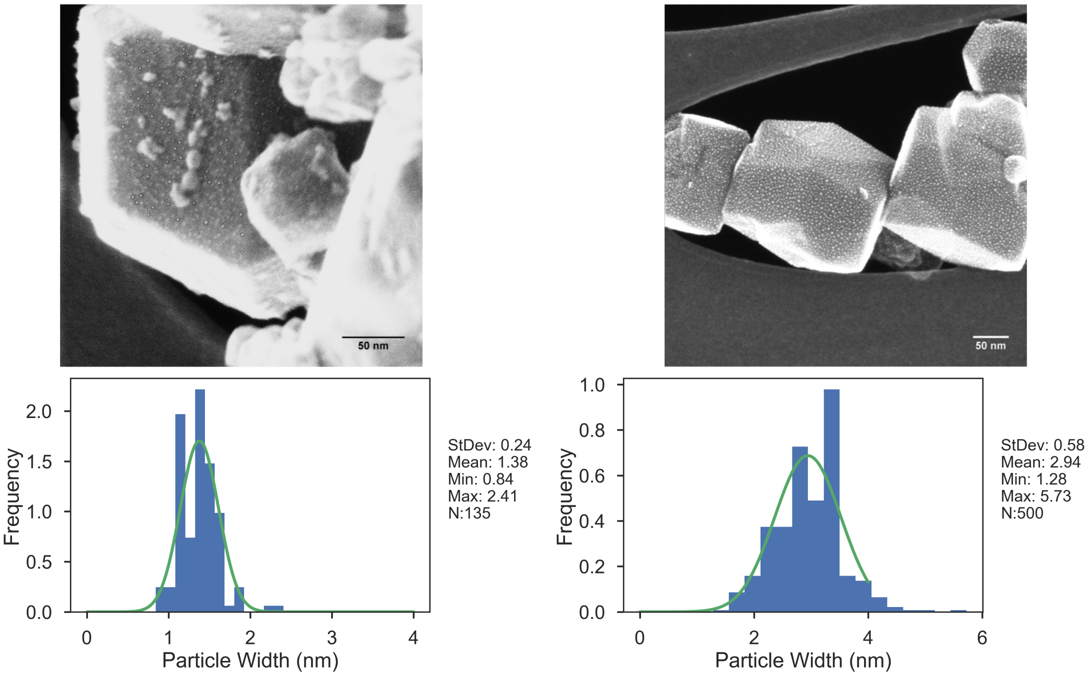

Figure 9.1. Secondary electron images and particle size distributions for (left) 1 platinum ALD and (right) 3 ALD cycles.

9.3.1 Selectivity through ALD SMSI

Figure 9.2 shows reaction data demonstrating the observed selectivity towards allyl alcohol for the titania overcoated samples, when compared with the bare platinum–STO and alumina overcoated samples.

The overcoat thickness, as determined from HREM imaging, was on the order of 6 Å for the alumina sample and 5 Å for the titania case (see Figure 9.3). EDS line scans (see Figure 9.4) confirmed these observations, which show that the alumina overcoat blocked the perimeter sites of platinum supported on STO nanocuboids.

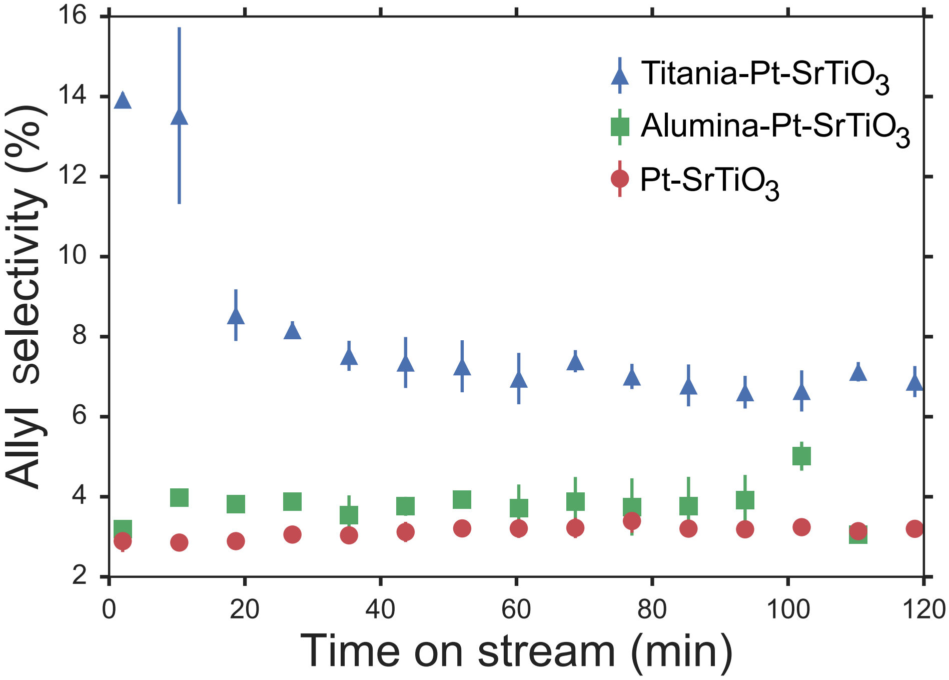

Figure 9.2. Plot of catalytic conversion versus time on stream showing increased selectivity towards allyl alcohol for titania overcoated Pt-STO samples, compared with the bare Pt-STO and alumina-Pt-STO samples.

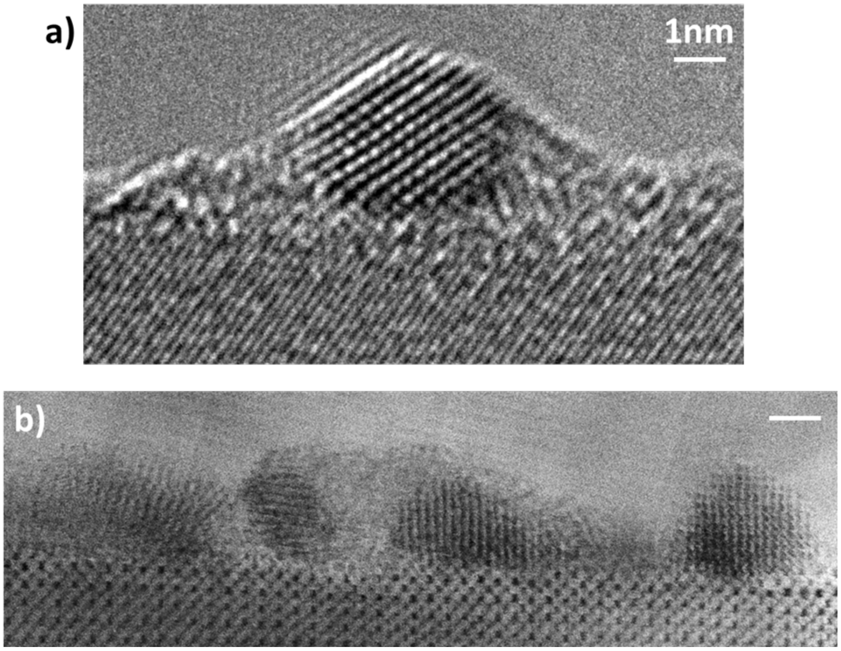

Figure 9.3. HREM images of ALD overcoats of (a) alumina and (b) titania. The overcoats are visible as a disordered film at the perimeter of the platinum nanoparticle in (a) and also over the top of the platinum nanoparticle in (b). Note that the scale bar applies to both images.

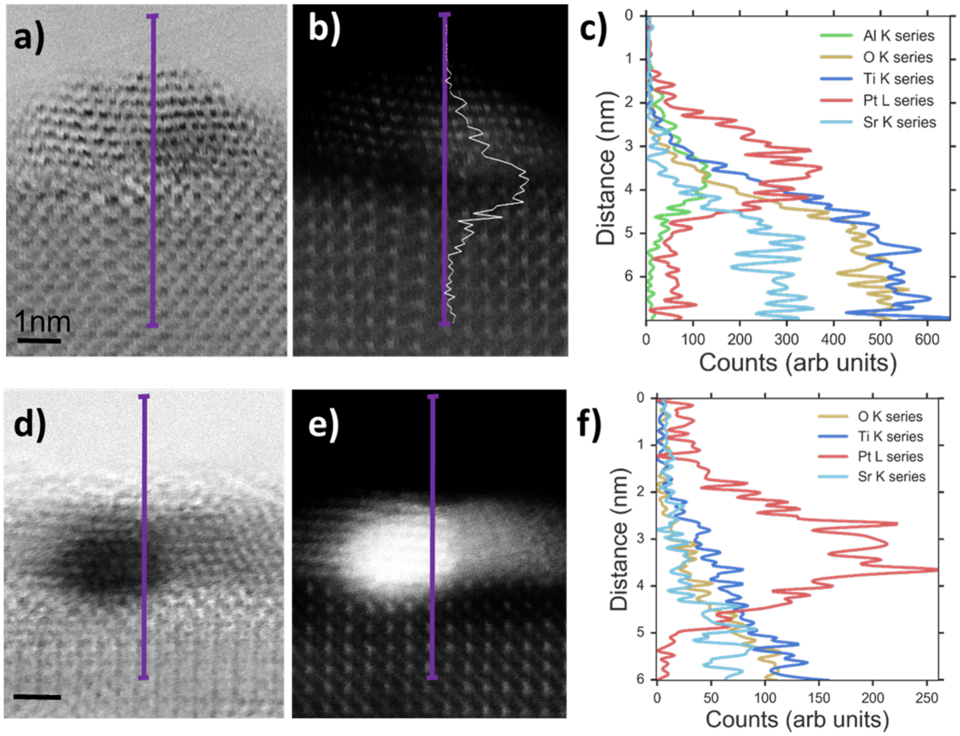

Figure 9.4. Combined BF/HAADF/EDS of $Al_2O_3/Pt/SrTiO_3$ (a-c) and $TiO_2/Pt/SrTiO_3$ (d-f). The bright-field (a, d) and HAADF (b, e) images show platinum on the (001) of STO. An amorphous oxide film can be seen at the sides of the platinum nanoparticles in (a) and also on top in (d). The EDS line scan path is shown in purple. EDS of alumina overcoated sample (c) indicates that the alumina overcoat is concentrated at the platinum–STO interface (see also white trace in (b)). The titania overcoat (f) could not be distinguished by EDS from titania signal contributed by the support.

9.3.2 Comparison of STO dodecahedra to anatase titania supports

Initial results indicate that the samples with platinum deposited on dodecahedra are more active than those deposited on titania.

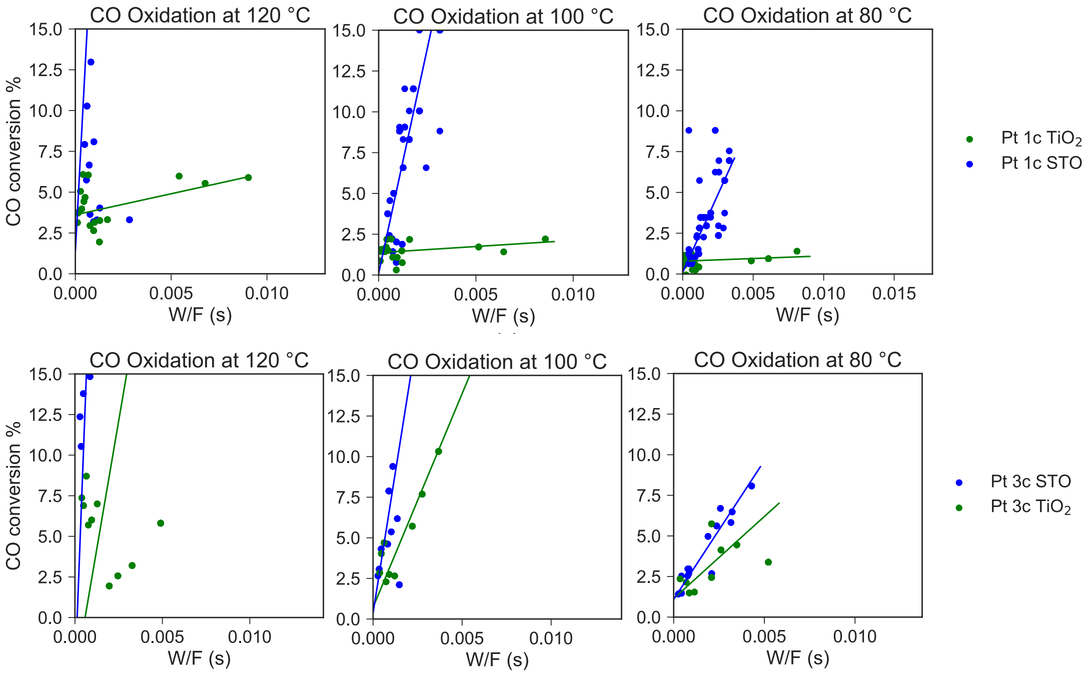

Figure 9.5. Conversion versus residence time for platinum deposited on titania and STO dodecahedra. The top row shows the samples with 1 Pt ALD cycle, while the bottom row shows 3 Pt ALD cycles deposited onto the supports as labeled.

Figure 9.5 shows the CO conversion versus the residence time of CO in the catalyst bed. The turnover number (TON), which is defined as the initial catalytic reaction rate approaching zero conversion, was calculated by fitting a linear regression to the data points. The fitting was performed using an implemenation of the robust linear modeling with a HuberT estimator as implemented in the statsmodels Python package. The use of robust fitting instead of ordinary least squares is to reduce the impact of outliers in the data. The results of the fitting appear in Table 9.1.

Table 9.1. Calculated gravimetric TOF, in units of s^{-1} normalized by total platinum platinum mass for platinum deposited on STO dodecahedra and anatase titania supports. Note that the Pt-STO samples had between 10 to 85 times higher turnover rates than the Pt-TiO_2 samples.

T (°C)	Pt 1c STO	Pt 1c TiO_2	Pt 3c STO	Pt 3c TiO_2
80	$(2.2 \pm 0.8) \times 10^{-1}$	$(2.6 \pm 0.9) \times 10^{-3}$	$(2.8 \pm 0.2) \times 10^{-1}$	$(0.6 \pm 0.2) \times 10^{-1}$
100	$(5.5 \pm 0.5) \times 10^{-2}$	$(0.8 \pm 0.5) \times 10^{-3}$	$(6.9 \pm 0.4) \times 10^{-2}$	$(2.6 \pm 0.1) \times 10^{-2}$
120	$(1.9 \pm 0.2) \times 10^{-2}$	$(0.3 \pm 0.4) \times 10^{-3}$	$(1.7 \pm 0.1) \times 10^{-2}$	$(1.0 \pm 0.3) \times 10^{-2}$

9.4 Conclusions

From the initial results, platinum supported on shape-controlled STO shows increased activity for CO oxidation compared to anatase titania. Work is currently ongoing to determine the number of exposed platinum atoms such that the turnover frequency (TOF) can be calculated for direct comparison with other catalysts. Work is also ongoing to determine the origin of the unexpected CO chemisorption behavior and whether it is materials-dependent. Future work to determine the origin of the differences in bonding character and electronic structure of the platinum-oxide interface will be informative not only for CO oxidation, but other reactions where selectivity towards a certain product is desired.

Additionally, the success of the ALD-generated SMSI effect in the STO nanocuboids overcoated with different oxide materials can be attributed to the creation of different platinum-oxide interfaces, and the blockage of active sites that favor the carbonyl product. Further work to explore more reactions and materials systems with shape-controlled synthesis can expand the engineering toolbox of catalytic systems, for both selective and rate-efficient catalysis.

CHAPTER 10

Ongoing Projects and Future Work

10.1 Determination of support effect in twinning of Pt and Pd

Work is ongoing to determine whether there is a support effect on twinning in platinum. Anatase titania (*I 41/amd*, space group 141), which has lattice parameters of $a = b = 3.804\,\text{Å}$, and $c = 9.614\,\text{Å}$, should have a larger interfacial energy due to strain. Inital attempts to image platinum deposited on titania (see HREM image in Figure 10.1) which shows several particles less than 1 nm in size, which make this task difficult. HAADF imaging would help this process since there is a large atomic number difference between platinum and titanium (78 vs 22).

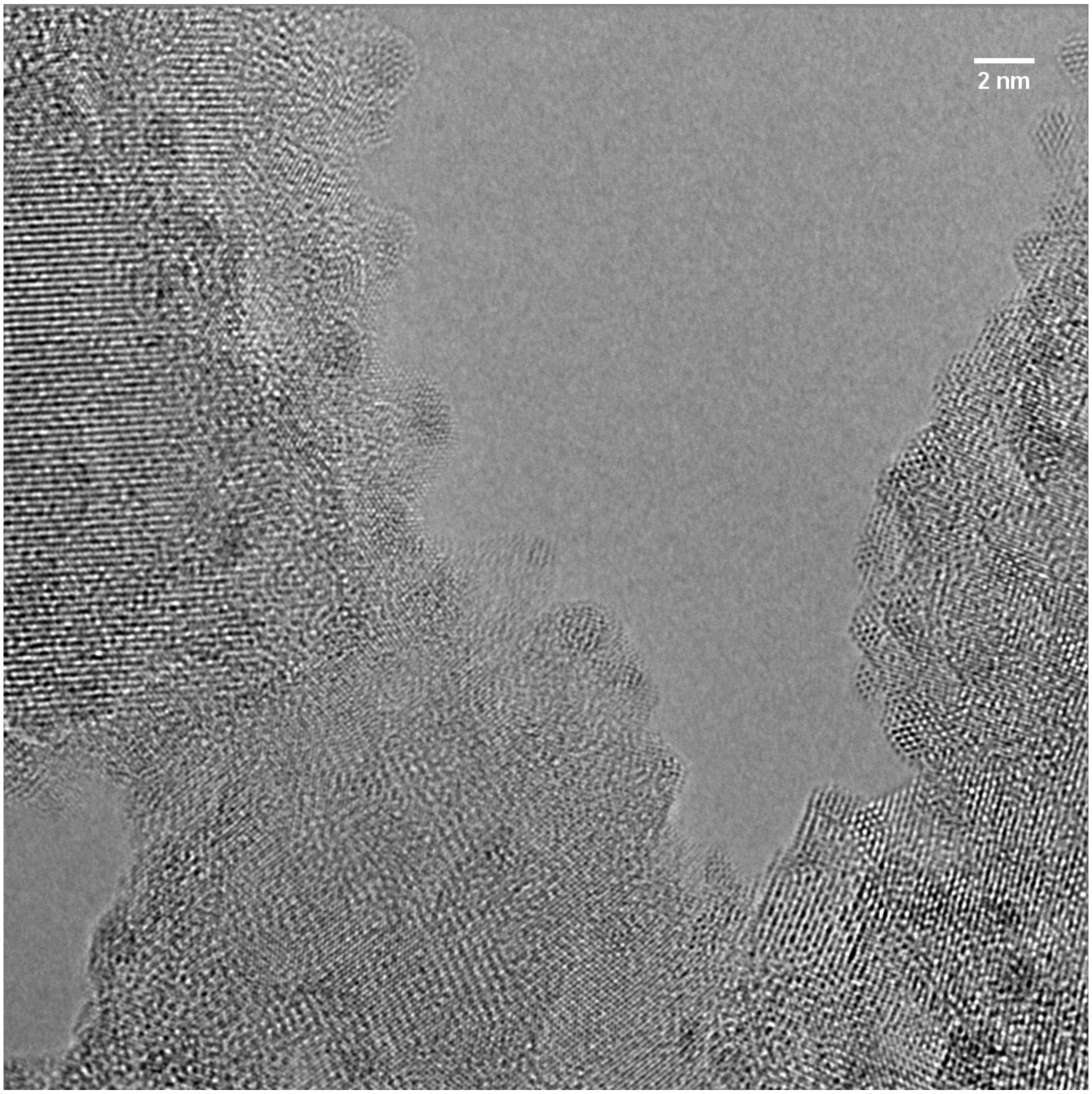

Figure 10.1. HREM image of 3 wt% platinum deposited on anatase titania. Note the low contrast which is because of the very small platinum particle size.

10.2 Characterization of Catalysis Samples

10.2.1 Initial XPS Results

Work is ongoing to further characterize the chemical state of the platinum-titania and platinum-STO catalyst samples discussed in Chapter 9 with XPS. XPS data obtained for the different samples show subtle differences in bonding character. Figures 10.2-10.5 show the platinum 4d and 4f states. The 4d peaks are best fit with three doublets, while the 4f states were best fit with two doublets. The signal to noise ratio is significantly worse for the titania samples in both cases, likely because of the lower platinum loading. Despite this, one can see a more peak splitting in the 4d and 4f in both the platinum-TiO_2 samples. This is likely due to differences in the platinum-STO interface compared with the platinum-TiO_2 interface. While nominally TiO_2-rich, it will be structurally different compared to anatase titania.

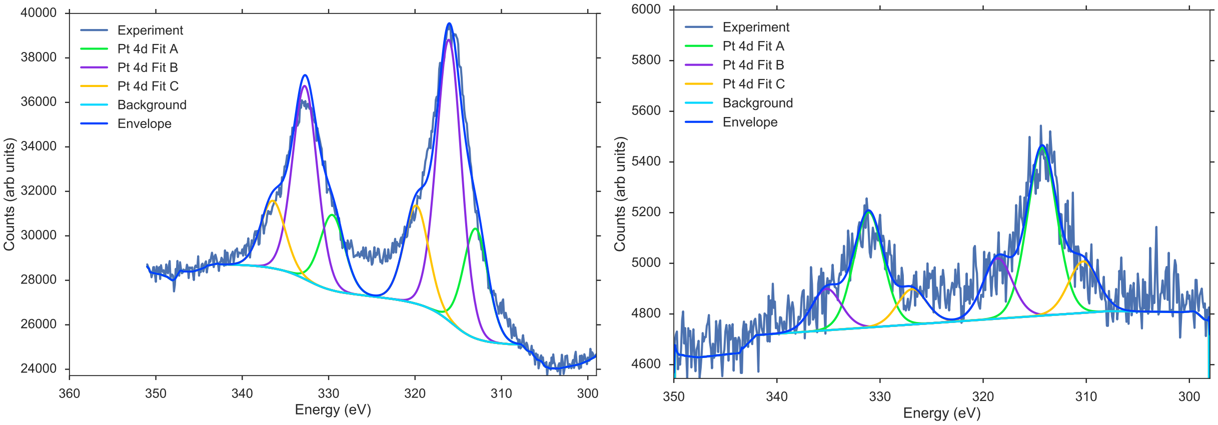

Figure 10.2. XPS scans of the Pt 4d states for the 1 ALD cycle on both STO dodecahedra (left) and anatase titania (right). Note the increase in peak area at higher binding energies for the STO case.

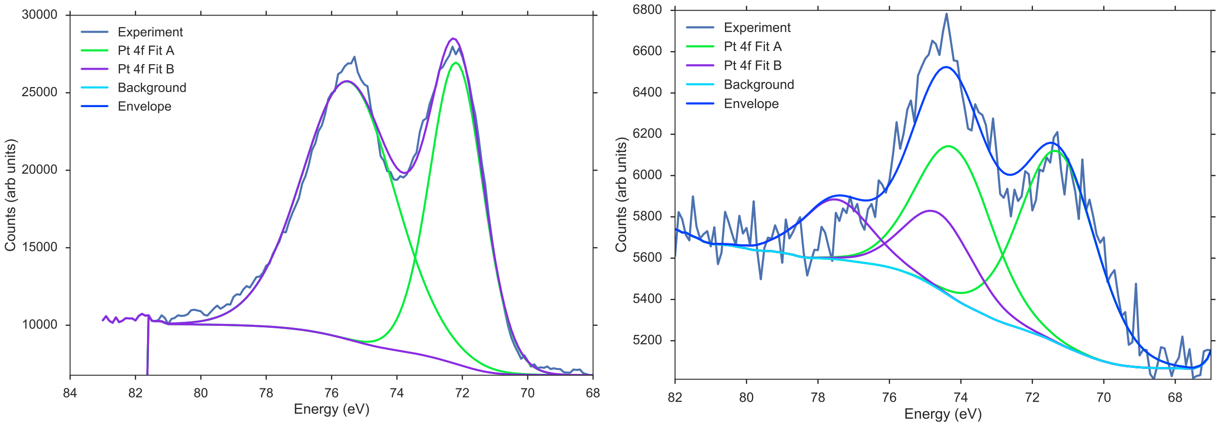

Figure 10.3. XPS scans of the Pt 4f states for the 1 ALD cycle on both STO dodecahedra (left) and anatase titania (right). Note the peak splitting present in titania sample and absent in the STO sample.

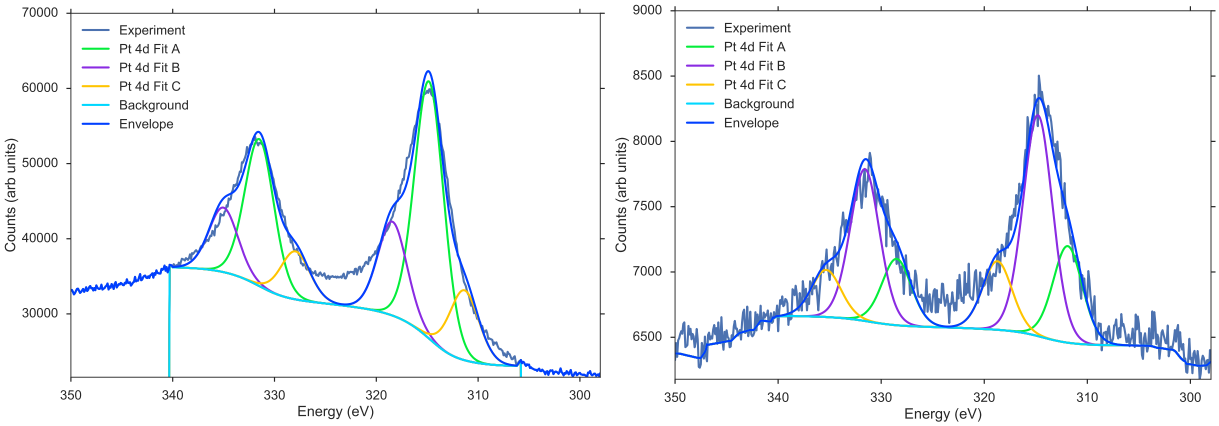

Figure 10.4. XPS scans of the Pt 4d states for the 3 ALD cycle on both STO dodecahedra (left) and anatase titania (right). Note the increase in peak area at higher binding energies for the STO case.

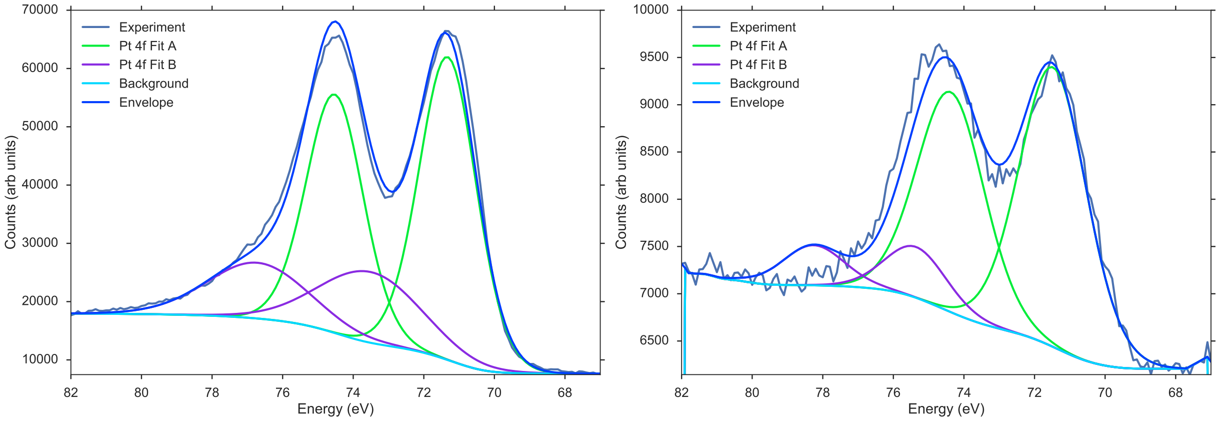

Figure 10.5. XPS scans of the Pt 4f states for the 3 ALD cycle on both STO dodecahedra (left) and anatase titania (right).

10.2.2 DRIFT Results

DRIFTS spectra were acquired for the samples using the protocol described above. The platinum on STO samples, in particular, exhibited unexpected behavior. After dosing CO gas, a strong absorbance peak appeared at around 2091 cm^{-1}, which is attributed to linear CO. This peak remains even after 15 min dosing under Ar. Upon introduction of O_2 gas, the peak red-shifts to 2076 cm^{-1} and decreases markedly. Both of these wavenumbers are associated with linear CO. Also note that there is a broad band around 1800 cm^{-1}, associated with bridging-type CO, which also decreases upon oxidation.

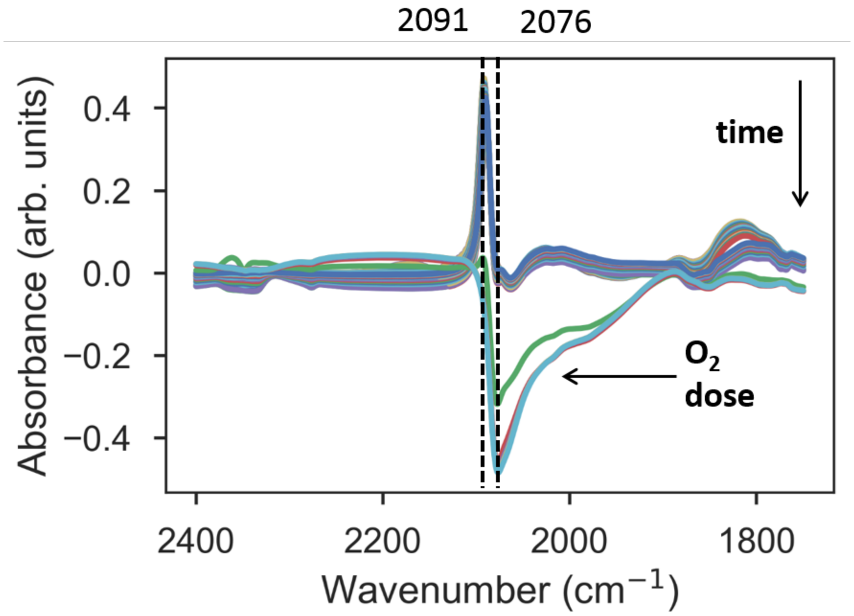

Figure 10.6. DRIFTS data for Pt 3c on STO dodecahedra after exposure of sample to CO. The large change in intensity at 2091 cm^{-1} occured after introducing oxygen into the chamber. Comparable results were obtained for the 1c sample.

By way of comparison, the Pt 3c titania sample exhibits significantly different behavior under the same experimental conditions. The CO chemisorption behavior resulted in two distinct peaks associated with linear CO near 2100 cm^{-1}. These peaks decay prior to introducing oxygen, and are dominated by a broad background after oxygen is introduced.

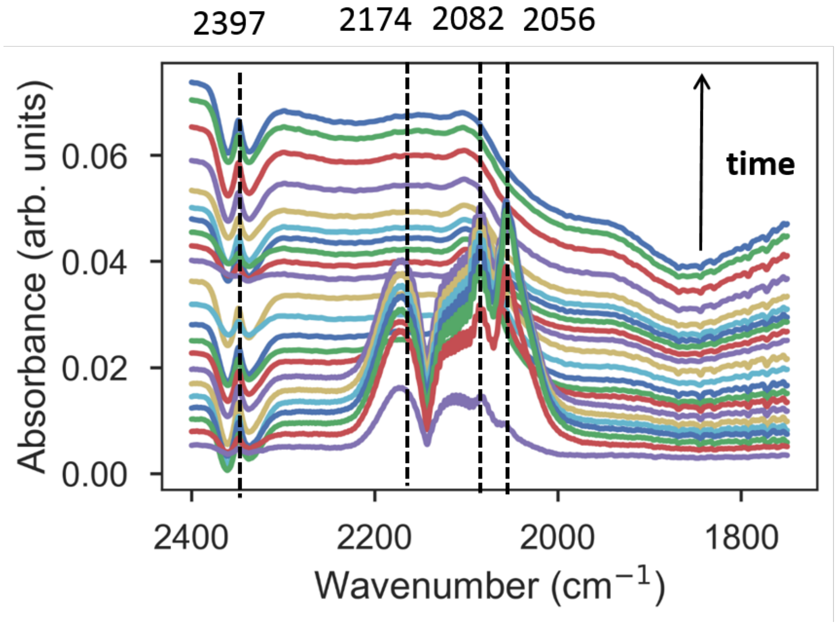

Figure 10.7. DRIFTS data for Pt 3c on anatase titania. Note that the peaks identified at 2397 cm^{-1}, 2174 cm^{-1}, 2082 cm^{-1}, and 2056 cm^{-1} correspond to CO_2, gas phase CO and linear CO. The intensity for the peaks in this case becomes dominated by background signal after introduction of oxygen into the chamber.

10.3 Proposed Future Work

Based upon the DRIFTS results and ongoing work in collaboration with Dr. Xin Tang, there is evidence to suggest that the disappearance and negative absorbance of the CO peak upon oxidation is due to CO present in the background spectrum prior to absorbance measurements. This peak does not appear until after H_2 reduction of the sample. One possible source of the CO is chemisorbed CO_2 from the atmosphere, which can react with hydrogen via the reverse water gas shift reaction:

$$CO_2 + H_2 \rightleftharpoons CO + H_2O \tag{10.1}$$

This reaction has a positive free energy change of 28.55 kJ/mol[198,199] at ambient conditions. Future work to determine whether this reaction is occurring would be a temperature controlled reduction (TPR) and/or temperature controlled oxidation (TPO) study. The CleanCat facility is equipped with an instrument capabable of this experiment, and additionally, there is the capability to analyze the output from the gas stream with a mass spectrometer. Furthermore, experiments to study the electronic structure, such as EELS and X-ray absorbance spectroscopy (XAS), along with further vibrational spectroscopy, will shed light on the mechanism behind this observation.

10.4 Conclusions

Overall, the surfaces of STO and BTO were found to be TiO_2 rich when synthesized with hydrothermal methods. It is possible to obtain the A-site termination through use of surfactants; however, it is challenging to reproducibly obtain the correct conditions to form liquid crystal phases which result in low-index faceting of nanoparticles grown therein. Additionally, catalytic results indicate that the {110}-faceted STO dodecahedra have higher catalytic activity than nanoparticles of anatase TiO_2 purchased from a commercial vendor. These serve as confirmation that surfaces play an important role in a host of chemical and electronic processes.

Appendix A

A.1 Thermochemical Data used for Dissolution Enthalpy Calculations in Chapter 7

Table A.1. Referenced standard enthalpies of formation for species involved in STO surface chemistry. Note that these values are used in thermodynamic analysis in Chapter 7 Section 7.4.4 (see Table 7.2 for calculated dissolution enthalpies).

Reagent	ΔH_f^o kJ/mol	ΔH_f^o eV/1×1	Ref
$SrTiO_3$ (s)	-1672.40	-17.33	Lencka and Riman [102]
SrO (s)	-592.04	-6.14	Lencka and Riman [102]
Sr^{2+} (aq)	-550.91	-5.71	Lencka and Riman [102]
TiO_2 (s)	-946.01	-9.80	Lencka and Riman [105]
Ti^{4+} (aq)	-215.61	-2.23	Lencka and Riman [105]
H_2O (aq)	-285.83	-2.96	Lencka and Riman [105]
OH^- (aq)	-230.03	-2.38	Lencka and Riman [105]
$Sr(OH)_2$ (aq)	-1011.60	-10.48	Lencka and Riman [102]
$Ti(OH)_4$ (aq)	-1511.30	-15.66	Lencka and Riman [105]
$Sr(OH)_2 \cdot 8\,H_2O$ (s)	-3360.60	-34.83	Lencka and Riman [102]

A.2 Structure Files used for Simulations

Listing A.1. RT13 BTO

```
data_blebleble
_symmetry_cell_setting          tetragonal
_symmetry_space_group_name_H-M      ’P2/m’
_symmetry_space_group_name_Hall      ’-P 2’
_symmetry_Int_Tables_number      10
loop_
   _symmetry_equiv_pos_as_xyz
```

```
    x,y,z
    -x,-y,-z
    -x,-y,z
    x,y,-z
_cell_length_a         14.466783
_cell_length_b         14.466783
_cell_length_c         28.303229
_cell_angle_alpha      90.000000
_cell_angle_beta       90.000000
_cell_angle_gamma      90.000000
loop_
  _atom_site_label
  _atom_site_fract_x
  _atom_site_fract_y
  _atom_site_fract_z
  _atom_site_U_iso_or_equiv
  _atom_site_occupancy
  _atom_site_type_symbol
    O1        0.958491    0.690717    0.206295   0.000   1.000  O
    O2        0.152063    0.722973    0.212341   0.000   1.000  O
    O3        0.198204    0.536514    0.209016   0.000   1.000  O
    O4        0.000000    0.500000    0.221626   0.000   1.000  O
```

O5	0.002098	0.806531	0.715201	0.000	1.000	O
O6	0.289464	0.627814	0.713726	0.000	1.000	O
O7	0.742793	0.842699	0.204252	0.000	1.000	O
O8	0.317354	0.981645	0.219101	0.000	1.000	O
O9	0.411030	0.395285	0.206883	0.000	1.000	O
O10	0.500000	0.000000	0.207354	0.000	1.000	O
O11	0.464452	0.193502	0.222298	0.000	1.000	O
O12	0.658593	0.221627	0.207963	0.000	1.000	O
O13	0.596117	0.401630	0.218647	0.000	1.000	O
O14	0.874589	0.089390	0.213212	0.000	1.000	O
O15	0.775609	0.650059	0.203722	0.000	1.000	O
O16	0.931518	0.907971	0.219418	0.000	1.000	O
O17	0.799147	0.955398	0.712376	0.000	1.000	O
O18	0.405003	0.892410	0.713973	0.000	1.000	O
O19	0.344921	0.267389	0.719613	0.000	1.000	O
O20	0.500000	0.500000	0.712910	0.000	1.000	O
O21	0.600960	0.911290	0.686218	0.000	1.000	O
O22	0.530351	0.292453	0.685733	0.000	1.000	O
O23	0.000000	0.000000	0.686067	0.000	1.000	O
O24	0.034063	0.813028	0.143193	0.000	1.000	O
O25	0.275863	0.648437	0.142416	0.000	1.000	O
O26	0.098158	0.438144	0.140376	0.000	1.000	O

O27	0.813804	0.970164	0.142728	0.000	1.000	O
O28	0.425863	0.883117	0.142050	0.000	1.000	O
O29	0.358762	0.263043	0.142077	0.000	1.000	O
O30	0.500000	0.500000	0.141394	0.000	1.000	O
O31	0.731810	0.848156	0.073046	0.000	1.000	O
O32	0.192068	0.537797	0.069460	0.000	1.000	O
O33	0.538370	0.808705	0.067555	0.000	1.000	O
O34	0.346995	0.768774	0.070966	0.000	1.000	O
O35	0.154064	0.731184	0.074298	0.000	1.000	O
O36	0.577638	0.615551	0.069705	0.000	1.000	O
O37	0.770382	0.654138	0.078470	0.000	1.000	O
O38	0.802764	0.961421	0.000000	0.000	1.000	O
O39	0.417124	0.887557	0.000000	0.000	1.000	O
O40	0.038829	0.802865	0.000000	0.000	1.000	O
O41	0.663688	0.729768	0.000000	0.000	1.000	O
O42	0.732531	0.343339	0.000000	0.000	1.000	O
O43	0.500000	0.500000	0.000000	0.000	1.000	O
O44	0.869855	0.589480	0.000000	0.000	1.000	O
O45	0.385766	0.576196	0.069679	0.000	1.000	O
O46	0.114203	0.922593	0.068340	0.000	1.000	O
O47	0.921675	0.885359	0.070170	0.000	1.000	O
O48	0.307021	0.960575	0.073330	0.000	1.000	O

O49	0.500000	0.000000	0.070102	0.000	1.000	O
O50	0.000000	0.500000	0.059023	0.000	1.000	O
O51	0.961342	0.690758	0.071782	0.000	1.000	O
Ti1	0.419609	0.881509	0.786977	0.000	1.000	Ti
Ti2	0.450535	0.200650	0.710960	0.000	1.000	Ti
Ti3	0.331728	0.997075	0.713289	0.000	1.000	Ti
Ti4	0.414174	0.607873	0.713873	0.000	1.000	Ti
Ti5	0.929250	0.908836	0.713829	0.000	1.000	Ti
Ti6	0.887069	0.575808	0.931661	0.000	1.000	Ti
Ti7	0.729366	0.345173	0.072545	0.000	1.000	Ti
Ti8	0.655707	0.729380	0.072538	0.000	1.000	Ti
Ti9	0.037406	0.810750	0.072197	0.000	1.000	Ti
Ti10	0.424925	0.883804	0.070835	0.000	1.000	Ti
Ti11	0.804269	0.963635	0.069926	0.000	1.000	Ti
Ti12	0.500000	0.500000	0.069144	0.000	1.000	Ti
Ti13	0.667930	0.714585	0.786930	0.000	1.000	Ti
Ti14	0.259295	0.647061	0.219055	0.000	1.000	Ti
Ti15	0.103473	0.422356	0.205960	0.000	1.000	Ti
Ti16	0.050449	0.805568	0.218192	0.000	1.000	Ti
Ti17	0.803365	0.956310	0.208665	0.000	1.000	Ti
Ti18	0.500000	0.500000	0.207873	0.000	1.000	Ti
Ba1	0.610486	0.919724	0.143600	0.000	1.000	Ba

```
Ba2     0.539429   0.305399   0.143585   0.000   1.000  Ba
Ba3     0.081161   0.621524   0.142106   0.000   1.000  Ba
Ba4     0.000000   0.000000   0.856798   0.000   1.000  Ba
Ba5     0.696943   0.535273   0.140392   0.000   1.000  Ba
Ba6     0.148641   0.232005   0.140891   0.000   1.000  Ba
Ba7     0.770375   0.160344   0.143343   0.000   1.000  Ba
Ba8     0.461396   0.693265   0.000000   0.000   1.000  Ba
Ba9     0.613867   0.921472   0.000000   0.000   1.000  Ba
Ba10    0.231436   0.843002   0.000000   0.000   1.000  Ba
Ba11    0.691900   0.536679   0.000000   0.000   1.000  Ba
Ba12    0.847066   0.772078   0.000000   0.000   1.000  Ba
Ba13    0.918348   0.378045   0.000000   0.000   1.000  Ba
Ba14    0.000000   0.000000   0.000000   0.000   1.000  Ba
```

Listing A.2. BaO BTO

```
data_Wien2k_Data
_cell_length_a       3.999799
_cell_length_b       4.017999
_cell_length_c      39.997985
_cell_angle_alpha   90.000000
_cell_angle_beta    90.000000
_cell_angle_gamma   90.000000
```

```
_cell_measurement_temperature 0.0
_diffrn_ambient_temperature 0.0
_symmetry_space_group_name_H-M         'Pmmm      '
_symmetry_space_group_number    47

_refine_date  '25- 9-2017'
_refine_method 'generated from Wien2k code'
_refine_special_details
;
Structure converted from Wien2k struct file, Version 9.1
File Name /home/crosby/BTO-BO/BTO-BO.struct
Title 'blebleble'
;

loop_
_symmetry_equiv_pos_as_xyz
   +x,+y,+z
   -x,-y,+z
   -x,+y,-z
   +x,-y,-z
   -x,-y,-z
   +x,+y,-z
   +x,-y,+z
   -x,+y,+z
loop_
_atom_site_label
_atom_site_type_symbol
_atom_site_fract_x
_atom_site_fract_y
_atom_site_fract_z
_atom_site_U_iso_or_equiv
Ba001   Ba   0.50000000   0.50000000   0.00000000   0.05000000
Ba002   Ba   0.50000000   0.50000000   0.10000001   0.05000000
Ba003   Ba   0.50000000   0.50000000   0.79999999   0.05000000
Ti004   Ti   0.00000000   0.00000000   0.05000001   0.05000000
Ti005   Ti   0.00000000   0.00000000   0.84999996   0.05000000
O0006   O    0.00000000   0.50000000   0.05000001   0.05000000
O0007   O    0.00000000   0.50000000   0.84999996   0.05000000
O0008   O    0.50000000   0.00000000   0.05000001   0.05000000
O0009   O    0.50000000   0.00000000   0.84999996   0.05000000
O0010   O    0.00000000   0.00000000   0.00000000   0.05000000
O0011   O    0.00000000   0.00000000   0.10000001   0.05000000
O0012   O    0.00000000   0.00000000   0.79999999   0.05000000
#End  data_Wien2k_Data
```

Listing A.3. TiO2 BTO

```
data_Wien2k_Data
_cell_length_a      3.999799
_cell_length_b      4.017999
_cell_length_c     39.997985
_cell_angle_alpha     90.000000
_cell_angle_beta      90.000000
_cell_angle_gamma     90.000000
_cell_measurement_temperature 0.0
_diffrn_ambient_temperature 0.0
_symmetry_space_group_name_H-M            'Pmmm     '
_symmetry_space_group_number    47

_refine_date  '25- 9-2017'
_refine_method 'generated from Wien2k code'
_refine_special_details
;
Structure converted from Wien2k struct file, Version 9.1
File Name /home/crosby/BTO-TiO2/BTO-TiO2.struct
Title 'blebleble'
;
```

```
loop_
_symmetry_equiv_pos_as_xyz
   +x,+y,+z
   −x,−y,+z
   −x,+y,−z
   +x,−y,−z
   −x,−y,−z
   +x,+y,−z
   +x,−y,+z
   −x,+y,+z
loop_
_atom_site_label
_atom_site_type_symbol
_atom_site_fract_x
_atom_site_fract_y
_atom_site_fract_z
_atom_site_U_iso_or_equiv
Ba001  Ba  0.00000000  0.00000000  0.00000000  0.05000000
Ba002  Ba  0.00000000  0.00000000  0.10000000  0.05000000
Ba003  Ba  0.00000000  0.00000000  0.79999998  0.05000000
Ti004  Ti  0.50000000  0.50000000  0.05000000  0.05000000
Ti005  Ti  0.50000000  0.50000000  0.24999999  0.05000000
```

```
Ti006  Ti  0.50000000  0.50000000  0.84999995  0.05000000
O0007  O   0.50000000  0.00000000  0.05000000  0.05000000
O0008  O   0.50000000  0.00000000  0.24999999  0.05000000
O0009  O   0.50000000  0.00000000  0.84999995  0.05000000
O0010  O   0.00000000  0.50000000  0.05000000  0.05000000
O0011  O   0.00000000  0.50000000  0.24999999  0.05000000
O0012  O   0.00000000  0.50000000  0.84999995  0.05000000
O0013  O   0.50000000  0.50000000  0.00000000  0.05000000
O0014  O   0.50000000  0.50000000  0.10000000  0.05000000
O0015  O   0.50000000  0.50000000  0.79999998  0.05000000
#End data_Wien2k_Data
```

Listing A.4. SrO STO

```
data_Wien2k_Data
_cell_length_a      3.904999
_cell_length_b      3.904999
_cell_length_c     39.049984
_cell_angle_alpha     90.000000
_cell_angle_beta      90.000000
_cell_angle_gamma     90.000000
_cell_measurement_temperature 0.0
_diffrn_ambient_temperature 0.0
```

```
_symmetry_space_group_name_H-M         'P4/mmm '
_symmetry_space_group_number  123

_refine_date  '25- 9-2017'
_refine_method  'generated from Wien2k code'
_refine_special_details
;
Structure converted from Wien2k struct file, Version 9.1
File Name /home/crosby/STO-SrO/STO-SrO.struct
Title 'blebleble'
;

loop_
_symmetry_equiv_pos_as_xyz
   +x,+y,+z
   -x,-y,+z
   -y,+x,+z
   +y,-x,+z
   -x,+y,-z
   +x,-y,-z
   +y,+x,-z
   -y,-x,-z
```

```
    -x,-y,-z
    +x,+y,-z
    +y,-x,-z
    -y,+x,-z
    +x,-y,+z
    -x,+y,+z
    -y,-x,+z
    +y,+x,+z
loop_
_atom_site_label
_atom_site_type_symbol
_atom_site_fract_x
_atom_site_fract_y
_atom_site_fract_z
_atom_site_U_iso_or_equiv
Sr001   Sr   0.50000000   0.50000000   0.00000000   0.05000000
Sr002   Sr   0.50000000   0.50000000   0.09999999   0.05000000
Sr003   Sr   0.50000000   0.50000000   0.80000001   0.05000000
Ti004   Ti   0.00000000   0.00000000   0.04999999   0.05000000
Ti005   Ti   0.00000000   0.00000000   0.85000004   0.05000000
O0006   O    0.00000000   0.00000000   0.00000000   0.05000000
O0007   O    0.00000000   0.00000000   0.09999999   0.05000000
```

```
O0008  O   0.00000000  0.00000000  0.80000001  0.05000000
O0009  O   0.50000000  0.00000000  0.04999999  0.05000000
O0010  O   0.50000000  0.00000000  0.14999999  0.05000000
#End data_Wien2k_Data
```

Listing A.5. TiO2 STO

```
data_Wien2k_Data
_cell_length_a      3.904999
_cell_length_b      3.904999
_cell_length_c     39.049984
_cell_angle_alpha    90.000000
_cell_angle_beta     90.000000
_cell_angle_gamma    90.000000
_cell_measurement_temperature 0.0
_diffrn_ambient_temperature 0.0
_symmetry_space_group_name_H-M          'P4/mmm '
_symmetry_space_group_number  123

_refine_date  '25- 9-2017'
_refine_method 'generated from Wien2k code'
_refine_special_details
;
```

```
Structure converted from Wien2k struct file, Version 9.1
File Name /home/crosby/STO-TiO2/STO-TiO2.struct
Title 'blebleble'
;

loop_
_symmetry_equiv_pos_as_xyz
   +x,+y,+z
   -x,-y,+z
   -y,+x,+z
   +y,-x,+z
   -x,+y,-z
   +x,-y,-z
   +y,+x,-z
   -y,-x,-z
   -x,-y,-z
   +x,+y,-z
   +y,-x,-z
   -y,+x,-z
   +x,-y,+z
   -x,+y,+z
   -y,-x,+z
   +y,+x,+z
loop_
_atom_site_label
_atom_site_type_symbol
_atom_site_fract_x
_atom_site_fract_y
_atom_site_fract_z
_atom_site_U_iso_or_equiv
Sr001   Sr   0.00000000   0.00000000   0.00000000   0.05000000
Sr002   Sr   0.00000000   0.00000000   0.10000000   0.05000000
Sr003   Sr   0.00000000   0.00000000   0.80000002   0.05000000
Ti004   Ti   0.50000000   0.50000000   0.05000000   0.05000000
Ti005   Ti   0.50000000   0.50000000   0.25000001   0.05000000
Ti006   Ti   0.50000000   0.50000000   0.85000005   0.05000000
O0007   O    0.50000000   0.50000000   0.00000000   0.05000000
O0008   O    0.50000000   0.50000000   0.10000000   0.05000000
O0009   O    0.50000000   0.50000000   0.80000002   0.05000000
O0010   O    0.00000000   0.50000000   0.05000000   0.05000000
O0011   O    0.00000000   0.50000000   0.85000005   0.05000000
O0012   O    0.50000000   0.00000000   0.25000001   0.05000000
#End  data_Wien2k_Data
```

Bibliography

(1) Somorjai, G. A., *Principles of Surface Chemistry*; Johnston, H. S., Ed.; Prentice Hall: Englewood Cliffs, NJ, 1972.

(2) Chadi, D. J. *Physical Review Letters* **1979**, *43*, 43–47, DOI: 10.1103/PhysRevLett.43.43.

(3) Palmberg, P. W.; Rhodin, T. N. *Physical Review* **1967**, *161*, 586–588, DOI: 10.1103/PhysRev.161.586.

(4) Marks, L. D.; Smith, D. J. *Nature* **1983**, *303*, 316–317, DOI: 10.1038/303316a0.

(5) Enterkin, J. A.; Becerra-Toledo, A. E.; Poeppelmeier, K. R.; Marks, L. D. *Surface Science* **2012**, *606*, 344–355, DOI: 10.1016/j.susc.2011.10.018.

(6) Satterfield, C. N., *Heterogeneous Catalysis in Industrial Practice*, 2nd ed.; McGraw-Hill: New York, 1996.

(7) Kung, H. H.; Ko, E. I. *Chemical Engineering Journal* **1996**, *64*, 203–214, DOI: 10.1016/S0923-0467(96)03139-9.

(8) Centi, G.; Cavani, F.; Trifiro, F., *Selective Oxidation by Heterogenous Catalysis*, 1st ed.; Centi, G., Cavani, F., Trifiro, F., Eds.; Kluwer Academic: New York, 2001.

(9) Bartholomew, C. H.; Farrauto, R. J., *Fundamentals of Industrial Catalytic Processes*, 2nd ed.; John Wiley & Sons, Inc: Hoboken, NJ, 2006.

(10) Wachs, I. E.; Kim, T. In *Metal Oxide Catalysis*; Wiley-VCH Verlag GmbH & Co. KGaA: 2009, pp 487–498.

(11) Franke, M. E.; Koplin, T. J.; Simon, U. *Small* **2006**, *2*, 36–50, DOI: 10.1002/smll.200500261.

(12) Fernández-García, M.; Rodriguez, J. A. In *Encyclopedia of Inorganic Chemistry*; John Wiley & Sons, Ltd: 2006.

(13) Beek, W. J. E.; Wienk, M. M.; Janssen, R. A. J. *Advanced Materials* **2004**, *16*, 1009–1012, DOI: 10.1002/adma.200306659.

(14) Simon, P.; Gogotsi, Y. *Nature Materials* **2008**, *7*, 845–854, DOI: 10.1038/nmat2297.

(15) Mitchell, E.; De Souza, F.; Gupta, R.; Kahol, P.; Kumar, D.; Dong, L.; Gupta, B. K. *Powder Technology* **2015**, *272*, 295–299, DOI: 10.1016/j.powtec.2014.12.021.

(16) Voorhoeve, R. J.; Remeika, J. P.; Gallagher, P. K.; Johnson, D. W. *Science* **1977**, *195*, 827–833, DOI: 10.1126/science.195.4281.827.

(17) Arlt, G.; Hennings, D.; de With, G. *Journal of Applied Physics* **1985**, *58*, 1619–1625, DOI: 10.1063/1.336051.

(18) Kiss, K.; Magder, J.; Vukasovich, M. S.; Lockhart, R. J. *Journal of the American Ceramic Society* **1966**, *49*, 291–295, DOI: 10.1111/j.1151-2916.1966.tb13265.x.

(19) Gunnarsson, R.; Kalabukhov, A.; Winkler, D. *Surface Science* **2009**, *603*, 151–157, DOI: 10.1016/j.susc.2008.10.045.

(20) Ohnishi, T.; Takahashi, K.; Nakamura, M.; Kawasaki, M.; Yoshimoto, M.; Koinuma, H. *Applied Physics Letters* **1999**, *74*, 2531–2533, DOI: 10.1063/1.123888.

(21) John, A. M.; Jose, R.; Ittyachen, M. A.; Koshy, J. *Superconductor Science and Technology* **2002**, *15*, 907–912, DOI: 10.1088/0953-2048/15/6/312.

(22) Kobayashi, J.; Tazoh, Y.; Miyazawa, S. *Journal of Crystal Growth* **1993**, *131*, 138–144, DOI: 10.1016/0022-0248(93)90406-m.

(23) McColm, T. D.; Irvine, J. T. S. *Ionics* **2001**, *7*, 116–121, DOI: 10.1007/BF02375477.

(24) Biegel, W.; Klarmann, R.; Stritzker, B.; Schey, B.; Kuhn, M. *Applied Surface Science* **2000**, *168*, 227–233, DOI: 10.1016/s0169-4332(00)00604-8.

(25) Klein, A.; Körber, C.; Wachau, A.; Säuberlich, F.; Gassenbauer, Y.; Harvey, S. P.; Proffit, D. E.; Mason, T. O. *Materials* **2010**, *3*, 4892–4914, DOI: 10.3390/ma3114892.

(26) Haller, G. L.; Resasco, D. E. *Advances in Catalysis* **1989**, *36*, 173–235, DOI: 10.1016/S0360-0564(08)60018-8.

(27) Ohtomo, A.; Hwang, H. Y. *Nature* **2004**, *427*, 423–426, DOI: 10.1038/nature04773.

(28) Williams, D. B.; Carter, C. B., *Transmission Electron Microscopy*; Springer Science: New York, NY, 2009.

(29) JEOL JEM 2100F Instruction Manual: Column Interior., JEOL USA, (accessed 11/13/2015).

(30) Hirsch, P.; Howie, A.; Nicholson, R.; Pashley, D.; Whelan, M., *Electron Microscopy of Thin Films*; Butter-worths: 1965.

(31) Cowley, J. M., *Diffraction Physics*, 3rd ed.; Elsebier Science B.V.: Amsterdam, 1995.

(32) Griffiths, P.; de Haseth, J. A., *Fourier Transform Infrared Spectrometry*, 2nd; John Wiley & Sons, Inc.: 2007.

(33) Brunauer, S.; Emmett, P. H.; Teller, E. *Journal of the American Chemical Society* **1938**, *60*, 309–319, DOI: 10.1021/ja01269a023.

(34) Rabenau, A. *Angewandte Chemie International Edition* **1985**, *24*, 1026–1040, DOI: 10.1002/anie.198510261.

(35) Byrappa, K.; Yoshimura, M. In *Handbook of Hydrothermal Technology*; William Andrew Publishing: Norwich, NY, 2001.

(36) Joshi, U. A.; Lee, J. S. *Small* **2005**, *1*, 1172–1176, DOI: 10.1002/smll.200500055.

(37) Urban, J. J.; Yun, W. S.; Gu, Q.; Park, H. *Journal of the American Chemical Society* **2002**, *124*, 1186–1187, DOI: 10.1021/ja017694b.

(38) Modeshia, D. R.; Walton, R. I. *Chemical Society Reviews* **2010**, *39*, 4303–4325, DOI: 10.1039/b904702f.

(39) Callen, H. B., *Thermodynamics and an Introduction to Thermostatistics*; John Wiley & Sons, Inc: New York, NY, 1985.

(40) Cowley, J. M.; Moodie, A. F. *Acta Crystallographica* **1957**, *10*, 609–619, DOI: 10.1107/s0365110x57002194.

(41) Peng, L. M.; Dudarev, S. L.; Whelan, M. J., *High-Energy Electron Diffraction and Microscopy*; Monographs on the physics and chemistry of materials; Oxford University Press: Oxford, UK, 2011.

(42) Kirkland, E., *Advanced Computing in Electron Microscopy*, 2nd ed.; Springer Science: New York, NY, 2010.

(43) Briechle, K.; Hanebeck, U. D. In *Proceedings of SPIE*, Optical Pattern Recognition XII, 2001; Vol. 4387, pp 95–102, DOI: 10.1117/12.421129.

(44) Lewis, J. P. *Vision Interface* **1995**, *10*, 120–123, DOI: 10.1007/s00034-009-9130-7.

(45) Wulff, G. *Zeitschrift fur Krystallographie und Mineralogie* **1901**, *34*, 449–530.

(46) Von Laue, M. *Zeitschrift für Kristallographie - Crystalline Materials* **1943**, *105*, 124–133, DOI: 10.1524/zkri.1943.105.1.124.

(47) Miracle-Sole, S. *arXiv preprint arXiv:1307.5180* **2013**, 1–15.

(48) Taylor, J. E., *Some crystalline variational techniques and results*; Asterisque: 1987; Vol. 154, pp 307–319.

(49) Ringe, E.; Van Duyne, R. P.; Marks, L. D. *Nano Letters* **2011**, *11*, 3399–3403, DOI: 10.1021/nl2018146.

(50) Ringe, E.; Van Duyne, R. P.; Marks, L. D. *Journal of Physical Chemistry C* **2013**, *117*, 15859–15870, DOI: 10.1021/jp401566m.

(51) Lüth, H., *Surfaces and Interfaces of Solids*; Springer Berlin Heidelberg: 1993, DOI: 10.1007/978-3-662-10159-9.

(52) Zucker, R. V.; Chatain, D.; Dahmen, U.; Hagége, S.; Carter, W. C. *Journal of Materials Science* **2012**, *47*, 8290–8302, DOI: 10.1007/s10853-012-6739-x.

(53) Christensen, S. T.; Elam, J. W.; Rabuffetti, F. A.; Ma, Q.; Weigand, S. J.; Lee, B.; Seifert, S.; Stair, P. C.; Poeppelmeier, K. R.; Hersam, M. C.; Bedzyk, M. J. *Small* **2009**, *5*, 750–757, DOI: 10.1002/smll.200801920.

(54) Enterkin, J. A.; Setthapun, W.; Elam, J. W.; Christensen, S. T.; Rabuffetti, F. A.; Marks, L. D.; Stair, P. C.; Poeppelmeier, K. R.; Marshall, C. L. *ACS Catalysis* **2011**, *1*, 629–635, DOI: 10.1021/cs200092c.

(55) Rabuffetti, F. A.; Stair, P. C.; Poeppelmeier, K. R. *Journal of Physical Chemistry C* **2010**, *114*, 11056–11067, DOI: 10.1021/Jp101727c.

(56) Blaha, P.; Schwarz, K.; Madsen, G. K. H.; Kvasnicka, D.; Luitz, J., *WIEN2k, An Augmented Plane Wave Plus Local Orbitals Program for Calculating Crystal Properties*; Technical University of Vienna: Vienna, 2001; Vol. 28.

(57) Marks, L. D. *Journal of Chemical Theory and Computation* **2013**, *9*, 2786–2800, DOI: 10.1021/Ct4001685.

(58) Perdew, J. P.; Ruzsinszky, A.; Csonka, G. I.; Vydrov, O. A.; Scuseria, G. E.; Constantin, L. A.; Zhou, X.; Burke, K. *Physical Review Letters* **2008**, *100*, 136406, DOI: 10.1103/physrevlett.100.136406.

(59) Staroverov, V. N.; Scuseria, G. E.; Tao, J.; Perdew, J. P. *Journal of Chemical Physics* **2003**, *119*, 12129–12137, DOI: 10.1063/1.1626543.

(60) Kienzle, D. M.; Becerra-Toledo, A. E.; Marks, L. D. *Physical Review Letters* **2011**, *106*, 176102, DOI: 10.1103/PhysRevLett.106.176102.

(61) Chen, J.; Huang, K.; Liu, S. *Electrochimica Acta* **2009**, *55*, 1–5, DOI: 10.1016/j.electacta.2009.04.017.

(62) Zhu, Y.; Zhang, L.; Gao, C.; Cao, L. *Journal of Materials Science* **2000**, *35*, 4049–4054, DOI: 10.1023/A:1004882120249.

(63) Smigelskas, A.; Kirkendall, E. O. *AIME Transactions* **1947**, *171*, 130–142.

(64) Enterkin, J. A.; Subramanian, A. K.; Russell, B. C.; Castell, M. R.; Poeppelmeier, K. R.; Marks, L. D. *Nature Materials* **2010**, *9*, 245–248, DOI: 10.1038/nmat2636.

(65) Lin, Y.; Wen, J.; Hu, L.; Kennedy, R. M.; Stair, P. C.; Poeppelmeier, K. R.; Marks, L. D. *Phys Rev Lett* **2013**, *111*, 156101, DOI: 10.1103/PhysRevLett.111.156101.

(66) Li, F. M.; Wang, Z. M.; Meng, S.; Sun, Y. B.; Yang, J. L.; Guo, Q. L.; Guo, J. D. *Physical Review Letters* **2011**, *107*, 36103, DOI: 10.1103/PhysRevLett.107.036103.

(67) Dong, L. Q.; Shi, H.; Cheng, K.; Wang, Q.; Weng, W. J.; Han, W. Q. *Nano Research* **2014**, *7*, 1311–1318, DOI: 10.1007/s12274-014-0495-y.

(68) Vasquez, R. P. *Surface Science Spectra* **1992**, *1*, 129–135, DOI: 10.1116/1.1247683.

(69) Alpay, D.; Peng, L.; Marks, L. D. *Journal of Physical Chemistry C* **2015**, *119*, 21018–21023, DOI: 10.1021/acs.jpcc.5b07021.

(70) Marks, L. D.; Peng, L. *Journal of Physics: Condensed Matter* **2016**, *28*, 53001, DOI: 10.1088/0953-8984/28/5/053001.

(71) Hu, L. H.; Wang, C. D.; Lee, S.; Winans, R. E. R.; Marks, L. D.; Poeppelmeier, K. R. *Chemistry of Materials* **2013**, *25*, 378–384, DOI: 10.1021/cm303303x.

(72) Zhan, H. Q.; Chen, Z.-G. G.; Zhuang, J. L.; Yang, X. F.; Wu, Q. L.; Jiang, X. P.; Liang, C. L.; Wu, M. M.; Zou, J. *Journal of Physical Chemistry C* **2015**, *119*, 3530–3537, DOI: 10.1021/jp512448p.

(73) Landree, E.; Grozea, D.; Collazo-Davila, C.; Marks, L. *Physical Review B* **1997**, *55*, 7910–7916, DOI: 10.1103/PhysRevB.55.7910.

(74) Yeomans, J. M., *Statistical Mechanics of Phase Transitions*; Oxford University Press: Oxford, UK, 1992.

(75) Corkhill, J.; Goodman, J. *Advances in Colloid and Interface Science* **1969**, *2*, 298–330, DOI: 10.1016/0001-8686(69)85003-7.

(76) Kanicky, J. R.; Shah, D. O. *Journal of Colloid and Interface Science* **2002**, *256*, 201–207, DOI: 10.1006/jcis.2001.8009.

(77) Spencer, J. N.; Bodner, G. M.; Rickard, L. H., *Chemistry: Structure and Dynamics*, 5th; John Wiley & Sons: 28, 2010.

(78) Wood, M. H.; Casford, M. T.; Steitz, R.; Zarbakhsh, A.; Welbourn, R. J. L.; Clarke, S. M. *Langmuir* **2016**, *32*, 534–540, DOI: 10.1021/acs.langmuir.5b04435.

(79) Hu, L.; Wang, C.; Kennedy, R. M.; Marks, L. D.; Poeppelmeier, K. R.; Kenneth, R. *Inorganic Chemistry* **2014**, 1–2, DOI: 10.1021/ic5011715.

(80) Rabuffetti, F. A.; Kim, H. S.; Enterkin, J. A.; Wang, Y. M.; Lanier, C. H.; Marks, L. D.; Poeppelmeier, K. R.; Stair, P. C. *Chemistry of Materials* **2008**, *20*, 5628–5635, DOI: 10.1021/Cm801192t.

(81) Ekwall, P. *Advances in Liquid Crystals* **1975**, *1*, 1–142, DOI: 10.1016/B978-0-12-025001-1.50007-X.

(82) Vo, D. Q.; Kim, E.-J.; Kim, S. *Journal of Colloid and Interface Science* **2009**, *337*, 75–80, DOI: 10.1016/j.jcis.2009.04.078.

(83) Fujinami, K.; Katagiri, K.; Kamiya, J.; Hamanaka, T.; Koumoto, K. *Nanoscale* **2010**, *2*, 2080–3, DOI: 10.1039/c0nr00543f.

(84) Friderichs, C.; Zotov, N.; Mader, W. *European Journal of Inorganic Chemistry* **2015**, *2015*, 288–295, DOI: 10.1002/ejic.201402724.

(85) Jing, C.; Hanbing, S. X. *Dyes and Pigments* **2007**, *75*, 766–769, DOI: 10.1016/j.dyepig.2006.08.020.

(86) Shih, W. Y.; Shih, W.-H.; Aksay, I. A. *Physical Review B* **1994**, *50*, 15575–15585, DOI: 10.1103/PhysRevB.50.15575.

(87) Frey, M. H.; Payne, D. A. *Physical Review B* **1996**, *54*, 3158–3168, DOI: 10.1103/PhysRevB.54.3158.

(88) Smith, M. B.; Page, K.; Siegrist, T.; Redmond, P. L.; Walter, E. C.; Seshadri, R.; Brus, L. E.; Steigerwald, M. L. *Journal of the American Chemical Society* **2008**, *130*, 6955–6963, DOI: 10.1021/ja0758436.

(89) Park, Y.; Lee, W.-J.; Kim, H.-G. *Journal of Physics: Condensed Matter* **1997**, *9*, 9445–9456, DOI: 10.1088/0953-8984/9/43/027.

(90) Christensen, A. N.; Rasmussen, S. E. *Acta Chemica Scandinavica* **1963**, *17*, 845–845, DOI: 10.3891/acta.chem.scand.17-0845.

(91) Christensen, A. N. *Acta Chemica Scandinavica* **1970**, *24*, 2447–2452, DOI: 10.3891/acta.chem.scand.24-2447.

(92) Eckert, J. O.; Hung-Houston, C. C.; Gersten, B. L.; Lencka, M. M.; Riman, R. E. *Journal of the American Ceramic Society* **1996**, *79*, 2929–2939, DOI: 10.1111/j.1151-2916.1996.tb08728.x.

(93) MacLaren, I.; Ponton, C. *Journal of the European Ceramic Society* **2000**, *20*, 1267–1275, DOI: 10.1016/S0955-2219(99)00287-3.

(94) Lu, S. W.; Lee, B. I.; Lin Wang, Z.; Samuels, W. D. *Journal of Crystal Growth* **2000**, *219*, 269–276, DOI: 10.1016/S0022-0248(00)00619-9.

(95) Testino, A.; Buscaglia, M. T.; Buscaglia, V.; Viviani, M.; Bottino, C.; Nanni, P. *Chemistry of Materials* **2004**, *16*, 1536–1543, DOI: 10.1021/cm031130k.

(96) Wang, Y.; Xu, H.; Wang, X.; Zhang, X.; Jia, H.; Zhang, L.; Qiu, J. *Journal of Physical Chemistry B* **2006**, *110*, 13835–13840, DOI: 10.1021/jp061597t.

(97) Nomura, T.; Mori, T.; Konishi, Y. *International Journal of Nanoscience* **2007**, *06*, 155–159, DOI: 10.1142/S0219581X07004420.

(98) Adireddy, S.; Lin, C.; Cao, B.; Zhou, W.; Caruntu, G. *Chemistry of Materials* **2010**, *22*, 1946–1948, DOI: 10.1021/cm9038768.

(99) Kimijima, T.; Kanie, K.; Nakaya, M.; Muramatsu, A. *Materials Transactions* **2014**, *55*, 147–153, DOI: 10.2320/matertrans.M2013350.

(100) Costa, G. C. C.; Saradhi, P. M.; Navrotsky, A. *Journal of the American Ceramic Society* **2012**, *95*, 3254–3262, DOI: 10.1111/j.1551-2916.2012.05373.x.

(101) Sahu, S. K.; Maram, P. S.; Navrotsky, A. *Journal of the American Ceramic Society* **2013**, *96*, 3670–3676, DOI: 10.1111/jace.12622.

(102) Lencka, M. M.; Riman, R. E. *Ferroelectrics* **1994**, *151*, 159–164, DOI: 10.1080/00150199408244737.

(103) Moulder, J. F.; Stickle, W. F.; Sobol, P. E.; Bomben, K. D., *Handbook of X-Ray Photoelectron Spectroscopy*; Chastain, J., Ed.; Perkin-Elmer Corporation: Eden Prairie, Minnesota, 1992.

(104) Schmitz, P. J. *Surface Science Spectra* **2001**, *8*, 190–194, DOI: 10.1116/11.20011102.

(105) Lencka, M.; Riman, R. *Chemistry of Materials* **1995**, *7*, 18–25, DOI: 10.1021/cm00049a006.

(106) Jiang, Q. D.; Zegenhagen, J. *Surface Science* **1999**, *425*, 343–354, DOI: 10.1016/S0039-6028(99)00223-X.

(107) Erdman, N.; Poeppelmeier, K. R.; Asta, M.; Warschkow, O.; Ellis, D. E.; Marks, L. D. *Nature* **2002**, *419*, 55–58, DOI: 10.1038/Nature01010.

(108) Erdman, N.; Warschkow, O.; Asta, M.; Poeppelmeier, K. R.; Ellis, D. E.; Marks, L. D. *Journal of the American Chemical Society* **2003**, *125*, 10050–10056, DOI: 10.1021/ja034933h.

(109) Deak, D. S.; Silly, F.; Newell, D. T.; Castell, M. R. *The Journal of Physical Chemistry B* **2006**, *110*, 9246–9251, DOI: 10.1021/jp060954x.

(110) Silly, F.; Newell, D. T.; Castell, M. R. *Surface Science* **2006**, *600*, L219–L223, DOI: 10.1016/j.susc.2006.05.043.

(111) Heifets, E.; Piskunov, S.; Kotomin, E. A.; Zhukovskii, Y. F.; Ellis, D. E. *Physical Review B* **2007**, *75*, 115417, DOI: 10.1103/PhysRevB.75.115417.

(112) Wohlwend, J. L.; Behera, R. K.; Jang, I.; Phillpot, S. R.; Sinnott, S. B. *Surface Science* **2009**, *603*, 873–880, DOI: 10.1016/j.susc.2009.01.035.

(113) Wang, Z.; Loon, A.; Subramanian, A.; Gerhold, S.; McDermott, E.; Enterkin, J. A.; Hieckel, M.; Russell, B. C.; Green, R. J.; Moewes, A.; Guo, J.; Blaha, P.; Castell, M. R.; Diebold, U.; Marks, L. D. *Nano Letters* **2016**, *16*, 2407–2412, DOI: 10.1021/acs.nanolett.5b05211.

(114) Haertling, G. H. *Journal of the American Ceramic Society* **1999**, *82*, 797–818, DOI: 10.1111/j.1151-2916.1999.tb01840.x.

(115) Damjanovic, D. *Reports on Progress in Physics* **1998**, *61*, 1267, DOI: 10.1088/0034-4885/61/9/002.

(116) Tan, C.-S.; Hsu, S.-C.; Ke, W.-H.; Chen, L.-J.; Huang, M. H. *Nano Letters* **2015**, *15*, 2155–2160, DOI: 10.1021/acs.nanolett.5b00150.

(117) Li, J.; Bai, H.; Yi, W.; Liu, J.; Li, Y.; Zhang, Q.; Yang, H.; Xi, G. *Nano Research* **2016**, *9*, 1523–1531, DOI: 10.1007/s12274-016-1048-3.

(118) Kakekhani, A.; Ismail-Beigi, S. *ACS Catalysis* **2015**, *5*, 4537–4545, DOI: 10.1021/acscatal.5b00507.

(119) Castell, M. R. *Surf. Sci.* **2002**, *505*, 1–13, DOI: 10.1016/s0039-6028(02)01393-6.

(120) Zhu, G.-z.; Radtke, G.; Botton, G. A. *Nature* **2012**, *490*, 384–387, DOI: 10.1038/nature11563.

(121) Marshall, M. S. J.; Becerra-Toledo, A. E.; Marks, L. D.; Castell, M. R. In *Defects at Oxide Surfaces*; Springer Series in Surface Sciences; Springer International Publishing: 2015, pp 327–349, DOI: 10.1007/978-3-319-14367-5_11.

(122) Ciston, J.; Brown, H. G.; D'Alfonso, A. J.; Koirala, P.; Ophus, C.; Lin, Y.; Suzuki, Y.; Inada, H.; Zhu, Y.; Allen, L. J.; Marks, L. D. *Nature Communications* **2015**, *6*, 7358, DOI: 10.1038/ncomms8358.

(123) Marks, L. D.; Smith, D. J. *Journal of Microscopy-Oxford* **1983**, *130*, 249–261, DOI: 10.1111/j.1365-2818.1983.tb04222.x.

(124) Saitoh, H.; Sunayama, H.; Tanaka, N.; Ohshio, S. *J. Ceram. Soc. Jpn.* **1998**, *106*, 1051–1055, DOI: 10.2109/jcersj.106.1051.

(125) Shimizu, R.; Ohsawa, T.; Iwaya, K.; Shiraki, S.; Hitosugi, T. *Crystal Growth & Design* **2014**, *14*, 1555–1560, DOI: 10.1021/cg4013119.

(126) Koster, G.; Kropman, B. L.; Rijnders, G. J. H. M.; Blank, D. H. A.; Rogalla, H. *Applied Physics Letters* **1998**, *73*, 2920–2922, DOI: 10.1063/1.122630.

(127) Kawasaki, M.; Takahashi, K.; Maeda, T.; Tsuchiya, R.; Shinohara, M.; Ishiyama, O.; Yonezawa, T.; Yoshimoto, M.; Koinuma, H. *Science* **1994**, *266*, 1540–1542, DOI: 10.2307/2885181.

(128) Biswas, A.; Rossen, P. B.; Yang, C.-H.; Siemons, W.; Jung, M.-H.; Yang, I. K.; Ramesh, R.; Jeong, Y. H. *Appl. Phys. Lett.* **2011**, *98*, 051904, DOI: 10.1063/1.3549860.

(129) Wang, C.; Koirala, P.; Stair, P.; Marks, L. *Applied Surface Science* **2017**, *422*, 661–665, DOI: 10.1016/j.apsusc.2017.05.187.

(130) Hatch, R. C.; Fredrickson, K. D.; Choi, M.; Lin, C.; Seo, H.; Posadas, A. B.; Demkov, A. A. *J. Appl. Phys.* **2013**, *114*, 103710, DOI: 10.1063/1.4821095.

(131) Hatch, R. C.; Choi, M.; Posadas, A. B.; Demkov, A. A. *J. Vac. Sci. Technol., B* **2015**, *33*, 061204, DOI: 10.1116/1.4931616.

(132) Daniele, P. G.; Foti, C.; Gianguzza, A.; Prenesti, E.; Sammartano, S. *Coordination Chemistry Reviews* **2008**, *252*, 1093–1107, DOI: 10.1016/j.ccr.2007.08.005.

(133) Crosby, L. A.; Kennedy, R. M.; Chen, B.-R.; Wen, J.; Poeppelmeier, K. R.; Bedzyk, M. J.; Marks, L. D. *Nanoscale* **2016**, *8*, 16606–16611, DOI: 10.1039/C6NR05516H.

(134) Meyer, R.; Waser, R.; Helmbold, J.; Borchardt, G. *Journal of Electroceramics* **2002**, *9*, 101–110, DOI: 10.1023/A:1022898104375.

(135) Bachelet, R.; Sánchez, F.; Palomares, F. J.; Ocal, C.; Fontcuberta, J. *Applied Physics Letters* **2009**, *95*, 141915, DOI: 10.1063/1.3240869.

(136) Schrott, A. G.; Misewich, J. A.; Copel, M.; Abraham, D. W.; Zhang, Y. *Applied Physics Letters* **2001**, *79*, 1786–1788, DOI: 10.1063/1.1404129.

(137) Nishimura, J.; Ohtomo, A.; Ohkubo, A.; Murakami, Y.; Kawasaki, M. *Japanese Journal of Applied Physics* **2004**, *43*, L1032, DOI: 10.1143/JJAP.43.L1032.

(138) Patnaik, P., *Handbook of Inorganic Chemicals*; McGraw-Hill: 2003.

(139) Habashy, G. M.; Kolta, G. A. *Journal of Inorganic and Nuclear Chemistry* **1972**, *34*, 57–67, DOI: 10.1016/0022-1902(72)80361-0.

(140) Dinescu, R.; Preda, M. *Journal of Thermal Analysis* **1973**, *5*, 465–473, DOI: 10.1007/BF01950236.

(141) Cai, W.; Rao, T.; Wang, A.; Hu, J.; Wang, J.; Zhong, J.; Xiang, W. *Ceramics International* **2015**, *41*, 4514–4522, DOI: 10.1016/j.ceramint.2014.11.146.

(142) Xiaowei, Y.; Yanwei, Z.; Leiqing, M.; Longxiang, H. *Journal of Colloid and Interface Science* **2011**, *357*, 308–316, DOI: 10.1016/j.jcis.2011.02.015.

(143) Morales, E. H.; Bonnell, D. A. *Surf. Sci.* **2013**, *609*, 62–66, DOI: 10.1016/j.susc.2012.11.006.

(144) Ohring, M., *Materials Science of Thin Films: Deposition and Structure*, 2nd ed.; 6; Academic Press: San Diego, CA, 2002; Vol. 40.

(145) Winterbottom, W. L. *Acta Metallurgica* **1967**, *15*, 303–310, DOI: 10.1016/0001-6160(67)90206-4.

(146) Ino, S. *Journal of the Physical Society of Japan* **1969**, *27*, 941–953, DOI: 10.1143/JPSJ.27.941.

(147) Marks, L. D. *Journal of Crystal Growth* **1983**, *61*, 556–566, DOI: 10.1016/0022-0248(83)90184-7.

(148) Howie, A.; Marks, L. D. *Philosophical Magazine A* **1984**, *49*, 95–109, DOI: 10.1080/01418618408233432.

(149) Marks, L. D. *Philosophical Magazine A* **1984**, *49*, 81–93, DOI: 10.1080/01418618408233431.

(150) Marks, L. D. *Reports on Progress in Physics* **1994**, *57*, 603–649, DOI: 10.1088/0034-4885/57/6/002.

(151) Doraiswamy, N.; Marks, L. D. *Philosophical Magazine B* **1995**, *71*, 291–310, DOI: 10.1080/13642819508239035.

(152) Meusel, I.; Hoffmann, J.; Hartmann, J.; Heemeier, M.; Baumer, M.; Libuda, J.; Freund, H. J. *Catalysis Letters* **2001**, *71*, 5–13, DOI: 10.1023/A:1016635804185.

(153) Liu, S.; Tan, J. M.; Gulec, A.; Crosby, L. A.; Drake, T. L.; Schweitzer, N. M.; Delferro, M.; Marks, L. D.; Marks, T. J.; Stair, P. C. *Organometallics* **2017**, *36*, 818–828, DOI: 10.1021/acs.organomet.6b00869.

(154) Enterkin, J. A.; Kennedy, R. M.; Lu, J. L.; Elam, J. W.; Cook, R. E.; Marks, L. D.; Stair, P. C.; Marshall, C. L.; Poeppelmeier, K. R. *Topics in Catalysis* **2013**, *56*, 1829–1834, DOI: 10.1007/s11244-013-0118-y.

(155) Chen, B.-R.; George, C.; Lin, Y.; Hu, L.; Crosby, L.; Hu, X.; Stair, P. C.; Marks, L. D.; Poeppelmeier, K. R.; Van Duyne, R. P.; Bedzyk, M. J. *Surface Science* **2016**, *648*, 291–298, DOI: 10.1016/j.susc.2015.10.057.

(156) Silly, F.; Castell, M. R. *Physical Review Letters* **2005**, *94*, 046103, DOI: 10.1103/PhysRevLett.94.046103.

(157) Silly, F.; Powell, A. C.; Martin, M. G.; Castell, M. R. *Physical Review B* **2005**, *72*, 165403, DOI: 10.1103/PhysRevB.72.165403.

(158) Gontard, L. C.; Dunin-Borkowski, R. E.; Gass, M. H.; Bleloch, A. L.; Ozkaya, D. *Journal of Electron Microscopy* **2009**, *58*, 167–174, DOI: 10.1093/jmicro/dfp003.

(159) García, M. A.; Ruiz-González, M. L.; de la Fuente, G. F.; Crespo, P.; González, J. M.; Llopis, J.; González-Calbet, J. M.; Vallet-Regí, M.; Hernando, A. *Chemistry of Materials* **2007**, *19*, 889–893, DOI: 10.1021/cm061740v.

(160) Gao, W.; Wu, J.; Yoon, A.; Lu, P.; Qi, L.; Wen, J.; Miller, D. J.; Mabon, J. C.; Wilson, W. L.; Yang, H.; Zuo, J.-M. *Scientific Reports* **2017**, *7*, 17243, DOI: 10.1038/s41598-017-16900-6.

(161) Kang, Y.; Li, M.; Cai, Y.; Cargnello, M.; Diaz, R. E.; Gordon, T. R.; Wieder, N. L.; Adzic, R. R.; Gorte, R. J.; Stach, E. A.; Murray, C. B. *Journal of the American Chemical Society* **2013**, *135*, 2741–2747, DOI: 10.1021/ja3116839.

(162) Fu, Q.; Wagner, T. *Surface Science Reports* **2007**, *62*, 431–498, DOI: 10.1016/j.surfrep.2007.07.001.

(163) Freund, H. J.; Nilius, N.; Risse, T.; Schauermann, S. *Physical Chemistry Chemical Physics* **2014**, *16*, 8148–8167, DOI: 10.1039/c3cp55231d.

(164) Schubert, M. M.; Hackenberg, S.; van Veen, A. C.; Muhler, M.; Plzak, V.; Behm, R. J. *Journal of Catalysis* **2001**, *197*, 113–122, DOI: 10.1006/jcat.2000.3069.

(165) Widmann, D.; Behm, R. J. *Accounts of Chemical Research* **2014**, *47*, 740–749, DOI: 10.1021/ar400203e.

(166) An, K.; Alayoglu, S.; Musselwhite, N.; Plamthottam, S.; Melaet, G.; Lindeman, A. E.; Somorjai, G. A. *Journal of the American Chemical Society* **2013**, *135*, 16689–16696, DOI: 10.1021/ja4088743.

(167) Tauster, S. J. *Accounts of Chemical Research* **1987**, *20*, 389–394, DOI: 10.1021/Ar00143a001.

(168) Willinger, M. G.; Zhang, W.; Bondarchuk, O.; Shaikhutdinov, S.; Freund, H. J.; Schlogl, R. *Angewandte Chemie-International Edition* **2014**, *53*, 5998–6001, DOI: 10.1002/anie.201400290.

(169) Ertl, G. *Angew. Chemie Int. Ed* **1990**, *29*, 1219–1227, DOI: 10.1002/anie.199012191.

(170) Campbell, C. T. *Surface Science Reports* **1997**, *27*, 1–111, DOI: 10.1016/S0167-5729(96)00011-8.

(171) Henry, C. R. *Surface Science Reports* **1998**, *31*, 231–325, DOI: 10.1016/s0167-5729(98)00002-8.

(172) Baumer, M.; Freund, H. J. *Progress in Surface Science* **1999**, *61*, 127–198, DOI: 10.1016/S0079-6816(99)00012-X.

(173) Somorjai, G. A.; McCrea, K. R.; Zhu, J. *Topics in Catalysis* **2002**, *18*, 157–166, DOI: 10.1023/A:1013874202404.

(174) Gao, F.; Goodman, D. W. *Annual Review of Physical Chemistry* **2012**, *63*, 265–286, DOI: 10.1146/annurev-physchem-032511-143722.

(175) Freund, H. J. *Rendiconti Lincei* **2016**, *28*, 5–18, DOI: 10.1007/s12210-016-0560-4.

(176) Goodman, D. W. *Surface Science* **1994**, *299*, 837–848, DOI: 10.1016/0039-6028(94)90701-3.

(177) Goodman, D. W. *The Journal of Physical Chemistry* **1996**, *100*, 13090–13102, DOI: 10.1021/jp953755e.

(178) St Clair, T. P.; Goodman, D. W. *Topics in Catalysis* **2000**, *13*, 5–19, DOI: 10.1023/A:1009020502894.

(179) Freund, H. J.; Kuhlenbeck, H.; Libuda, J.; Rupprechter, G.; Baumer, M.; Hamann, H. *Topics in Catalysis* **2001**, *15*, 201–209, DOI: 10.1023/A:1016686322301.

(180) Somorjai, G. A.; York, R. L.; Butcher, D.; Park, J. Y. *Physical Chemistry Chemical Physics* **2007**, *9*, 3500–3513, DOI: 10.1039/b618805b.

(181) Carr, R. G.; Somorjai, G. A. *Nature* **1981**, *290*, 576–577, DOI: 10.1038/290576a0.

(182) Polli, A. D.; Wagner, T.; Gemming, T.; Ruhle, M. *Surface Science* **2000**, *448*, 279–289, DOI: 10.1016/S0039-6028(99)01233-9.

(183) Iddir, H.; Komanicky, V.; Ogut, S.; You, H.; Zapol, P. *Journal of Physical Chemistry C* **2007**, *111*, 14782–14789, DOI: 10.1021/Jp073041r.

(184) Komanicky, V.; Iddir, H.; Chang, K.-C.; Menzel, A.; Karapetrov, G.; Hennessy, D.; Zapol, P.; You, H. *Journal of the American Chemical Society* **2009**, *131*, 5732–5733, DOI: 10.1021/ja900459w.

(185) Stoltz, S. E.; Ellis, D. E.; Bedzyk, M. J. *Surface Science* **2015**, *633*, 8–16, DOI: 10.1016/j.susc.2014.11.011.

(186) Wagner, T.; Richter, G.; Ruhle, M. *Journal of Applied Physics* **2001**, *89*, 2606–2612, DOI: 10.1063/1.1338987.

(187) Stoltz, S. E.; Ellis, D. E.; Bedzyk, M. J. *Surface Science* **2014**, *630*, 46–63, DOI: 10.1016/j.susc.2014.06.018.

(188) Setthapun, W.; Williams, W. D.; Kim, S. M.; Feng, H.; Elam, J. W.; Rabuffetti, F. A.; Poeppelmeier, K. R.; Stair, P. C.; Stach, E. A.; Ribeiro, F. H.; Miller, J. T.; Marshall, C. L. *Journal of Physical Chemistry C* **2010**, *114*, 9758–9771, DOI: 10.1021/jp911178m.

(189) Haruta, M.; Yamada, N.; Kobayashi, T.; Iijima, S. *Journal of Catalysis* **1989**, *115*, 301–309, DOI: 10.1016/0021-9517(89)90034-1.

(190) Bond, G. C. *Chemical Society Reviews* **1991**, *20*, 441–475, DOI: 10.1039/cs9912000441.

(191) Valden, M.; Lai, X.; Goodman, D. W. *Science* **1998**, *281*, 1647–1650, DOI: 10.1126/science.281.5383.1647.

(192) Bond, G. C.; Thompson, D. T. *Catalysis Reviews* **1999**, *41*, 319–388, DOI: 10.1081/CR-100101171.

(193) Trimm, D. L.; Önsan, Z. I. *Catalysis Reviews* **2001**, *43*, 31–84, DOI: 10.1081/CR-100104386.

(194) Grillo, F.; Natile, M. M.; Glisenti, A. *Applied Catalysis B: Environmental* **2004**, *48*, 267–274, DOI: 10.1016/j.apcatb.2003.11.003.

(195) Oh, S.-H.; Hoflund, G. B. *Journal of Catalysis* **2007**, *245*, 35–44, DOI: 10.1016/j.jcat.2006.09.016.

(196) Isaifan, R. J.; Couillard, M.; Baranova, E. A. *International Journal of Hydrogen Energy* **2017**, *42*, 13754–13762, DOI: 10.1016/j.ijhydene.2017.01.049.

(197) Kennedy, R. Support and Overcoating Effects on Selective Catalysis of Platinum Nanoparticle Model Catalysts., Ph.D. Thesis, Northwestern University, 2017.

(198) Zeigarnik, A. V.; Callaghan, C.; Datta, R.; Fishtik, I.; Shustorovich, E. *Kinetics and Catalysis* **2005**, *46*, 509–515, DOI: 10.1007/s10975-005-0103-y.

(199) King, A. D.; King, R. B.; Yang, D. B. *Journal of the American Chemical Society* **1980**, *102*, 1028–1032, DOI: 10.1021/ja00523a020.